Soft X-ray High-Temperature Regions above Solar Flare Loops

Sachiko Akiyama

Doctor of Philosophy

Department of Astronomical Science,
School of Mathematical and Physical Science,
The Graduate University for Advanced Studies, Japan

January, 2001

Contents

Acknowledgements

I would like to thank my supervisors, Dr. H. Hara and Profs. Te. Watanabe and T. Sakurai for their continuous guidance during this thesis work. In particular, I express special thanks to Dr. H. Hara. During these five years, I have learned solar physics, magnetohydrodynamics, the way of investigation, and many things from him.

I acknowledge Profs. To. Sakurai, M. Hidai and T. Hirayama for introducing me to solar physics. I greatly thank Profs. T. Kosugi, K, Shibata, S. Tsuneta, K. Shibasaki, H. Kurokawa, N. Saito, Ta. Watanabe, and E. Hiei, Drs. N. V. Nitta, Y. Hanaoka, Y. Suematsu, M. Akioka, K. Akita, and S. Watari for many fruitful discussions of solar physics. I also acknowledge Drs. H. S. Hudson and G. A. Doschek for many discussions about solar physics and the calibration of the SXT.

I would like to express my thanks to Drs. T. Sakao, M. Masuda, and T. Yokoyama, for many useful discussion about magnetic reconnection and to Dr. T. Shimizu for discussions how to use the *Yohkoh* data. I am grateful to Drs. J. I. Khan, A. C. Sterling, M. R. Kundu, N. Gopalswamy and G. Slater for many discussions not only in solar physics, but in other topics like English as a language. I thank Drs. M Ohyama, K. Hori, J. Sato, T. Magara, M. Takahashi, M. Shimojo, T. Yoshida, S, Yashiro, A. Takeda, S. Nagata, and Mr. K. Yaji for useful discussions about flares and plasma ejections observed with *Yohkoh*. I thank Messrs. S. Kubo, H. Tonooka, and M. Hata, and Ms. K. Nakakubo for many discussions.

Prof. Y. Ogawara, the project manager of *Yohkoh*, is sincerely acknowledged. He has made a great effort to achieve the project. I express my hearty gratitude to all members of the *Yohkoh* team for their dedicated efforts to the operation. Also the staffs of NASA's Deep Space Network stations are acknowledged for their support to *Yohkoh*.

Finally, I would like to express my largest thanks to my father, mother, sister, and brother.

Abstract

We analyze data of 141 solar flares that were observed with the *Yohkoh* soft and hard X-ray telescopes to investigate general characteristics of a soft X-ray high-temperature region above soft X-ray flare loops. Careful analyses are performed in order to obtain the accurate temperature maps of the high-temperature regions, as these high-temperature regions are the fainter structures located close to the brighter flare loops. Statistical approach is also taken to understand general characteristics of the regions and their roles in the flare energy release mechanism. We carefully estimate the electron temperatures at the flare sites with the filter ratio technique for the *Yohkoh* soft X-ray data, after correcting the spacecraft pointing jitter and scattered X-rays due to the mirror micro-roughness, both of which introduce the errors in temperature estimate. We have found the high-temperature regions of 15–35 million degrees above soft X-ray flare loops for 64 flares in 141 events. The average event has single/multiple high-temperature region(s) of $1\text{–}3\times10^4$ km in size. The region appears at the hard X-ray impulsive phase and its temperature reaches the maximum before the soft X-ray peak time. The volume emission measure of the region is 10^{47-48} cm^3, as the average, which is about ten times smaller than that of 10 million degree flare loop beneath. The high-temperature regions tend to move outwords at a speed of 10–20 km s^{-1}, which is systematically faster than the rising speed of flare loops of 4–6 km s^{-1}. The region tends to be located at the side of the stronger hard X-ray footpoint source measured in the M1 channel (23–33 keV) of the *Yohkoh* hard X-ray telescope, namely showing that the high-temperature region appears at the side of the weaker magnetic fields at the footpoint.

Chapter 1

Introduction

1.1 Solar Flares

Solar flares are explosive phenomena in the solar corona. Energy stored in the coronal magnetic fields is violently released, and as a result coronal plasmas are heated up to more than 10^7 K. In big flares, the total amount of energy reaches more than 10^{32} ergs. A substantial fraction of flare energy goes into accelerating electrons and ions, so these high-energy particles stream down toward the solar surface or out into space. They result in the enhancement of radiations in the wide wavelength ranges (see Fig.1.1).

Before the occurrence of a flare, certain areas in an active region may gradually brighten in several wavelengths. This is called the preflare or precursor phase. According to the categorization of preflares by Gaizauskas (1989), it is a transient phase preceding the impulsive phase, possibly even before the flare onset. It does not necessarily happen at the site of the flare itself. After the preflare phase, violent change takes place. Electromagnetic waves in all wavelengths are strongly emitted, plasma blobs are ejected, and high energy particles are generated. This violent phase is called the impulsive phase. In the subsequent phases, these radiations gradually decrease to their normal levels. This phase is called the gradual or the main phase. Fig.1.1 also shows the temporal intensity changes in various wavelengths. For example, hard X-rays and microwaves are seen for short periods of time and have spiky appearances, whereas soft X-rays and Hα show long periods of durations and have smoother variations of intensity.

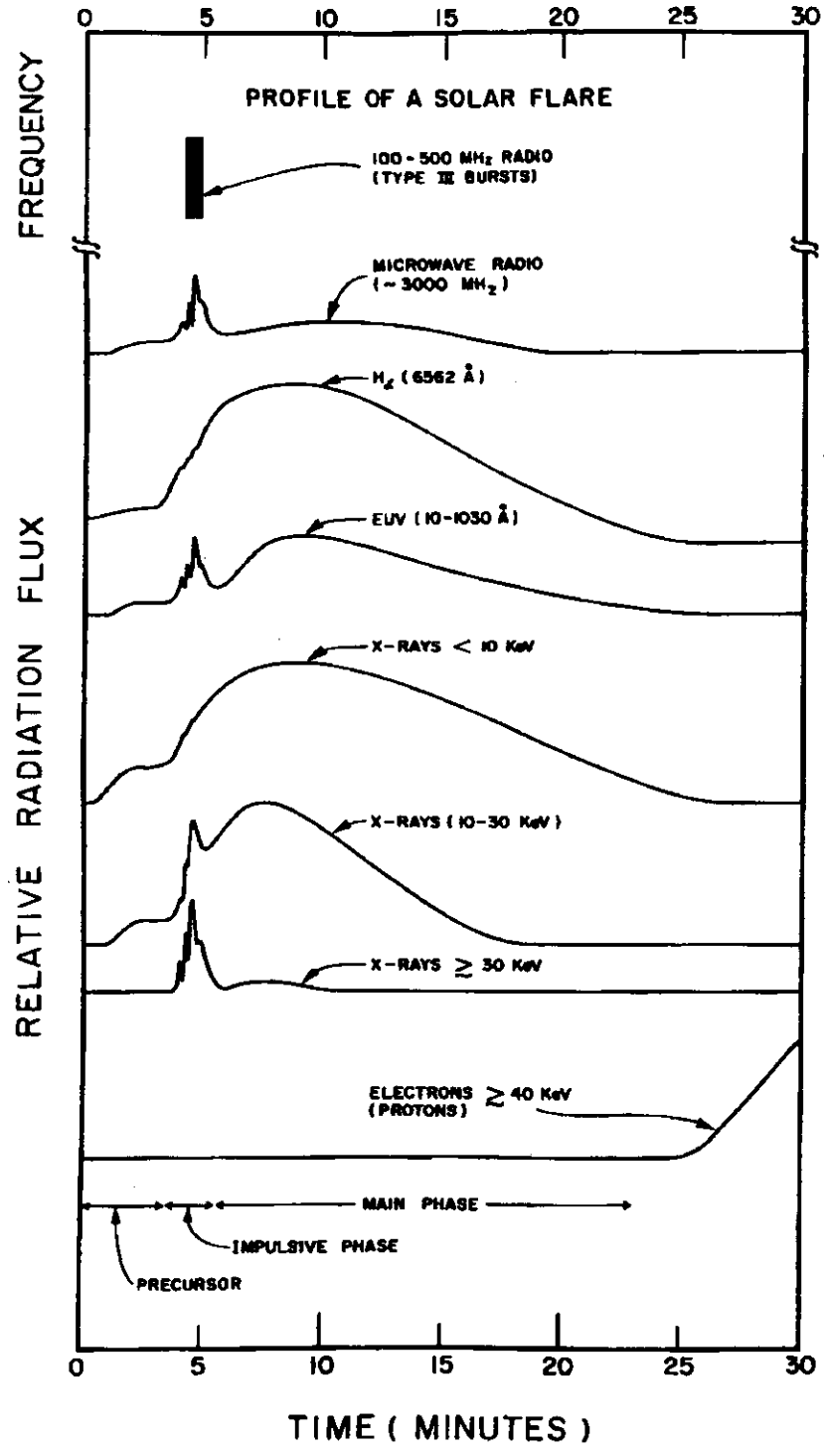

Figure 1.1: A schematic representation of time profiles of a typical solar flare in various wavelengths (reference Svestka monograph).

1.2 Flare Observations: Historical Overview

1.2.1 Hα Observations

A solar flare was first observed in the visible ("white") light by Carrington (1859) and Hodgson, independently in 1859. However, it was very difficult to understand the whole structure of the flares. First only a few white-light flares occur which are able to be observed in the bright photosphere. Second, main parts of flare radiations are emitted in the upper atmosphere of the sun, such as the chromosphere and the corona, which can not be observed in the visible light.

Research on solar flares rapidly progressed after George Ellery Hale developed the spectrohelioscope in the late 1920s. This spectrohelioscope was able to take solar monochromatic images in any wavelength. Especially, the hydrogen alpha (Hα) emission or absorption were the most suitable for the observation of chromospheric structures. The flares were observed as rapid enhancements of Hα emission and called chromospheric eruptions. Flares occurred most frequently in the magnetic configuration having opposite polarities near the sunspots. Since filaments or prominences supported by horizontal and sheared field lines are sometimes seen above the magnetic neutral lines (Severny, 1958), structural changes of the filaments were observed to be associated with flares. Both filaments and prominences are high-density (10^{11} cm^{-3}) but low-temperature (10^4 K) structures in the solar corona, which has lower densities (10^9 cm^{-3}) and higher temperatures (10^6 K). When a prominence is located on the solar disk, it is called a filament. Flare-associated phenomena seen in Hα observations are enumerated as follows.

Smith & Ramsey (1964) and then Martin & Ramsey (1972) reported that filaments were observed to rise about minutes before the flare onsets. The phenomena associated with flares in the preflare phase are generally faint and vague, so it is difficult to clarify the relationship between the preceding phenomena and the flare itself. Besides, some explosive phenomena are observed in the Hα line during the impulsive phase. When big flares occur, structures often appear on either side of the magnetic neutral line as two extended parallel ribbons. This type of flare is called a two-ribbon flare (Zirin & Tanaka, 1973) (Fig.1.2). In addition, filament eruption is one of the most conspicuous and violent Hα phenomenon during the impulsive phase. Filaments start to erupt with a slow speed of a few km s^{-1}, are gradually accelerated, and reach finally a speed of the order of several hundred km s^{-1} (Rompolt, 1990) (Fig.1.3). Flares associated with filament eruptions are mostly the type of two ribbon flares (Hirayama, 1974). The Hα ejecta observed during the impulsive phase include sprays. Warwick (1957) studied Hα sprays which had extraordinarily high speed

outward motions along the apparent straight trajectory. He found that Hα sprays started near the onset of the solar flare. Finally during gradual phase, post-flare loop prominence systems (LPS) are observed to overlie the neutral line for several hours following a major flare (Bruzek, 1964). LPS is considered as excess hot material brought into the corona and seen in chromospheric temperature, as the flare cools down.

1.2.2 Soft X-ray & Hard X-ray Observations: Space Observations

The study of solar flares has changed a lot since the launch of satellites. As we began to observe the sun with X-rays, which are absorbed by the Earth atmosphere, we could immediately guess magnetic structures of the solar corona from those X-ray observations. Solar flare X-rays are classified into two groups according to their energy. One is soft X-ray with relatively low energy between 1 and 10 keV. Soft X-rays originate from thermal radiations of hot plasmas. The other is hard X-rays which have greater penetrating power and higher energy between 10 keV and 100 keV. Hard X-rays are produced by non-thermal electrons accelerated to a fraction of the light velocity and by thermal electrons with higher temperature.

X-ray Radiative Mechanism

Bremsstrahlung is a radiative mechanism of highly accelerated electrons in solar flares. They are observed as both *non-thermal* and *thermal* Bremsstrahlung emissions (Acton, 1968; Kane, 1969; Takakura, 1969) in solar flares.

Energy spectra of non-thermal electrons observed in the impulsive phase show generally a single power-law distribution (Kane, 1969; Frost, 1969) :

$$I(\epsilon) = A\epsilon^{-\gamma}(\text{photons/cm}^2\text{/s/keV}) \tag{1.1}$$

where $I(\epsilon)$ denotes a photon-number distribution as a function of photon energy ϵ (keV). The power index γ typically ranges $3 \leq \gamma \leq 8$ (Dennis, 1985). On the other hand, the thermal Bremsstrahlung spectrum can be described

$$I(\epsilon) = 1.3 \times 10^{-42}(n^2V)\epsilon^{-1.4}(k_BT)^{-0.1}e^{-\epsilon/k_BT}(\text{photons/cm}^2\text{/s/keV}), \tag{1.2}$$

where n (cm^{-3}), V (cm^3), and T (K) are the density, volume, and temperature of plasma, respectively, and k_B (keV/K) is the Boltzman constant (Crannell et al., 1978). These flare emissions in X-rays are optically thin, so the total intensity is proportional to the emission measure (EM), where EM is defined as $EM \equiv n^2V$.

Figure 1.2: Chromospheric brightenings in a two-ribbon pattern on 7 August 1973. When this big flare started in the complex magnetic fields, numerous bright patches were observed in Hα images of the flare region. Connected bright patches became two elongated regions along the neutral line, and these double ribbons gradually separated with time (Zirin & Tanaka 1973).

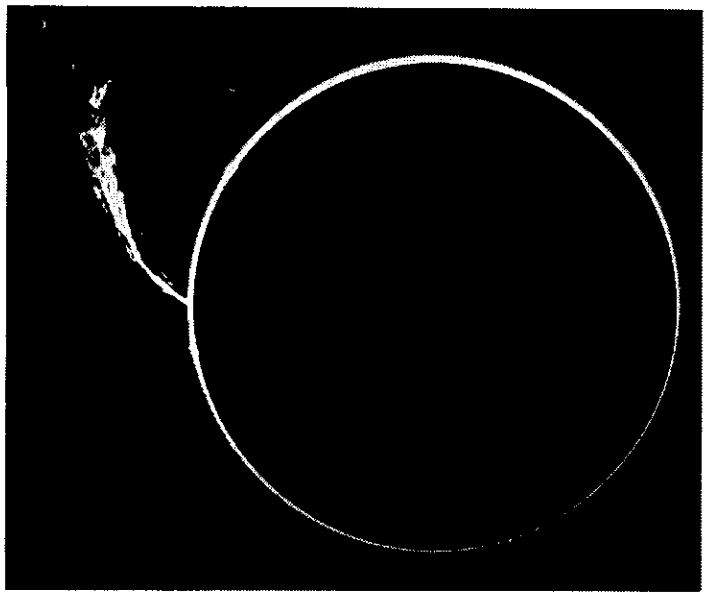

Figure 1.3: Big filament eruption observed in Hα line on 31 July 1992. This photograph was taken by the solar coronagraph at the Norikura Solar Observatory.

The *Skylab* Mission (1970's)

The *Skylab* space station (MacQueen et al., 1974) had two X-ray telescopes, and these telescopes took many X-ray pictures of the corona through 1973 to 1974. Pallavicini et al. (1977) and Pallavicini & Vaiana (1980) reported on flares which emitted X-rays for several hours. This type of flares were called long duration event (LDE) flares. Since many of LDE flares were associated with two-ribbon flares, Hα ejections and LPSs, scientists proposed that energy release of LDE flares took place above the soft X-ray loop. In addition, the *Skylab* mission observed coronal mass ejections (CMEs), which erupted in the corona and were associated with the LDE type of flares (Sheeley et al., 1975; Webb et al., 1976; Kahler, 1977). The speed and the mass of CMEs are about 50 - 2000 km s^{-1} (Gosling et al., 1976; Howard et al., 1985; Harrison et al., 1990; Hundhausen et al., 1994) and 10^{15} - 10^{16} g (Gosling et al., 1974; Hundhausen, 1988), respectively. Pallavicini et al. (1977) and Moore et al. (1980) proposed that solar flares could be classified into two groups: (1) short-duration flares, called compact or impulsive flares, without CMEs, and (2) LDE flares with CME and/or eruptive filaments.

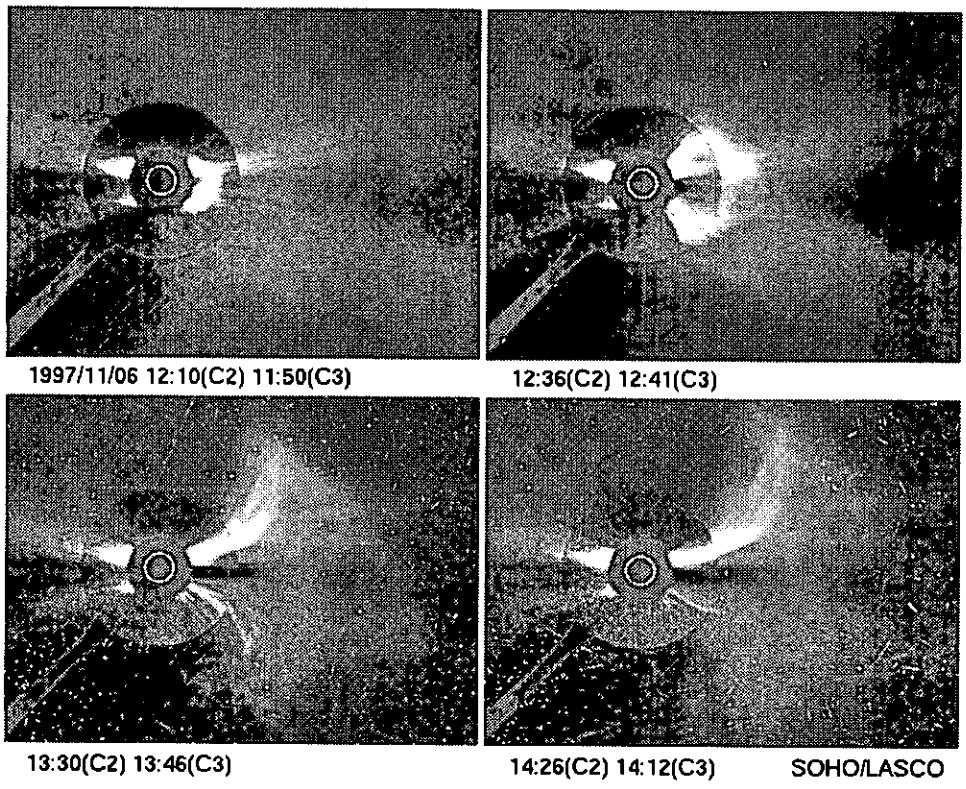

Figure 1.4: Development of a large coronal mass ejection (CME) on 6 November 1997. The four photographs are composite images from the C2 and C3 coronagraphs of the LASCO experiment onboard SOHO. (Field of view C2: 6 solar radii; C3: 32 solar radii.) Courtesy of SOHO/LASCO consortium.

The *SMM* & The *Hinotori* Mission (1980's)

Although Peterson & Winckler (1959) first detected hard X-rays from a flare in the energy range of 200-500 keV using a balloon-borne experiment, images in hard X-rays were observed with the *Solar Maximum Mission* (*SMM*) (Chipman, 1981) and the *Hinotori* mission (Tanaka, Y., 1983) permitting the first detailed study of flaring hard X-ray sources. The Hard X-ray Imaging Spectrometer (HXIS) (Van Beek et al., 1980) aboard the *SMM* satellite and the Solar X-ray Telescope (SXT) (Makishima, 1982; Oda, 1983; Takakura, 1983) aboard the *Hinotori* synthesized two dimensional images of solar flares in hard X-rays. Hoyng et al. (1981) reported that double hard X-ray sources during the impulsive phase of solar flares were concentrated at the footpoints of coronal loops. The *SMM* and *Hinotori* showed that the hard X-ray double sources were observed in many flares and were nearly co-spatial with Hα flare-kernel emissions in the chromosphere (Duijveman et al., 1982). These observations show that hard X-rays are produced by Bremsstrahlung of non-thermal electrons spinning down the two legs of the coronal loop into the low corona and chromosphere.

The *Yohkoh* Mission (1990's)

After the launch of the Solar-A satellite (later called *Yohkoh*), in 1991, researches on solar flares entered a new era (Ogawara et al., 1991). Aiming for the elucidation of the flare physics, *Yohkoh* is capable of high spatial and time resolution observations both in hard and soft X-rays. Especially, detailed comparison between the Hard X-ray Telescope (HXT) (Kosugi et al., 1991) and Soft X-ray Telescope (SXT) (Tsuneta et al., 1991) images led to important discoveries. Masuda et al. (1994) discovered a hard X-ray source above the soft X-ray loop, which suggested that energy of impulsive flares might be released above the soft X-ray loop top (Fig.1.5). In addition, X-ray plasma ejections were observed not only in LDE flares but also in impulsive flares, which had not been thought associated with plasma ejections before (Shibata et al., 1995; Tsuneta, 1997b; Ohyama & Shibata, 1997, 1998) (Fig.1.6). From the above-mentioned observations, Shibata et al. (1995) suggested that impulsive flares, as well, occur as a result of magnetic reconnection process similar to that of LDE flares (see Fig.1.9). *Yohkoh* observations also show other phenomena supportive of the magnetic reconnection model. Cusp-shaped structures are considered as cross-sections of magnetic field lines seen in LDE flares (Tsuneta et al., 1992; Hudson, 1994; Svestka et al., 1995). Tsuneta et al. (1992) reported that temperature map of a cusp flare studied in SXT images showed the tendency that the highest temperature regions occurred in the periphery of the X-ray cusp structures. The distribution of temperature

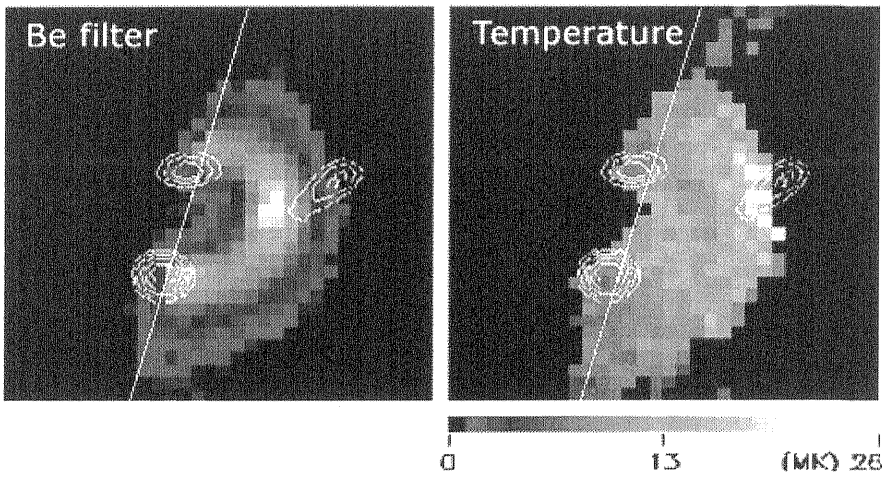

Figure 1.5: Hard X-ray loop top source associated with an impulsive flare on 13 January 1992. Left and right panels show the soft X-ray intensity observed by Be119 filter and the temperature, respectively. Contour lines represent the hard X-ray intensity (M2-bands). Two foot-point sources and a loop top source can be clearly seen. Courtesy of S. Masuda.

in this LDE flare suggested the heating took place by magnetic reconnection.

Sakao (1998) studied the separating motions of hard X-ray double footpoint sources and reported that two kinds of magnetic field configurations were responsible for the solar flare energy release (see Fig.1.7): One is a "loop-with-a-cusp" type, where magnetic reconnection takes place above one closed loop. The other type is an "emerging-flux-type", in which magnetic reconnnection occurs with emerging loops by magnetic buoyancy from the photosphere. In addition, Nishio et al. (1997) reported the characteristics of this "emerging-flux-type" impulsive flares using the Nobeyama Radioheliograph (NoRH), the *Yohkoh*/SXT and HXT, and magnetograms. From the relative locations of microwave, hard X-ray, and soft X-ray sources, at least two loops, the big and the small, seem to be involved in the majority of impulsive flare events.

1.3 Theoretical Models of Solar Flares

Since flares need an explosive release of enormous energy, to accelerate electrons and ions to high speed, and to eject prominences and coronal plasmas, it has been proposed for a long time that the solar magnetic fields provide a plausible source of this energy (Sweet, 1958; Gold & Hoyle, 1960; Petschek, 1964).

During 1940 – 1960, some scenarios appeared using magnetic geometry for the origin of solar flares. Giovanelli (1946) proposed that at the neutral point generated in coronal

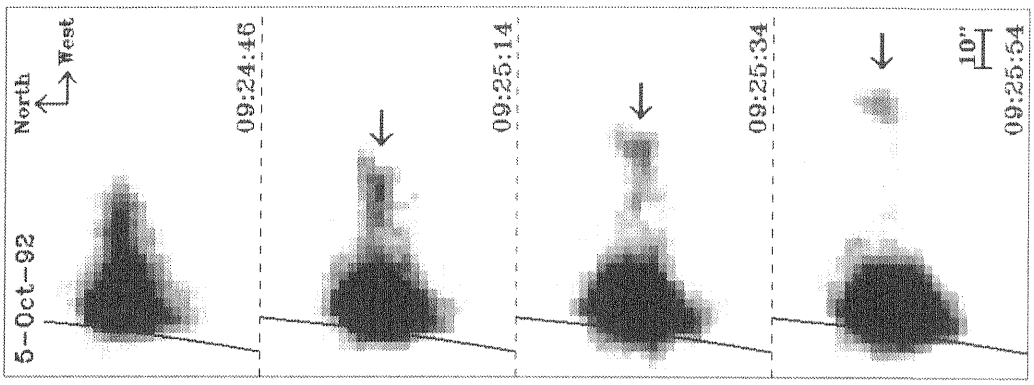

Figure 1.6: Temporal evolution of X-ray plasma ejection associated with the impulsive flare on 5 October 1992. The X-ray plasma ejection is indicated by arrows (Ohyama & Shibata 1998).

magnetic field, electric currents develop excess energy until electrical discharge could release it as a solar flare. Dungey (1958) noticed that the effect of discharge would result in reconnecting the oppositely-directed magnetic lines of force at the neutral point. According to his model, accelerated particles were shot out of the neutral point in two directions, one up into space and the other down toward the Sun. Subsequently the importance of current sheets was pointed out and magnetic reconnnection was considered in the case where oppositely-directed magnetic field are pressed together (Sweet, 1958). Quick dissipation of magnetic energy around the neutral point was shown (Petschek, 1964), as he introduced shock regions near the site of reconnection. These theories of magnetic annihilation contributed greatly to a clear understanding of solar flare physics. In addition, Carmichael (1964) discussed the relation of magnetic fields and accelerated high-energy particles. Sturrock (1966) noticed that when open magnetic fields would become unstable against tearing instability, stored magnetic energy would lead to accelerating particles, plasma ejections, and the formation of two ribbons. Magnetic loop interactions were also discussed: For example Gold & Hoyle (1960) proposed a pair of oppositely-directed and twisted coronal loop configurations, and Heyvaerts (1977) pointed out the important role of emerging flux.

Thanks to Hα observations and X-ray images from the *Skylab* mission, many scientists recognized the important role that the magnetic fields played in various coronal activity including solar flares. Hirayama (1974) and Kopp & Pneuman (1976) proposed a flare model based on the idea that the solar flares have close connections with other energetic phenomena in the solar atmosphere. These models are combined and called the CSHKP model, including results of Carmichael (1964) and Sturrock (1966) (see Fig.1.8). This

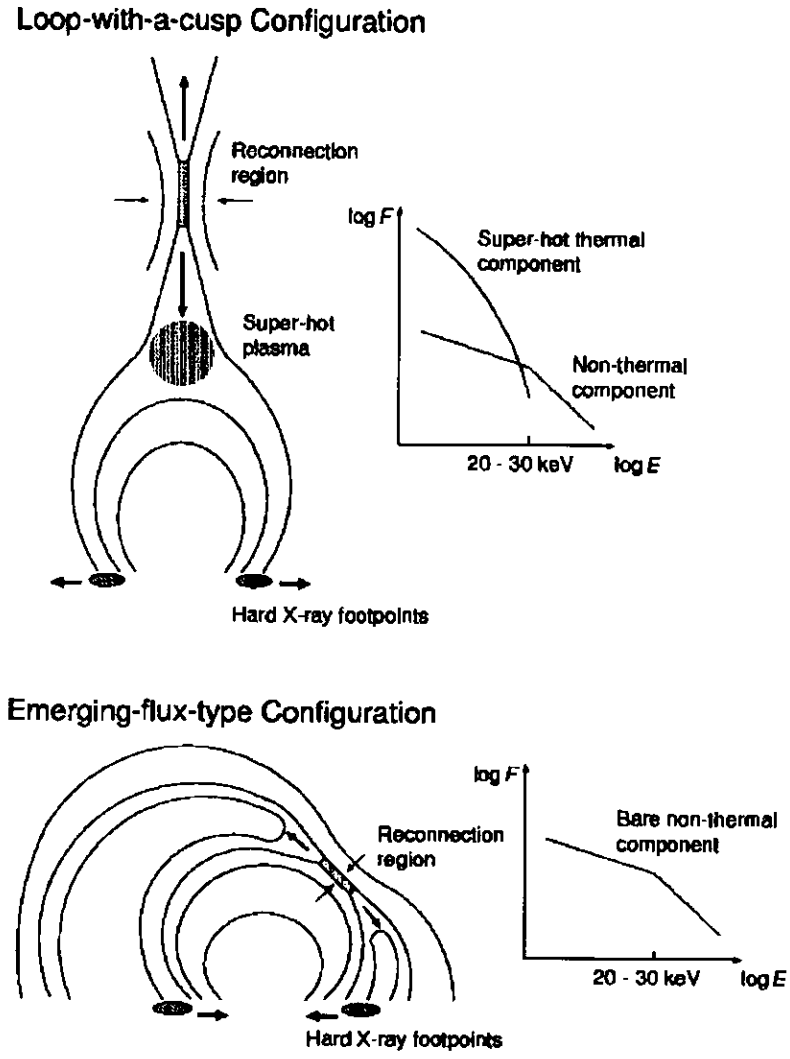

Figure 1.7: Two types of magnetic configuration in solar flares. Flares of the "loop-with-a-cusp" configuration produce super-hot plasma at the loop top, while such plasma is hardly produced in flares of the "emerging-flux-type" configuration. (Sakao et al. 1998).

model suggests that the magnetic reconnnection occurs in a current sheet formed in the corona, and that the magnetic energy is converted into thermal and kinetic energies. Since all phenomena like filament eruption, CMEs, two-ribbon structures, and LPSs, show the effects of magnetic reconnnection, the CSHKP model was considered to be the model for the LDE events associated with variety of erupting phenomena and LPSs.

Since the *Yohkoh* satellite was launched, many phenomena suggestive of magnetic reconnection in solar flares were clearly observed thanks to its high cadence capability. Combining impulsive flare findings by *Yohkoh*, like hard X-ray source above the loop top (Masuda et al., 1994) and of soft X-ray ejections (Shibata et al., 1995), Shibata et al. (1995) suggested to unify the models for the impulsive and LDE flares. According to his unified model, all flare-like phenomena take place by magnetic reconnection, and the differences are only in size and life time, which modify the apparent characteristics of flares.

1.4 High Temperature Plasmas in Solar Flares

Solar flares generate a wide range of high energy particles and plasmas, with thermal sources of temperatures of ($0.5 \leq$ kT ≤ 4 keV) and non-thermal energies ranging above 1 keV.

1.4.1 Classification of Flare Plasmas

Non-Thermal Electrons with Power-Law Distribution

Non-thermal spectra observed as hard X-ray emissions are produced by Bremsstrahlung of high energy electrons in 0.5–1.0 MeV energy range, and stopped in the solar chromosphere. Brown (1971) proposed two processes to produce non-thermal hard X-ray Bremsstrahlung, *thick target* and *thin target* emissions. The difference is the energy loss process of electrons. Both describe an energy loss mainly due to Coulomb collisions with dense plasma. Hard X-ray double-sources located at loop foot-points are thought to result from thick-target of emission. Thin-target Bremsstrahlung results in low-density plasma, where high energy electrons are trapped in the magnetic bottle of a coronal loop, for example, by the magnetic mirror effect.

Thermal Plasmas Produced by Chromospheric Evaporation

Neupert (1968) reported that the peak of the gradual phase in flares was generally later than the peak of the impulsive phase observed by microwave radio emission. Recently this

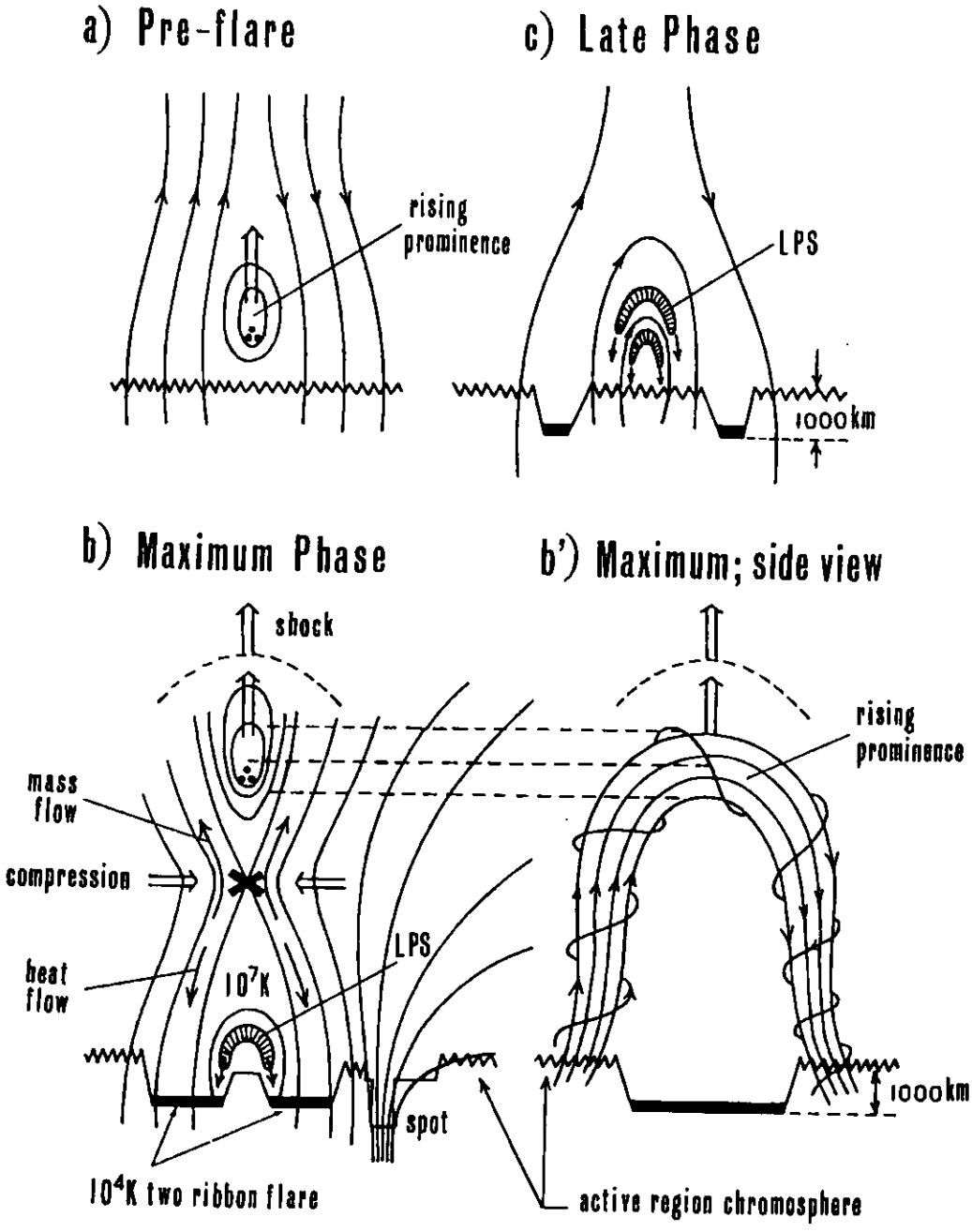

Figure 1.8: Schematic pictures of LDE flares. Thin lines denote magnetic field lines (Hirayama 1974).

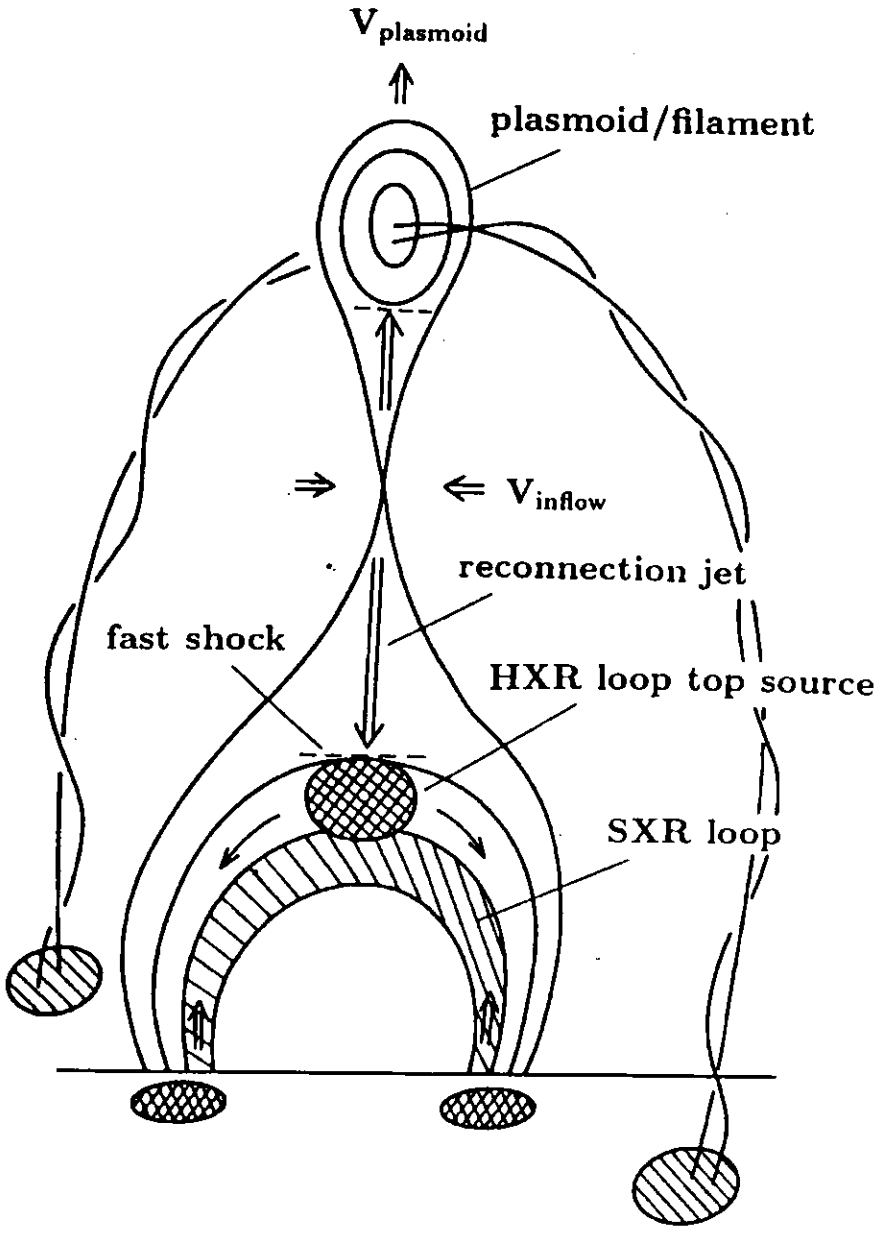

Figure 1.9: Schematic picture of both impulsive and LDE flares. This model developed from the CSHKP model gives a unified view of the two groups of flares. (Shibata et al. 1995).

phenomenon is thought as follows: (1) High energy electrons rush into dense layers, and cause microwave and hard X-ray emissions by gyro-synchrotron emission and non-thermal Bremsstrahlung. (2) The chromosphere is heated by these penetrating electrons to more than 10^7 K and it evaporates upwards in the corona with at the sound speed. This is called *chromospheric evaporation*. (3) Closed magnetic loops filled with hot dense plasma can be observed in soft X-rays. Antonucci et al. (1982) and Tanaka et al. (1982) supported this scenario using data from the *SMM* and *Hinotori*. Strong blue-shifts of the Fexxv resonance line during hard X-ray bursts correspond to upward flows of up to 400 km s^{-1}. More recent observations from the *Solar and Heliospheric Observatory* (*SOHO*) (Domingo et al., 1995) show similar phenomena in further detail. Czaykowska et al. (1999) reported that relatively strong blue-shifts were observed at the outer foot-points of a two-ribbon flare during the decay phase by the Coronal Diagnostic Spectrometer (CDS).

Hot Thermal Plasmas

Lin et al. (1981) first observed a high-temperature component in solar flares by a balloon-borne spectrometer equipped with cooled germanium planar detectors of high energy resolution (FWHM $\leq$ 1 keV). Since this component was characterized by an extremely steep spectrum in hard X-ray (10 - 20 keV) region, he deduced that hot component came from thermal plasma with a maximum temperature of $\leq 34 \times 10^6$ K and an emission measure of 2.9 $\times 10^{48}$ cm^{-3}. The hot thermal (often called superhot) component first appeared at the maximum phase and continued to the decay phase. Tanaka (1986) observed a similar hot component of Te $\approx 30 \times 10^6$ K by the Bragg spectrometers aboard the *Hinotori*. Plasma properties were derived from soft X-ray diagnostics of Fexxvi and Fexxv lines. These components were also observed with the *Yohkoh* Bragg Crystal Spectrometer (BCS) (Culhane et al., 1991) (Fig.1.10). Moreover, using the *Yohkoh* SXT, a thermal plasma region, in which the temperature and the density were 15–20 K and 10^{11} cm^{-3}, was found near the loop top where the hard X-ray loop top sources are located (Masuda et al., 1994; Tsuneta et al., 1997a; Nitta & Yaji, 1997; Doschek, 1999; Nitta & Yaji, 1997). Recently, Warren et al. (1999) reported that the superhot components observed by *Yohkoh* were also consistent with the observations of the *Transition Region and Coronal Explorer* (*TRACE*) satellite (Handy et al., 1999). Since two temperature maxima, which could correspond to the slow shock location, were observed at the 13 January 1992 flare, Tsuneta et al. (1997a) suggested the heating mechanism of the superhot component to be the slow shock heating along the reconnected field lines.

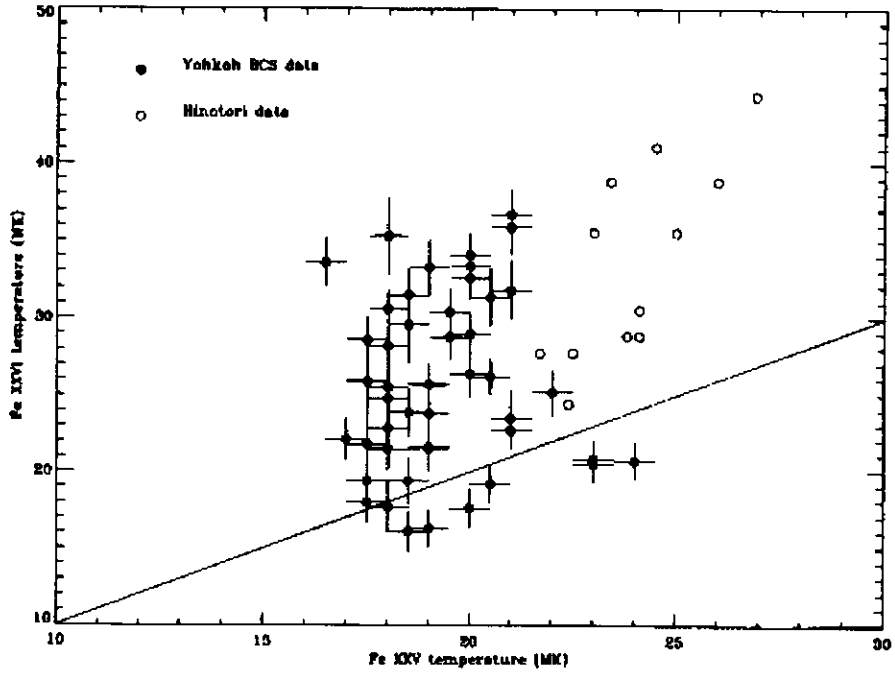

Figure 1.10: Plot of temperature from the Fexxvi spectra against those from the Fexxv spectra. Points (*open circles*) from the *Hinotori* flares discussed by Tanaka (1986) are included. (Pike et al. 1996).

1.5 Purpose of This Thesis

1.5.1 Flare Associated Ejecta and High-Temperature Regions

Although the *Yohkoh* mission revealed important findings via valuable observations, there are still many questions remaining in the flare physics. Especially, a big discrepancy that still exists between observations and theories is the speed of X-ray plasma ejecta. The average velocity of the X-ray plasma ejecta from observation ($\sim$ 300 km s^{-1}) is much slower than that estimated from the model ($V_A \sim$ 3000 km s^{-1}). Further, Shibata et al. (1995) and Magara et al. (1997) proposed that many kinds of ejecta are triggered in flares, however, no clear relationship was found between ejecta and flares. With regard to hot components observed with the SXT, little is known about the detailed physical conditions of the heating process. To begin with, some people consider it dubious that hot components observed by the SXT are similar to the super-hot thermal sources observed by Lin et al. (1981) and Tanaka (1986). Because the accuracy of temperature map produced by SXT may be affected by several factors, and, some of them are ambiguous, only a few events have been analyzed thus far. Moreover, the relationship between hot components seen in SXT and hard X-ray loop top source seen in HXT has not yet been established.

If both the hot component and the hard X-ray source originate from thermal emissions, no explanation is yet given to the fact that the temperature difference between the two sources reaches an order of magnitude.

1.5.2 Construction of This Thesis

In this thesis, we would like to confirm that the hot components observed by the SXT are real structures, and to investigate their physical characteristics. First, we evaluate the errors in the SXT temperature maps in chapter 2. In chapter 3, we discuss the physical parameters of the hot components above the loop tops. Finally, taking global magnetic structures around the flare regions into account, we compare the observations with the flare models in chapter 4.

References

Acton, L. W. 1968, ApJ, 152, 305

Antonucci. E., Gabriel, A. H., Acton, L. W., Culhane, J. L., Doyle, J. G., Leibacher, J. W., Machado, M. E., Orwing, L. E., & Dennis B. R. 1982, Sol. Phys., 78, 107

Brown, J. C. 1971, Sol. Phys., 18, 489

Bruzek, A. 1964, ApJ, 140, 746

Carmichael, H. 1964, in *AAS-NASA Symposium on Solar Flares*, ed. W. N. Hess (NASA SP-50), 451

Carrington, R. 1859, MNRAS, 20, 13

Chipman, E. G. 1981, ApJ, 244, l113

Crannell, C. J., Frost, K. J., Matzler, C., Ohki, K., & Saba, J. L. 1978, ApJ, 223, 620

Culhane, J. L., Hiei, E., Doschek, G. A., Cruise, A. M., Ogawara, Y., Uchida, Y., Bentley, R., Brown, C. M., Lang, J., Watanabe, T., et al. 1991, Sol. Phys., 136, 89

Czaykowska, A., De Pontieu, B., Alexander, D., & Rank, G. 1999, ApJ, 521, L75

Dennis, B. R. Sol. Phys., 100, 465

Domingo, V., Fleck, B., & Poland, A. I. 1995, Sol. Phys., 162, 1

Doschek, G. A. 1999, ApJ, 527, 426

Duijveman, A., Hoying, P., & Machado, M. E. 1982, Sol. Phys., 81, 137

Dungey, J. W. 1958, in *Electromagnetic phenomena in cosmical physics*, Proc. IAU Symp. no.6, ed B. Lehnert, p135

Frost, K. J. 1969, ApJ, 158, L159

Gaizauskas, V. 1989, Sol. Phys., 121, 135

Giovanell, R. G. 1946, Nature, 158, 81

Gold, T., & Hoyle, F. 1960, MNRAS, 120, 89

Gosling, J. T., Hildner, E., MacQueen, R. M., Munro, R. H., Poland, A. I., & Ross, C. L. 1974, J. Geophys. Res., 79, 4581

Gosling, J. T., Hildner, E., MacQueen, R. M., Munro, R. H., Poland, A. I., & Ross, C. L. 1976, Sol. Phys., 48, 389

Handy, B. N., et al. 1999, Sol. Phys., 187, 229

Harrison, R. A., Hildner, E., Hundhausen, A. J., Sime, D. G., & Simnett, G. M. 1990, J. Geophys. Res., 95, 917

Heyvaerts, J., Priest, E. R., & Rust, D. M. 1997, ApJ, 216, 123

Hirayama, T. 1974, Sol. Phys., 34, 323

Hoyng, P., Machado, M. E., Duijveman, A., Boelee, A., de Jager, C., et al. 1981, ApJ, 244, L153

Howard, R., Sheeley, N. R., Koomen, M. J., & Michels, D. J. 1985, J. Geophys. Res., 90, 8173

Hudson, H., 1994, in *Proc. of Kofu Meeting*, eds. S. Enome, & T. Hirayama, Nobeyama Radio Observatory Report No. 360. p1

Hundhausen, A. J. 1988, in *Proc. of the Sixth International Solar Wind Conference*, TN306+Proc, eds. V. Pizzo, T. E. Holzer, & D. G. Sime, National Center for Atmospheric Research, Boulder, pp. 181

Hundhausen, A. J., Burkepile, J. T., & St. Cyr, O. C. 1994, J. Geophys. Res., 99, 6543

Kahler, S. 1977, ApJ, 214, 891

Kane, S. R. 1969, ApJ, 157, L139

Kopp, R. A., & Pneuman, G. W. 1976, Sol. Phys., 50, 85

Kosugi, T., Makishima, K., Murakami, T., Sakao, T., Dotani, T., Inda, M., Kai, K., Masuda, S., Nakajima, H., Ogawara, Y., Sawa, M. & Shibasaki, K. 1991, Sol. Phys., 136 17

Lin, R. P., Schwartz, R. A., Pelling, R. M., & Hurley, K. C. 1981, ApJ, 251, L109

MacQueen, R. M., Eddy, J. A., Gosling, J. T., Hildner, E., Munro, R. H., Newkirk, G. A., Poland, A. I., & Ross, C. L. 1974, ApJ, 187, L85

Magara, T., Shibata, K., & Yokoyama, T. 1997, ApJ, 487, 437

Makishima, K. 1982, in *Proc. Hinotori Symp. on Solar Flares*, eds. Tanaka, Y., Tanaka, K., Matsuoka, M., Ohki, K., Kondo, I., Hirayama, T., & Nishi, K., p120

Martin, S., F., & Ramsey, H., E. 1972, in *Solar Activity Observations and Predictions*, ed. McIntosh, P. S., & Dryer, M., (Cambridge: MIT Press), p371

Masuda, S., Kosugi, T., Hara, H., Tsuneta, S., & Ogawara, Y. 1994, Nature, 371, 495

Moore, R., McKenzie, D. L., Svestka, Z., et al. 1980, in *Solar Flares*, eds, P.A. Sturrock, Colorado Associated University Press, Boulder, CO

Neupert, W. M. 1968, ApJ, 153, L59

Nitta, N., & Yaji, K. 1997, ApJ, 484, 927

Nitta, N., Sato, J., & Hudson, H. 2001, ApJ, in press

Nishio, M., Yaji, K., Kosugi, T., Nakajima, H., & Sakurai, T. 1997 ApJ, 489, 976

Oda, M. 1983, *Adv. Space Res.*, 2, No.4, 207

Ohyama, M., & Shibata, K. 1997 PASJ, 49, 249

Ohyama, M., & Shibata, K. 1998 ApJ, 499, 934

Ogawara, Y., Takano, T., Kosugi, T., Tsuneta, S., Watanabe, T., Kondo, I. & Uchida, Y. 1991, Sol. Phys., 136, 1.

Pallavicini, R., Serio, S. & Vaiana, G. S. 1977, ApJ, 216, 108

Pallavicini, R., & Vaiana, G. S. 1980, Sol. Phys., 67, 127

Peterson, L. E., & Winckler, J. R. 1959, J. Geophys. Res., 64, 697

Petschek, H., E. 1964, in *AAS-NASA Symposium on Solar Flares*, ed. W. N. Hess (NASA SP-50), 425

Pike, C. D., Phillips, K, J, H,, Lang, J., Sterling, A., Watanabe, T., Hiei, E., Culhane, J. L., Cornille, M., & Dubau, J. 1996, ApJ, 464, 487

Rompolt, B. 1990, *Hvar Obs. Bull.*, 14, 37

Sakao, T., Kosugi, T., & Masuda, S. 1998, in *Observational Plasma Astrophysics: Five Years of Yohkoh and Beyond*, eds. T. Watanabe, T. Kosugi, & A. C. Sterling, p 273

Severny, A. B. 1958, *Izu. Krym. Astrofiz. Obs.* 1 102

Sheeley, M. R. Jr., Bohlin, J. D., Brueckner, G. E., Purcell, J. D., Scherrer, V. E., Tousey, R., Smith, J.B. Jr., Speich, D. M., et al. 1975, Sol. Phys., 45,377

Shibata, K., Masuda, S., Shimojo, M., Hara, H., Yokoyama, T., Tsuneta, S., Kosugi, T., & Ogawara, Y. 1995, ApJ, 451, L83

Smith, S. F., & Ramsey, H. E. 1964, ApJ, 60, 1

Sturrock, P. A. 1966, Nature, 211, 695

Svestka, Z., Farnik, F., Hudson, H., Uchida, Y., Hick, P., & Lemen J. R. 1995, Sol. Phys., 161, 331

Sweet, P. A. 1958, IAU Symp. No. 6, 123

Takakura, T. 1969, Sol. Phys., 6, 122

Takakura, T. 1983, ApJ, 270, L83

Tanaka, K., Watanabe, T., Nishi, K., & Akita, K. 1982, ApJ, 254, L59

Tanaka, K. 1986, PASJ, 38, 225

Tanaka, Y. 1983, Sol. Phys., 86, 3

Tsuneta, S., Acton, L., Bruner, M., Lemen, J., Brown, W., Caravalho, R., Catura, R., Freeland, S., Jurcevich, B., Morrison, M., Ogawara, Y., Hirayama, T., & Owens, J., 1991, Sol. Phys., 136, 37.

Tsuneta, S., Hara, H., Shimizu, T., Acton, L., Strong, K., Hudson, H., & Ogawara, Y. 1992 PASJ, 44, L63

Tsuneta, S., Masuda, S., Kosugi, T., & Sato, J. 1997, ApJ, 478, 787

Tsuneta, S., 1997, ApJ, 484, 507

Van Beek, H., Hoyng, P., Lafleur, B., & Simnett, G. M. 1980, Sol. Phys., 65, 39

Warren, H. P., Bookbinder, J. A., Forbes, T. G., Golub, L., Hudson, H. S., Reeves, K., & Warshall, A. 1999, ApJ, 527, L121

Warwick, J. W. 1957, ApJ, 125, 5811

Webb, D. F., Krieger, A. S., & Rust, D. M. 1976, Sol. Phys., 48, 159

Zirin, H., & Tanaka, K. Sol. Phys., 32, 173

Zirin, H., MacKinnon, A., & Mackenna-Lawlor, S. M. P. 1990, in *Solar Interior and Atmosphere*, ed. A. N. Cox, W. C. Livingston, M. S. Matthews, the University of Arizona Press, 964

Chapter 2

Evaluation of Temperature Maps Observed with the YOHKOH SXT

2.1 Introduction

2.1.1 Yohkoh Satellite

Yohkoh (Ogawara et al., 1991) was launched on 30 August 1991 as the second Japanese solar-observing satellite following *Hinotori*. Since one of the scientific targets of *Yohkoh* is to investigate high energy phenomena related to solar flares, a coordinated set of four capable instruments for the flare observation were carried on board: the Hard X-ray Telescope (HXT), the Soft X-ray Telescope (SXT), the Bragg Crystal Spectrometer (BCS), and the Wide Band Spectrometer (WBS). Two of the instruments, used in this paper for obtaining images and temperature maps of flares, are described in detail in this chapter.

2.1.2 Soft X-ray Telescope aboard Yohkoh

The Soft X-ray Telescope (SXT) (Tsuneta et al., 1991) is a modified Wolter I grazing-incidence telescope with a basically hyperboloid-hyperboloid mirror configuration. The detector of SXT is a CCD camera with 1024 $\times$ 1024 pixel. The pixel size corresponds to an angular size of 2.46 arcsec. Since a single X-ray photon at 10 Å creates about 200 electrons, the SXT CCD can observe 1000 X-ray photons without saturation. The data number (DN) is so defined as to correspond to 100 electrons detected by the CCD.

SXT has two filter wheels. One contains metal filters to reflect visible light on the filter surface, and to transmit X-rays in the limited wavelengths ranges. Pairs of X-ray images with two different filters are used as a method for plasma diagnostic observations. Fig. 2.1 shows the effective area of the SXT for six kinds of filters. If we define the Data

Number (DN): $DN_i \equiv N_i \cdot \delta t/100$, where δt is the exposure duration, DN_i is expressed as

$$DN_i = F_i(T) \cdot VEM \cdot \delta t, \tag{2.1}$$

where $F_i(T)$ is a function of temperature, including all the instrumental and observational factors, and VEM is the volume emission measure. Fig.2.2 shows the response of the SXT ($F_i(T) \cdot VEM$) for the volume emission measure of 10^{44} cm^{-3} as a function of a plasma temperature.

2.1.3 Filter Ratio Method

The temperature and emission measure are obtained from images taken with two different X-ray broad-band filters. This is called the *filter ratio method* (Hara, 1992a; Hara et al., 1992b). The intensity ratio (R_{ij}) of images taken with two different metal filters (i and j) is written as

$$R_{ij} \equiv \frac{DN_i/\delta t_i}{DN_j/\delta t_j} = \frac{F_i(T)}{F_j(T)}. \tag{2.2}$$

Since equation 2.2 indicates that the ratio is only a function of the temperature, plasma temperatures can be derived by the filter ratio method. Fig. 2.3 shows the temperature dependence of filter ratios for various filter pairs.

2.1.4 Point Spread Function

The Point Spread Function (PSF) of the telescope shows scattering effect of the incidence photons caused by micro-roughness of the mirrors and mid frequency figure shape errors, as well as a core defined by the mirror figure itself. The PSF is a function of wavelength and off-axis distance. Since the X-ray spectrum varies with plasma temperature, radial X-ray intensity distributions also depend the temperature.

Actual soft X-ray images observed by SXT are convolved with the X-ray source distributions as well as the PSF of the telescope. The PSF of the grazing-incidence telescope consists of a roughly Gaussian core component and a power-law wing component (Fig.2.4). Hara et al. (1994) estimated the characteristics of wing part of the SXT PSF with the Al 1265 Å filter, using post-launch data which included intense point-like flares. They found that the wing behaves as r^{-2} for r $>$ 200 arcsecs. The wing part of the PSF appears to be connected smoothly at $r \sim 20$ - 50 arcsecs to the core of the PSF derived from the pre-launch calibration data (See Fig.2.5). Martens et al. (1995) described the calibration of the PSF from the pre-launch data.

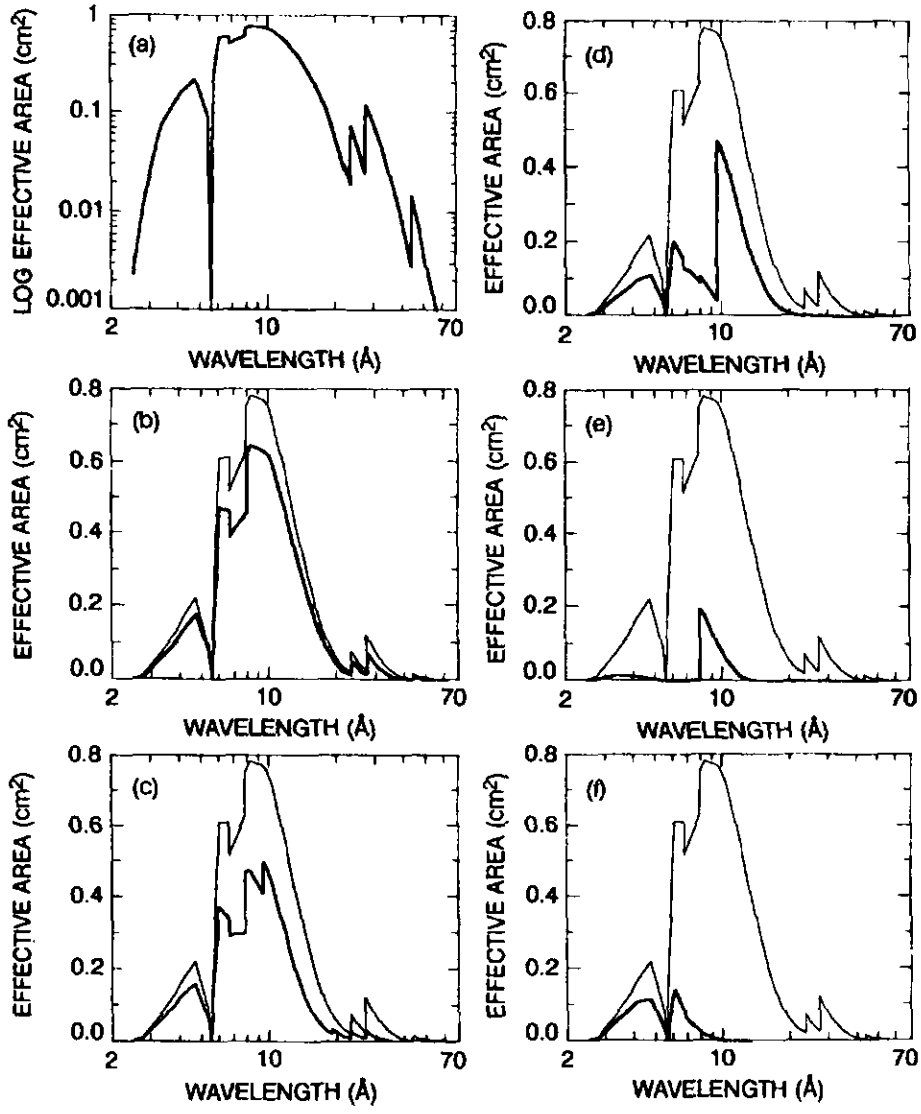

Figure 2.1: Effective area of the SXT: (a) no back, (b) Al 1265 Å, (c) AlMgMn, (d) Mg 2.52 μm, (e) Al 11.6 μm, and (f) Be 119 μm (Tsuneta et al. 1991).

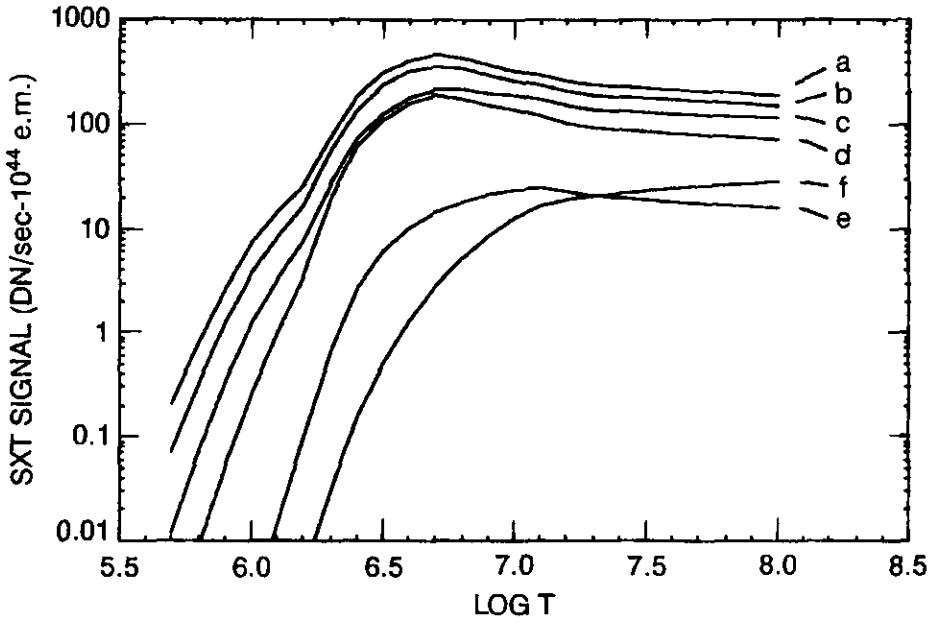

Figure 2.2: Response of SXT $(F_i(T) \cdot VEM)$ for the volume emission measure (VEM) of 10^{44} cm^{-3} as a function of a plasma temperature. The labeling is the same as Fig. 2.1 (Tsuneta et al. 1991).

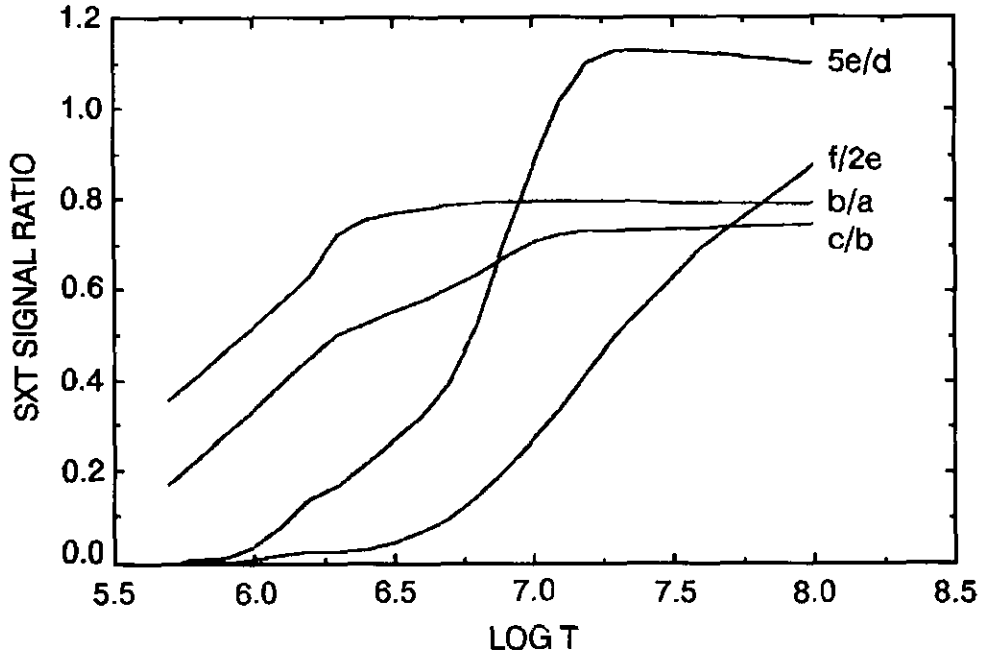

Figure 2.3: Ratio of the SXT response functions. The labeling are the same as in Fig.2.1 (Tsuneta et al. 1991).

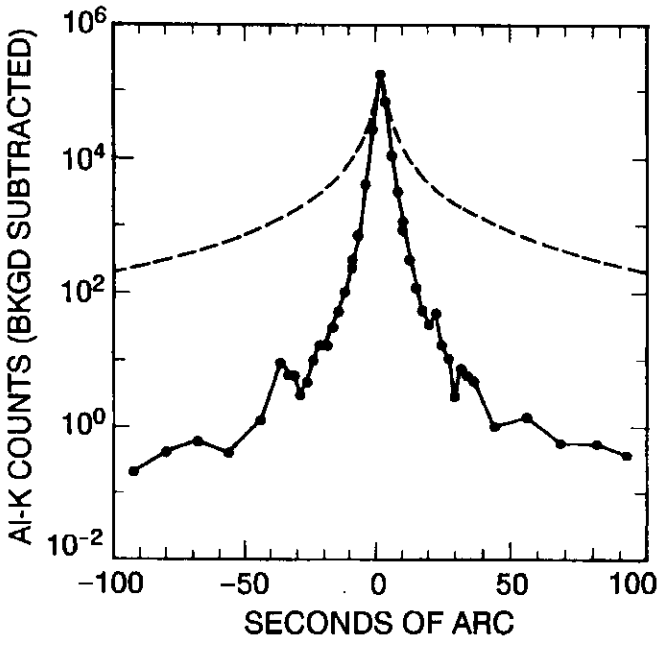

Figure 2.4: Point spread function of SXT at 8.34 Å for 1 arcsec source at 310 m. A dashed line shows the PSF of *Skylab* S0-54 telescope (Vaiana et al., 1977) (From Tsuneta et al. 1991).

Although the wing part PSF level of the SXT is much lower than that of the Skylab telescope (Fig. 2.4), scattered X-rays from bright regions are not negligible.

2.2 Errors in Temperature Map

Errors in the temperature map mainly originate from scattered light, which depends on the filter and source positions, and from jittering motions of the spacecraft during the observation. The correction procedures of the both errors is described, which might still include errors in temperature estimate.

2.2.1 Alignment of Images

Jitter of Satellite Pointing

We calibrate the SXT data using the software SXT_PREP procedure for decompression, dark current and pin hole leak subtractions, identification of saturated pixels, and pointing interpolation. The spacecraft pointing is determined by using ACS (Attitude Control System) and Hard X-ray Aspect sensor (HXA) onboard and in the attitude (ATT) database.

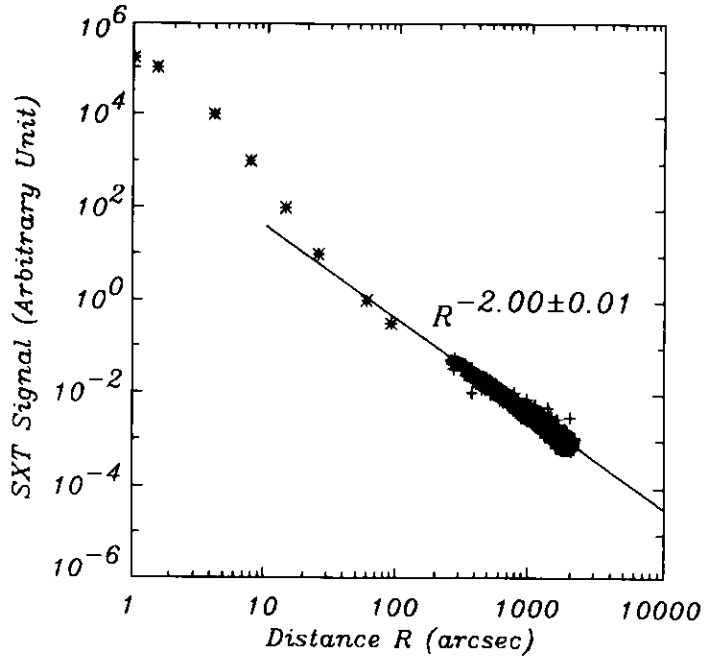

Figure 2.5: Point spread function of SXT derived from post-launch observational data (*crosses*) and from calibration data (*asterisk*; Tsuneta et al. 1991). The solid line shows the fitting for the halo component by the lease-squares method (Hara et al. 1994).

Inertia Reference Unit (IRU) detects short time-scale vibrations by using the gyroscopes. The time resolution of IRU data is 0.25 s, and an angle increment pulse is generated every 0.08 arcsec. Siarkowski et al. (1996) pointed out large excursion of the satellite pointing during the periods of frequent filter exchanges. These filter-wheel motions cause periodic changes of satellite pointing, as shown in Fig.2.6. Fig.2.6 shows IRU data (marked by plus) at the 13 January 1992 flare. Black circles and black squares stand for the exposure timings with the Be119 and the Al12 filters, respectively. Spacecraft jitters are directly related to filter exchange cadence. The spacecraft attitude moves from $-1.0''$ to $0.9''$ off, but it is only in $0.5'' \sim 0.7''$ at exposures with Be119 filter, and $-0.4'' \sim -0.2''$ at exposures with Al112 filter. Since full-resolution images are used in this analysis, the spacecraft motions should be corrected less than one tenths of the pixel size. HXA measures the solar direction by observing the solar limb. Because the gyro attitudes drift with time, it is necessary to calibrate a long time-scale movement of the satellite using the HXA data. Time resolution and position accuracy of HXA are about 1 minute and 2 arcsec, respectively.

Siarkowski et al. (1996) also reported that even after the SXT_PREP procedure the maximum error of about 0.5 pixels might remain. Although their results are not entirely

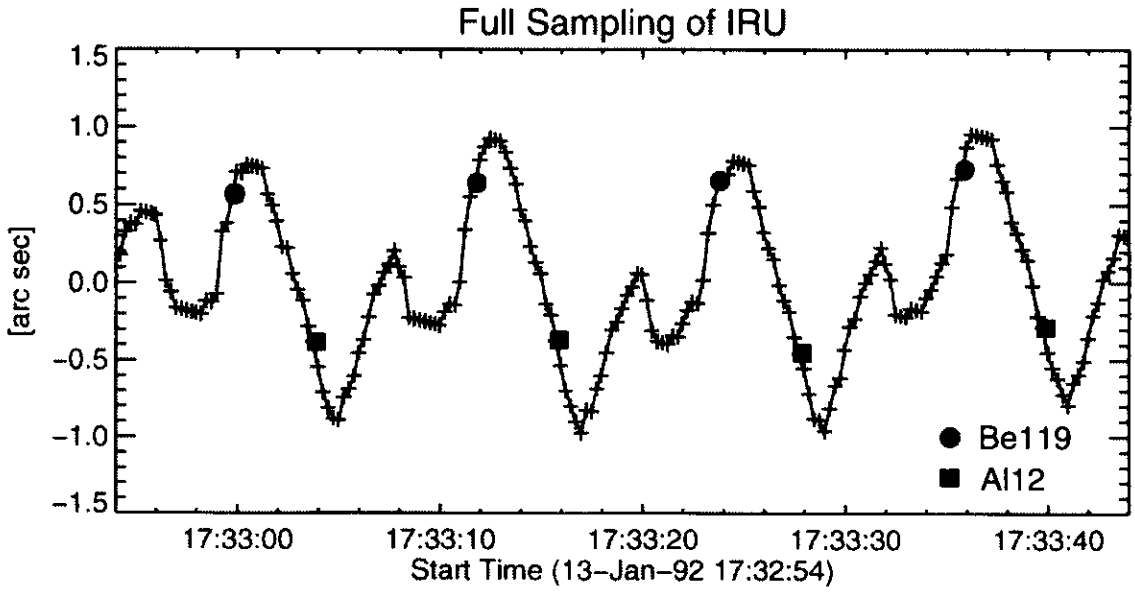

Figure 2.6: Time profile of IRU data of 13 January 1992 flare. A black circle and a black square show pointing jitter of Be119 filter and Al12 filter, respectively.

correct, pointing jitters are estimated from the coaligned images by different filters. It is clear in Fig.2.1 that when high temperature plasmas exist, the telescope wavelength responses are greatly varied with filters. Fig.2.7 shows the intensity profiles of both Be119 and Al 1265 images and the temperature profiles at the 13 January 1992 flare. Along the line indicated at the upper right corner of the top panel, the intensities are plotted normalized to the maximum intensity in each image. Solid and dashed lines are intensities of the Be119 and the Al12 images. Since the footpoint of flare loop is located at the left side, it is the loop top side that the slope of Be119 is more gradual than that of Al 1265. No slopes obtained from the two different filters could coincide to each other on either side, if the alignment would be simply corrected by about 0.5 pixel.

Error Estimation of Observed Images

In the previous section, the positioning error of images effective in our analysis should be about 0.1 pixel or less. In this section, we evaluate the error in temperature due to this pointing shifts of about 0.1 pixel. Fig.2.8 shows SXT temperature maps for the 13 January flare. The Be119 images are artificially shifted by 0.1 pixels to each direction. The center image has no shift. In each image, the average temperatures of the high temperature regions are indicated, and the area of the high temperature regions and the flare loops are shown by white and black lines, respectively. The exact definitions of the

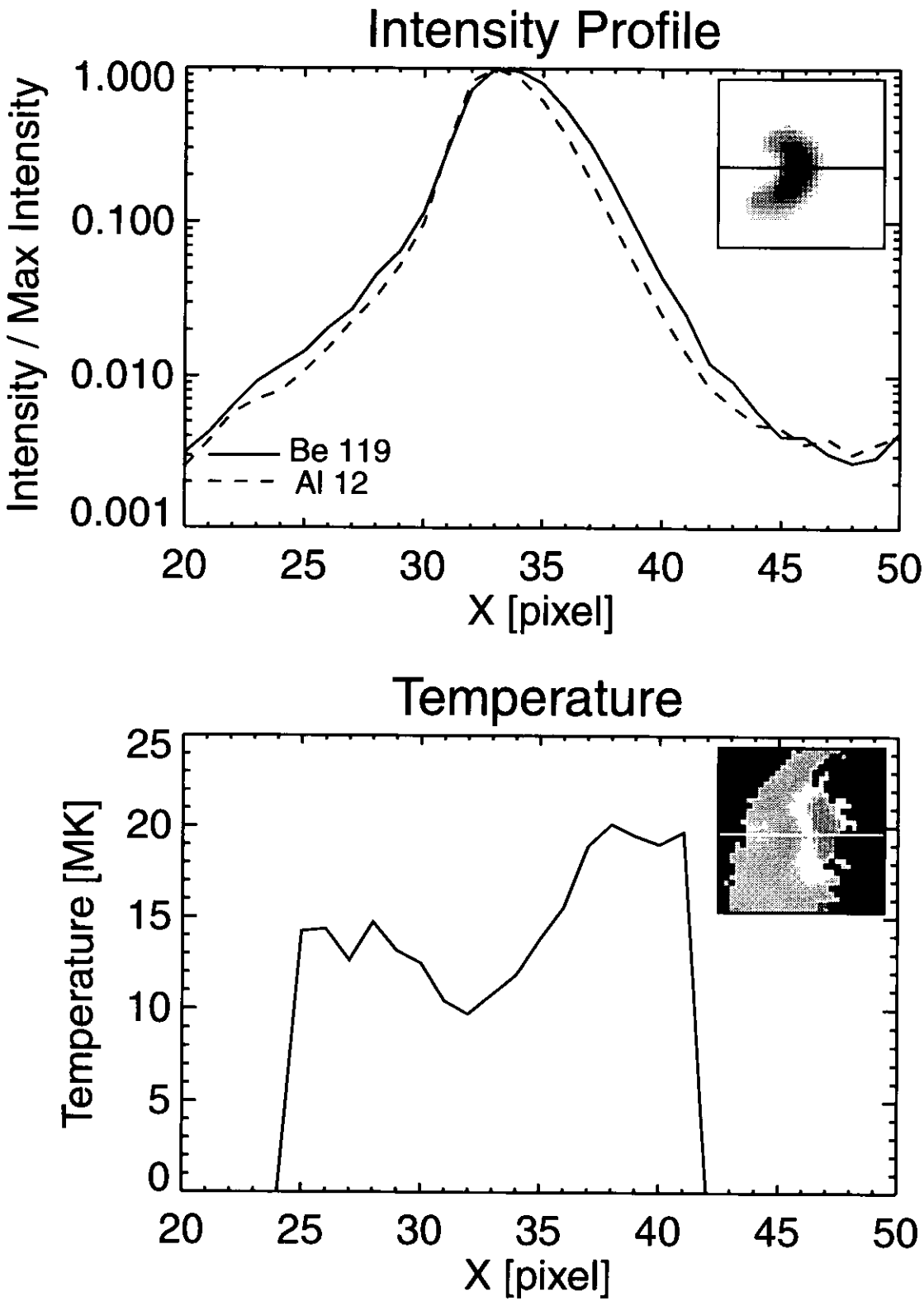

Figure 2.7: Profile of intensity and temperature of 13 January 1992 flare along the line indicated at the upper right corner of each panel. In the top panel, intensities are normalized to the maximum intensity. Solid and dashed lines are intensities of the Bel19 and the Al12 images, respectively. Lower panel shows the same of the temperature structure.

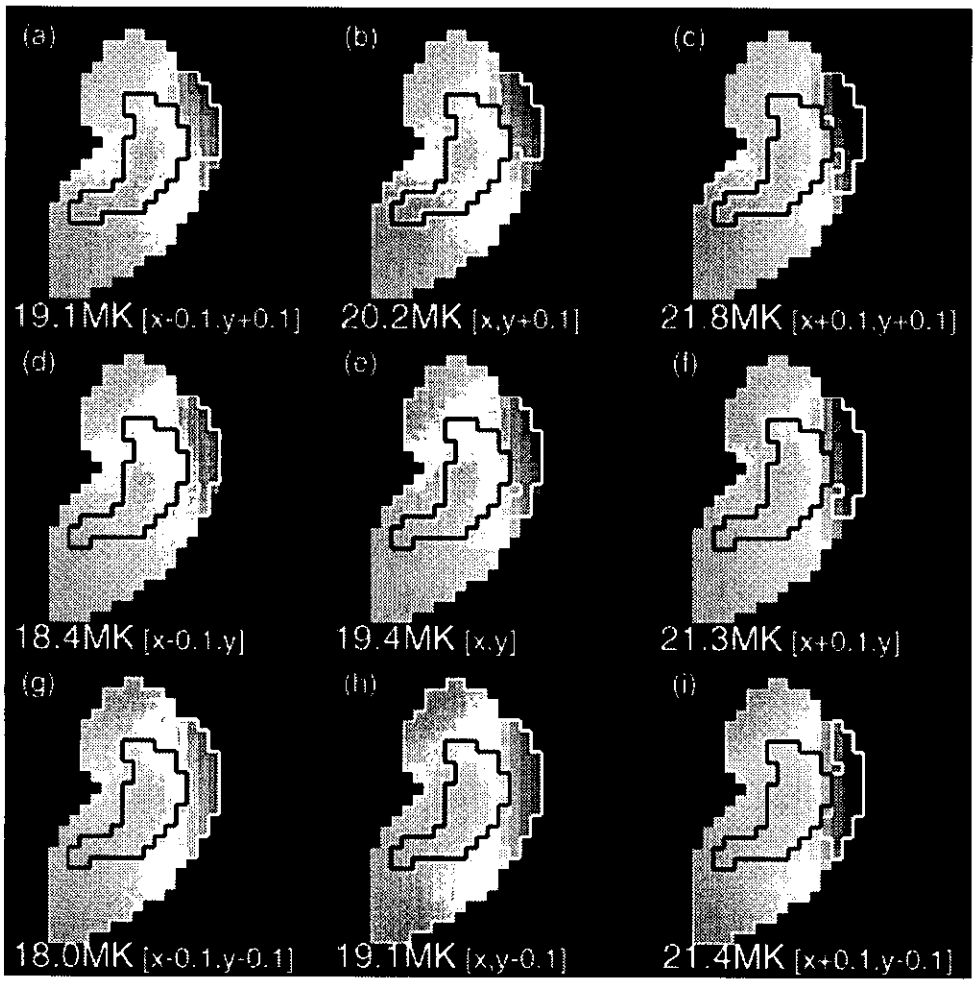

Figure 2.8: Effect of possible mis-alignment of the images of 13 January 1992 flare. The Be 119 filter images are artificially shifted by 0.1 pixels to the corresponding directions – The center map has no shift. In each map, the maximum temperature is indicated.

high temperature region and the flare loop are described in chap. 3. From Fig.2.8 we estimate the error in temperature to about 2 MK at 20 MK, if the accuracy of alignment is about 0.1 pixel.

2.2.2 Motion of Flares

Generally, the flare loop is observed to rise as the flare progresses. Temperature maps used in this study are obtained from the integrated images taken about 2 minutes apart. We know from our analysis, in chap. 3 of this thesis, that the average rising speeds of flares and high-temperature regions are about 5 km s^{-1} and about 15 km s^{-1}, respectively (see the details in chap. 3). Accordingly, the high-temperature regions move about 1800

km for 2 minutes. Since one pixel size for SXT full resolution is about 1700 km, high-temperature plasmas transit a SXT pixel for 2 minutes. Therefore, errors introduced by intrinsic plasma motions are negligible.

2.2.3 Scattered Light

Characteristics of PSF

Scattered light correction is one of the important processes we need to take into account, when we make temperature maps. Strong emissions from the flare kernel influence the derived temperatures of the faint structures around the flare loop, such as high-temperature regions we analyse in chap. 3.

We summarize here the major characteristics of the SXT PSF.

1. The PSF of SXT consists of a Gaussian core and a power-law wing component (see Fig.2.4).
2. Acton reported that azimuthal angle dependence is little.
3. Therefore, PSF is the function of wavelength, distance from the source (see Fig.2.4), and position on CCD.
4. As for the core component, Martens et al. (1995) analysed using the pre-launch data. No strong filter-dependence was found in the core part.
5. For the wing part, no pre-launch data was available. Hara et al. (1994) estimated the wing part of PSF with the Al 1265 Åfilter, using the post-launch data. The functional shape is a power law, and it is regarded as r^{-2} in the distance range from 20 – 50 arcsec to 200 arcsec (see Fig.2.5).
6. Generally, PSF with the shorter-wavelength filter has stronger wing components.
7. Thus, the strength of the wing part of PSF differs from filter to filter.

Scattered Light Considerations in Other Studies

Tsuneta et al. (1997a) estimated the scattered photon intensities from the wing component of the PSF function given by Hara et al. (1994). They defined the scattering ratio, which is the ratio of the signal in a pixel to that all scatter light signals in the the field of view of the PFI image. They used only the pixels in which the scattering ratio were below 15 %. In the case of flare study this method of estimate is not exact, because flare images are

not taken with the Al 1265 Åfilter. We need to estimate the wing parts of the PSF with the Be119 and Al112 filters. Another approach to estimate the level of scattered light is a deconvolution (super-resolution) technique. Although Shin (1998) investigated the error of scattered photons from bright soft X-ray loops using a deconvolution technique, the concrete analysis method has not been established yet.

2.3 Evaluation of PSF

2.3.1 Contribution of Wing Part of PSF

Fig.2.9 shows the distances between the center-of-gravity point of the high-temperature region and the pixel of maximum intensity in the images we use in chap. 3. They are taken at the time of hard X-ray peaks. We can see from this figure that most of the high-temperature regions we are interested in, are located less than 30 arcsec away from the brightest point in the flares. The wing part of the PSF exceeds the PSF core at about 20 – 50 arcsec from the brightest point (Hara et al., 1994). Considering the sizes of the brightest flare loops, we can say that the high-temperature regions are located in the areas where scattered lights are originated from the core part of the PSF, which was precisely analysed and determined by the pre-launch calibration data of the SXT (Martens et al., 1995). For more distant faint structures, the wing part should be taken into account.

2.3.2 PSF Obtained from SXT_PSF Procedure

Martens et al. (1995) estimated the core part of the PSF by fitting the experiment data with the Moffat function. The original Moffat function is axially symmetric around its maximum,

$$G(r) = \frac{c}{(1 + (\frac{r}{a})^2)^b} \tag{2.3}$$

where r is the distance from the peak , a, b, and c are parameters. The best fits of the PSF parameters for scattering experiments are summarized in the table 2.1 as well as parameters that we use in this study.

When we use PSF derived from SXT_PSF, a significant negative value appears around the edge of flare loops for Al12 data after the deconvolution process, in which fast Fourier transform (FFT) is used (see Fig. 2.11). This is due to the slow decrease of the PSF wing. We increased the parameter b for the Al12 filter step by step without changing the parameter until the significant negative values around the edge of the flare loops disappear.

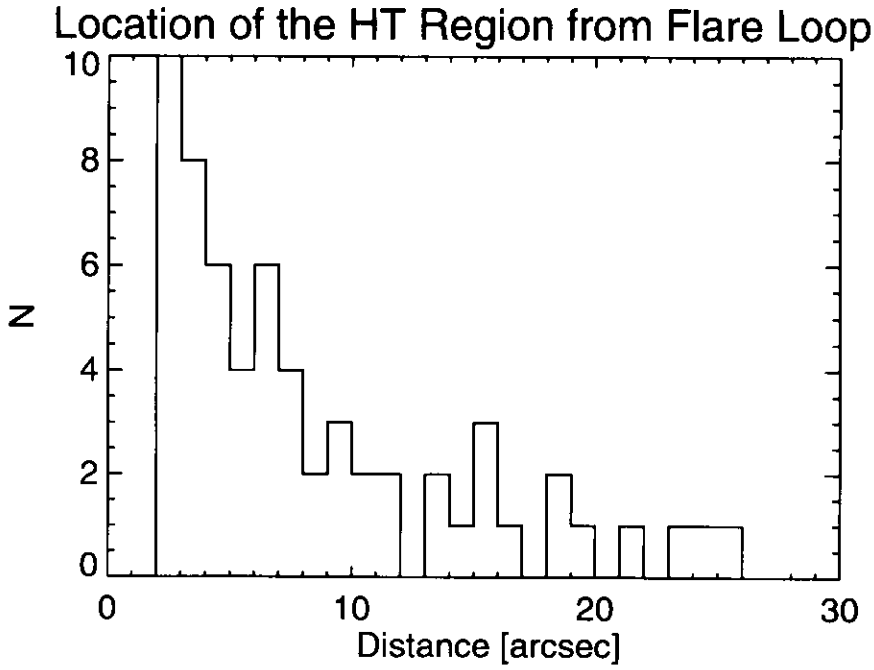

Figure 2.9: Histogram of location of the high-temperature region from flare loop.

Table 2.1: PSF Function from Martens et al. (1995)

Point Spread Function		$\mathrm{PSF}(r) = \frac{1}{\left(1+(\frac{r}{a})^2\right)^b}$	
Parameter		a	b
Ag-L 4.16 Å	experiment	1.10 ± 0.23	1.77 ± 0.24
Al-K 8.34 Å	experiment	0.68 ± 0.24	1.45 ± 0.21
C-K 44.7 Å	experiment	1.10 ± 0.24	1.45 ± 0.21
Be filter	in SXT_PSF	0.88	1.60
Al filter	in SXT_PSF	0.63	1.40
Be filter	this study	0.88	1.60
Al filter	this study	0.63	1.52

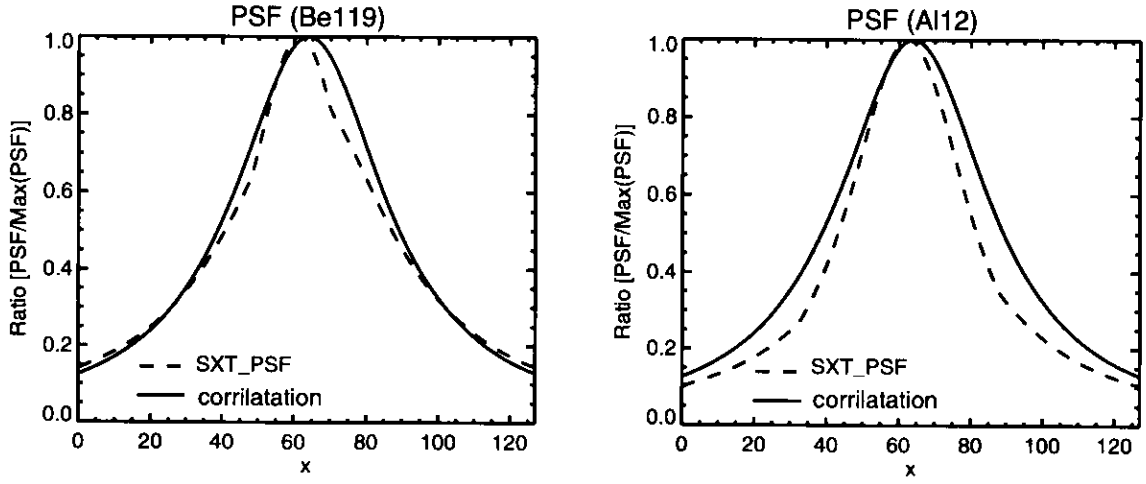

Figure 2.10: PSF of 13 January 1992 flare. Dashed lines show PSF obtained from SXT_PSF procedure, and solid lines indicate PSF that we use in this study.

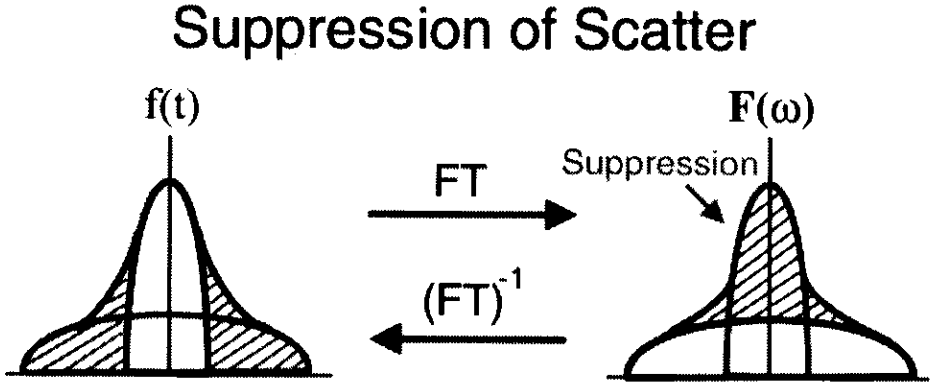

Figure 2.11: Schematic picture of deconvolution process

Thus, SXT_PSF procedure, which is included in the *Yohkoh* software, is slightly modified in this study as shown in the table 2.1 and in Fig.2.10. The parameters of SXT_PSF in this table are those for 10 million degree plasma. Although there is a very weak temperature dependence in the PSF shape, we do not consider it in our flare study, because the flare temperatures that we studied here are in a limited range from 8 to 20 million degrees in which these PSF parameters are considered to be almost constant. Dashed lines in Fig.2.10 show the modified PSF. in table2.1.

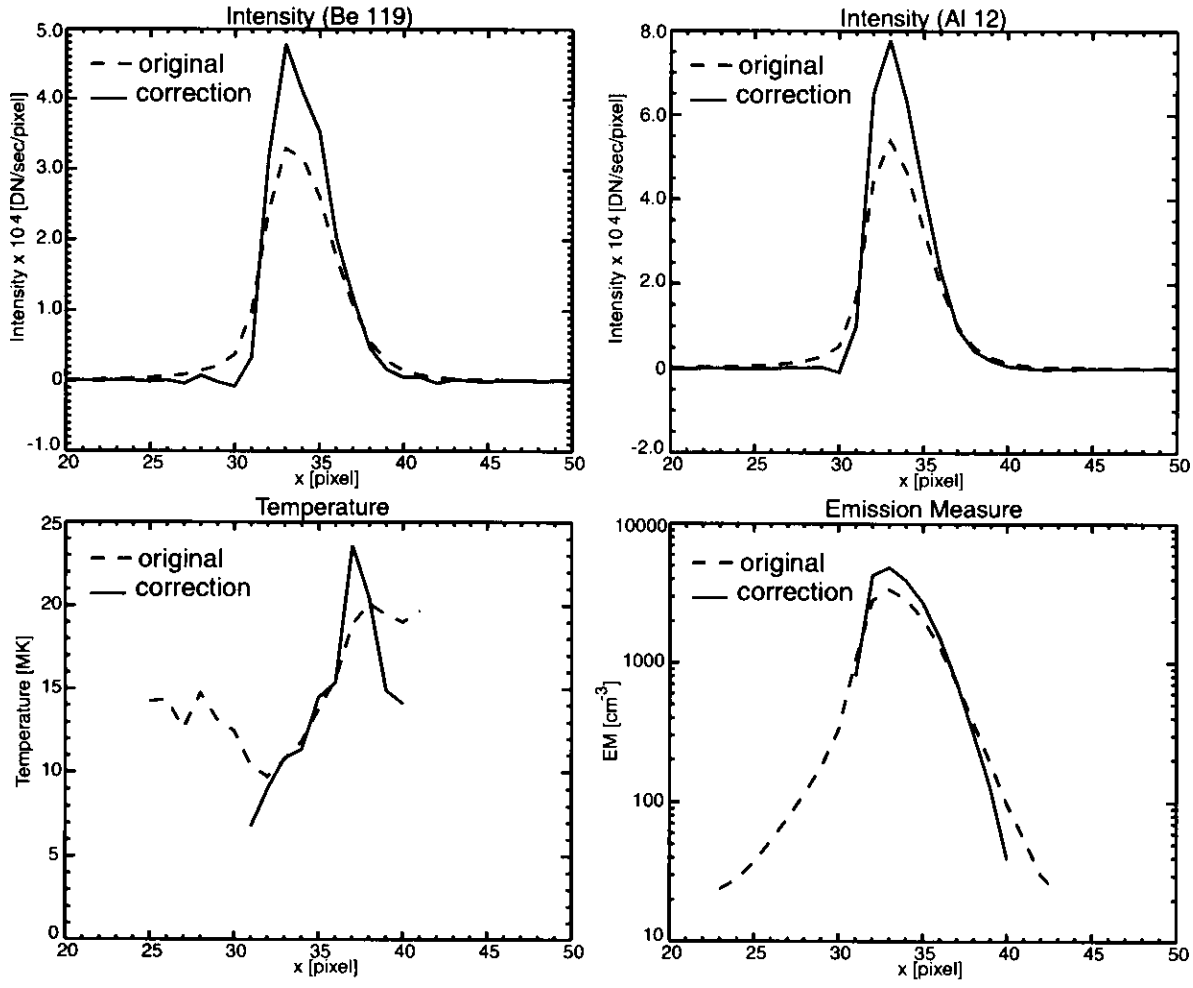

Figure 2.12: Intensity, temperature, and EM line profiles along white lines in the middle row panels of Fig.2.13. Dashed lines and solid lines show original data and converted data using by SXT_PSF procedure, respectively.

2.3.3 Evaluation of Corrected Temperature Maps

Fig.2.12 show intensity, temperature, and emission measure profiles along the white line (a) in the middle row of fig.2.13. Dashed lines and solid lines show original data and converted data using by SXT_PSF procedure, respectively. We can see from the temperature profile in the left- bottom panel that faint scattered-light-affected temperature profiles are eliminated in the corrected image. On the contary, the temperature hump right side of the intensity peak was not affected, and hence, is a real structure. The peak temperature in the corrected image is higher than that in the original image, because scattered photons are put back more to the original position in the Be119 filter image than in the Al112 filter image.

Fig.2.13 shows temperature maps of 13 January 1992 flare at the epochs shown in the figures. Left panels are from the original data and right panels are temperature maps obtained from the correct images. Comparing the left and right panels, one can easily recognize that faint "high-"temperature structures far away from the flare loop are much suppressed in the right panels, and that these high temperature regions can be considered as fake structures.

Fig.2.14 compares time series of temperatures and EMs of the high-temperature region and the flare loops derived from original images and deconvolved images. Crosses ($\times$) and solid line show the parameters (T_e in the left panel and EM in the right panel) for the high-temperature region and the flare loop obtained from the original data, respectively. Diamonds ($\diamond$) and dashed line show those from the deconvolved data. We see from these figures that temperatures obtained from the converted data come to the peak earlier in time, and are higher reaching the maximum difference of about 5 MK. Generally, temperatures and sizes of the high-temperature region detected in the converted images are, first, similar to those already derived from the original images, but higher and more compact than those parameters from the original data. On the other hand, shapes and time profiles of the flare loops themselves show no big changes.

As the conclusion, accurate temperatures can be derived from the converted data, while shape of real faint structures could be even extracted from the original data, which sometimes have wider field of view in lower spatial resolution.

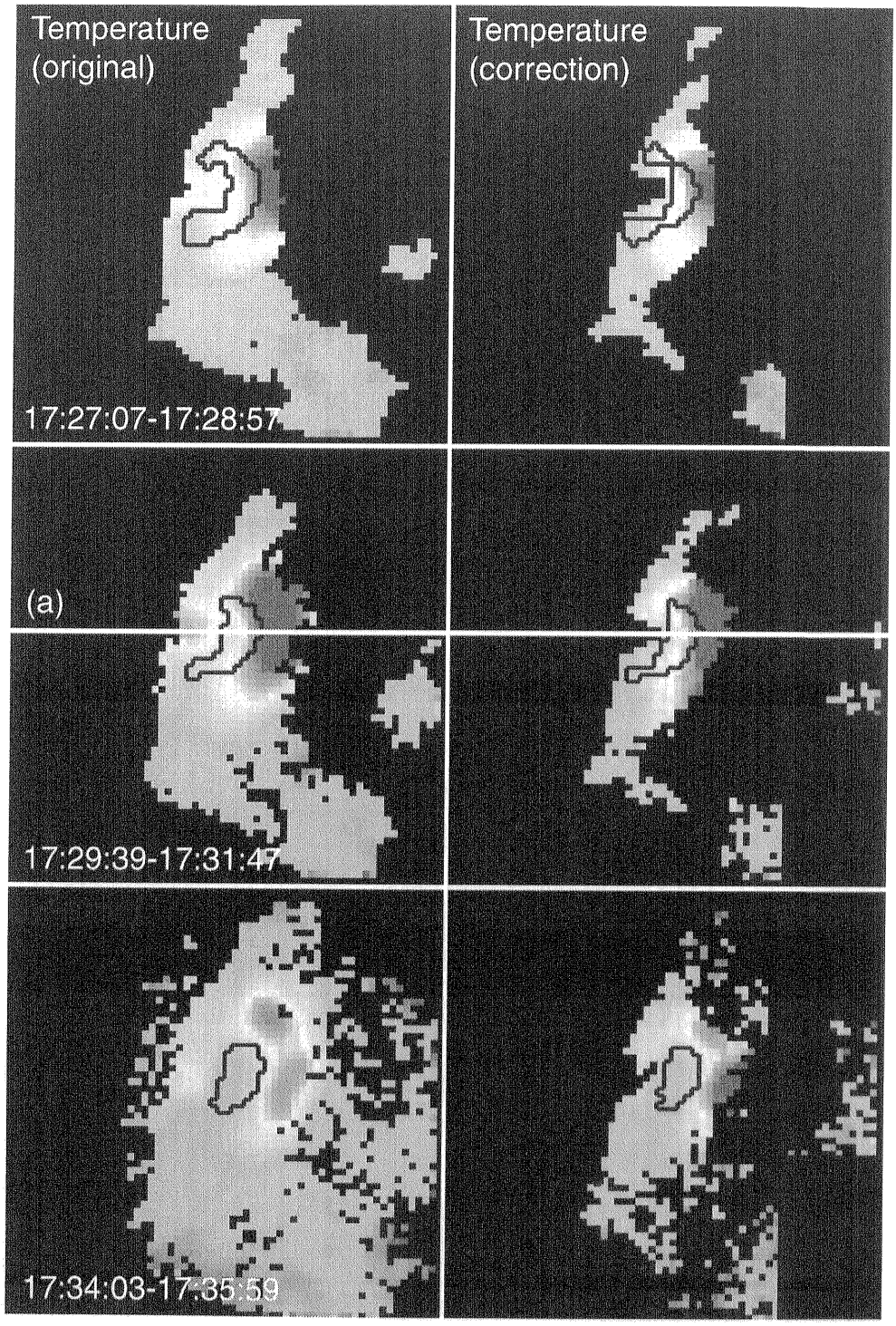

Figure 2.13: Temperature maps of 13 January 1992 flare. Left and right panels show maps obtained from original data and converted data, respectively.

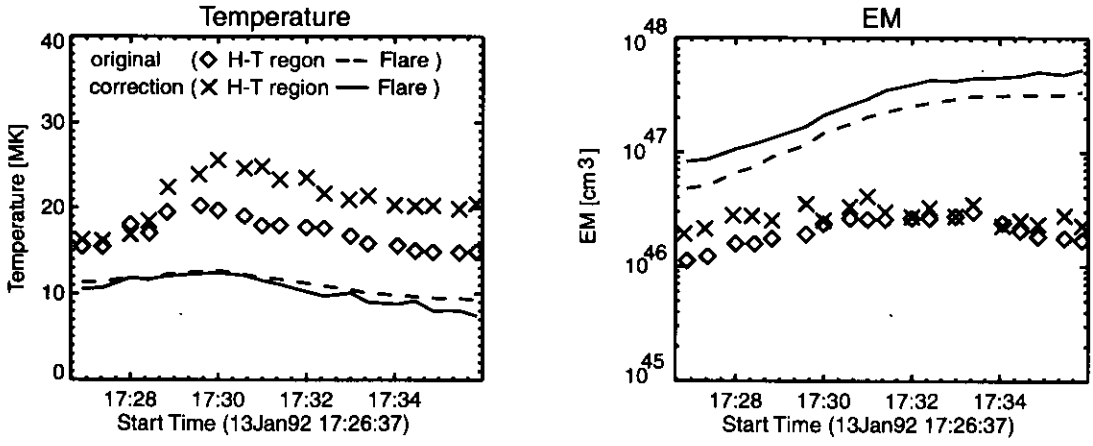

Figure 2.14: Time profile of temperature and EM of the high-temperature region and flare loop. A cross ($\times$) symbol and solid line show the high-temperature region and the flare loop obtained from original data. A diamond ($\diamond$) symbol and dashed line show the high-temperature region and the flare loop obtained from converted data.

References

Hudson, H. 2000, in *the Calibrations Notes*

Hara, H. 1992, Master thesis, Department of Astronomy, The University of Tokyo.

Hara, H., Tsuneta, S., Lemen, J. R., Acton, L. W., & McTiernan, J. M. 1992, PASJ, 44, L135

Hara, H., Tsuneta, S., Acton, L. W., Bruner, M. E., Lemen, J. R., & Ogawara, Y. 1994, PASJ, 46, 493

Kano, R., & Tsuneta, S. ApJ, 454, 934

Martens, P. C., Acton, L. W., & Lemen, L. W. 1995, Sol. Phys., 157, 141

Ogawara, Y., Takano, T., Kosugi, T., Tsuneta, S., Watanabe, T., Kondo, I. & Uchida, Y. 1991, Sol. Phys., 136, 1.

Siarkowski, M., Sylwester, J., Jakimiec, J., & Tomczak, M. 1996, *ACTA ASTRONOMICA*, 46, 15

Shin, J. 1998, PhD Thesis., The Draduate University for Advanced Studies

Tsuneta, S., Acton, L.,Bruner, M., Lemen, J., Brown, W., Caravalho, R., Catura, R., Freeland, S., Jurcevich, B., Morrison, M., Ogawara, Y., Hirayama, T., & Owens, J., 1991, Sol. Phys., 136, 37.

Tsuneta, S., Masuda, S., Kosugi, T., & Sato, J. 1997, ApJ, 478, 787

Vaiana, G. S., Van Speybroek, L., Zombeck, M. V., Krieger, A. S., Silk, J. K., & Timothy, A. 1977, *Space Sci. Instr.*, 3, 19

Chapter 3

Characteristics of the High-Temperature Region above the Loop Top

Abstract

We have found 64 flares associated with high-temperature regions observed with Soft X-ray Telescope (SXT) aboard *Yohkoh* out of 141 flares which Sato et al (1998) compiled from Hard X-ray Telescope (HXT) during the period from 1991 October through 1998 August. A statistical study for these high-temperature regions results in the following characteristics: (1) The average of temperature is 19 MK. (2) The average volume emission measure is $10^{48.6}$ cm^{-3}. (3) The average of area is 1.5×10^9 km^2. (4) Temperature and area of the high-temperature region are proportional to those of the flare loop. (5) High-temperature regions begin to appear during the hard X-ray impulsive phase and reach a maximum temperature before the peak of soft X-ray intensity. (6) The rise velocity of the high-temperature regions is $2 \sim 3$ times as fast as that of the flare loops. (7) Flares associated with the high-temperature region have stronger X-ray fluxes, longer life times, and bigger areas than those without high-temperature regions.

3.1 Introduction

The soft X-ray telescope (SXT) (Tsuneta et al., 1991) and the hard X-ray telescope (HXT) (Kosugi et al., 1991) aboard *Yohkoh* (Ogawara et al., 1991) have made epoch-making observations for the study of solar flares. Solar flares have been usually classified into two types, i.e., compact or impulsive flares and long duration event (LDE) flares represented by the CSHKP flare model (Petschek, 1964; Carmichael, 1964; Sturrock, 1966; Hirayama, 1974; Kopp & Pneuman, 1976), each of which was thought to require different physical mechanisms (Priest, 1981). Several scientists argued that magnetic reconnection is responsible for the LDE flares, though no common opinion appeared for the mechanism of the impulsive flares. Masuda et al. (1994) discovered a hard X-ray source above a soft X-ray loop, which suggested that the reconnection process might take place in impulsive flares as well as in the LDE flares. According to Masuda et al. (1994), the loop-top hard X-ray sources had effective temperatures of 100–150 MK and the total emission measures (EM) of 10^{44} cm^{-3}, if the hard X-ray source was a thermal (superhot) source. Moreover the areas above the flare loop showed higher temperatures than other regions in the main loops. The temperatures and the total EMs in these areas were about 30 MK and 10^{47-48} cm^{-3}, respectively. Tsuneta et al. (1997) investigated the high temperature region of this 13 January 1992 flare and reported the following characteristics. (1) The temperature of the hot source (15–20 MK) was 1.5 times as high as the that of flare loop (9–12 MK). (2) The total EM of the hot source (2×10^{48} cm^{-3}) was 1 order of magnitude less than that of flare loop (10^{49} cm^{-3}). (3) The single high-temperature region appeared before the soft X-ray peak and gradually parted to two high-temperature sources in the peak and decay phases. From these observations he suggested that the high-temperature region was heated by the slow shock associated with magnetic reconnection. Similar high-temperature regions above the flare loops were observed in 16 events out of 33 flares with the SXT and the Bragg Crystal Spectrometer (BCS) (Culhane et al., 1991) aboard the *Yohkoh* (Doschek, 1999). Warren et al. (1999) reported hot plasma (15–20 MK) at the top of an arcade by comparing the *Transition Region and Coronal Explorer* (*TRACE*) and SXT images.

So far, the physics of the high-temperature regions was not well understood. First, it was difficult to make accurate temperature maps for faint structures in SXT images. Second, a statistical approach for the high-temperature region was not thoroughly done with discussion of their physical parameters and relationship to the soft X-ray loop. Therefore, in this paper we would like to examine the characteristics of high-temperature regions above flare loops, taking the accuracy of the temperature map into account. We ob-

tain the physical parameters of the high-temperature region and discuss the relationships between the high-temperature region and other parts of the flare.

3.2 Observation and Analysis

3.2.1 Data selection

The observations were made with the soft X-ray telescope (Tsuneta et al., 1991) aboard *Yohkoh* (Ogawara et al., 1991). Only partial-frame images (PFIs) in the Flare mode were used, which were taken in high temporal and spatial resolutions. For this study, flares are selected from THE YOHKOH HXT IMAGE CATALOGUE edited by Sato et al (1998) and satisfying the following conditions.

- Flares are observed by both the Al 11.6 filter and the Be 119 filters, which are the most temperature-sensitive filter combination for flaring plasma.
- The number of full-resolution PFI images obtained from two filters is more than 30, in order to examine the temporal evolution of the high-temperature region.
- Near-limb flares located at the heliocentric longitudes exceeding $\pm$ 60 degrees are chosen, in order to study the vertical structures above the soft X-ray loops, as shown (Fig.3.1). The latitude range is also restricted to less than 60 degrees both north and south, as it is where we generally find active regions.

The total of 141 flares are chosen by the above-mentioned criteria from 1 October 1991 to 31 August 1998.

3.2.2 Temperature Map

The temperature maps are obtained from the ratios of two images taken with two different filters the assumption that an isothermal plasma occupies each single SXT pixel. In this paper we use the Al 11.6 and the Bel19 filter images. Generally speaking, the temperatures obtained from the SXT images are less reliable in the pixels with low levels of intensity. The following improvements are accommodated to reduce the inaccuracy: We use only the pixels in the images with intensities greater than 1/50 of the maximum intensity and with Poisson noise error less than 10 %. Successive images, usually taken in 2 minute intervals are coaligned and summed to improve the photon statistics. Only scattered light structures from the central part of PSF are considered in the analysis,

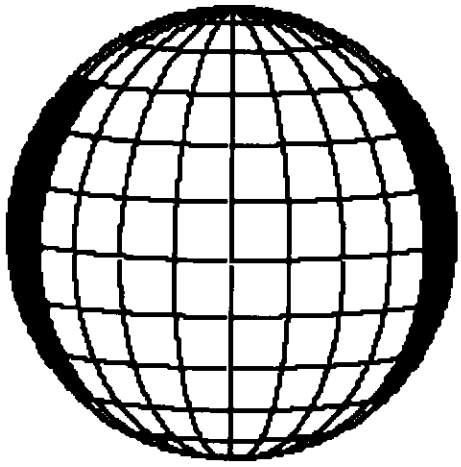

Figure 3.1: The schematic picture of the area of the selected flares. The gray areas are at the heliocentric longitudes exceeding 60 degrees from the disk center.

applying the PSF calculated from SXT_PSF of *Yohkoh* studied software. The uncertainty in the derived temperatures is discussed in section 2.

3.2.3 Definition of High-Temperature Regions

The high-temperature regions are defined as the area which satisfy the following criteria.

- The temperature of the region should be more than 1.5 times higher than the average temperature of the main flare loop. In this paper, the flare loop is defined as the area where the emission measure in each pixel is more than 30 % of the peak emission measure.
- The region should have more than two contiguous pixels, which have temperatures satisfying the first criterion.
- The region should be continuously observed in more than three maps.

To find high-temperature regions, we made the movie of temperature maps which consisted of running-mean difference images integrated for about 2 minutes. The average time interval for each map is about 30 sec. We found 64 flares with high-temperature regions above the flare loop tops.

Next, the area of the high-temperature regions is defined as the area where the temperatures are more than 80 % of the maximum temperature in the selected region. The 64 events to be analyzed are summarized in table 3.1.

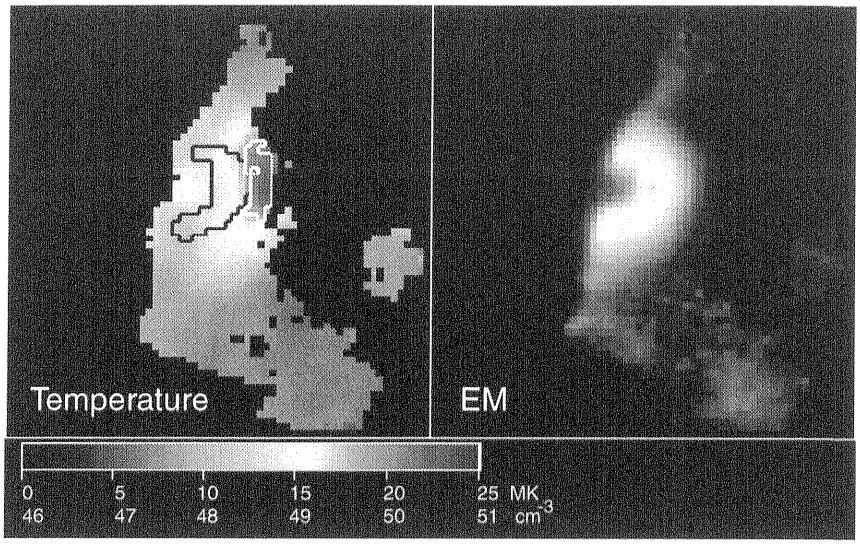

Figure 3.2: High-temperature region and flare loop of the 13 January 1992 flare. Left panel shows the temperature map obtained from soft X-ray images of the Al 11.6 filter and the Be119 filter. High-temperature region (shown by white line) is defined as the region where the pixel temperature is more than 80 % of the maximum temperature in the map. Similarly the flare region (shown by black line) is defined as the area where EM is more than 30 % of the maximum EM in the right map. The right panel shows the emission measure map.

Fig. 3.2 shows both the high-temperature region and the flare loop region in the 13 January 1992 flare. Left and right panels are the temperature and EM maps, respectively. The black line in the left panel corresponds to the flare loop region, namely the EM of this area is more than 30 % of the maximum EM among the pixels in the right panel. In the same way, the white line is the boundary line of the high-temperature region. The temperature inside the white line is more than 80 % of the maximum temperature among the pixels in the left panel.

Table 3.1: List of Flares and High-Temperature Regions

	General Infomation						Parameters of Flare Region					Parameters of H-T Region					
event	Date	Start	End	Lifetime	GOES	Location	T	VEM $\times 10^{48}$	Area $\times 10^{8}$	Density $\times 10^{10}$	Velocity	T	VEM $\times 10^{48}$	Area $\times 10^{8}$	Density $\times 10^{10}$	Velocity	Height
no.	YYMMDD	HHMMSS		[s]			[MK]	[cm^{-3}]	[km^2]	[cm^{-3}]	[km s^{-1}]	[MK]	[cm^{-3}]	[km^2]	[cm^{-3}]	[km s^{-1}]	[km]
00700	911102	064300	071400	1020	M9.0	S12W60	12	451	36	4.57	16	22	9.6	27	0.85	28	31333
00950	911117	070205	071125	860	M1.1	S11E86	11	87	80	1.10	2	16	1.1	40	0.21	11	21240
00980	911119	092731	093155	780	C8.5	S12W60	10	66	35	1.80	13	16	1.3	12	0.55	18	15329
01060	911202	044857	053211	2250	M3.6	N16E87	9	190	21	4.44	2	20	4.1	14	0.94	12	16815
01750	911218	101736	103342	556	M3.5	S14E84	11	27	8	3.47	9	23	1.9	8	0.92	36	19913
02260	920113	172435	173843	1292	M2.0	S16W84	13	79	33	2.09	4	20	8.9	26	0.84	8	19028
02270	920113	190156	191619	867	M1.3	S10E84	11	40	22	1.97	0	18	0.5	7	0.54	3	7080
02290	920114	192321	193811	1376	M1.7	S08E84	9	140	31	2.84	10	17	1.6	15	0.54	24	19470
02360	920126	152317	154211	1420	X1.0	S16W66	10	82	36	2.00	8	19	21	46	0.81	28	11063
02500	920130	170656	170920	856	M1.6	S13E84	9	80	22	2.78	3	18	11	50	0.81	5	22125
02810	920206	001747	002137	2464	C9.9	N14E84	10	20	6	4.20	5	19	2.0	21	0.47	27	19028
02820	920206	031203	034327	1620	M7.6	N05W82	12	316	50	3.00	4	30	0.8	66	0.13	7	5664
02860	920206	205053	212103	2647	M4.1	N06W84	14	53	21	2.43	1	30	0.2	5	0.37	17	4868
02970	920213	073300	073440	708	C5.5	N21W62	11	8.3	10	1.75	7	14	1.2	15	0.46	15	6638
03240	920219	033539	040205	828	M3.7	N04E85	10	51	39	1.47	3	16	1.1	8	0.78	11	41484
03270	920219	144331	145629	–	C9.4	N06E84	13	15	24	1.13	0	16	1.6	17	0.66	16	7965
03280	920219	153333	153847	2190	M1.2	N04E70	9	68	63	1.18	3	14	2.6	21	0.52	7	8850
03380	920226	013508	014004	790	M1.3	S16W90	11	28	12	2.76	5	16	6.4	25	0.81	25	3825
03680	920419	020956	021254	1296	C3.9	N15E78	9	37	52	1.01	6	14	5.0	34	0.50	12	16373
04820	920811	222441	223343	661	M1.4	N14E82	11	22	8	3.47	7	23	1.2	10	0.61	46	15045
05010	920822	082249	082429	540	C1.9	N13W62	8	25	67	0.67	–	12	7.8	77	0.34	–	–
05090	920825	190112	191624	2069	C8.7	N16W84	10	114	87	1.20	5	14	5.6	27	0.63	10	23674
05400	920909	020618	021950	1110	M3.1	S10W72	11	164	20	4.45	4	16	3.2	21	0.58	25	10620
05430	920909	175739	180045	1350	M1.9	S11W78	10	83	18	3.44	11	17	1.8	15	0.55	15	5310
05590	921005	092342	094032	1032	M2.0	S08W84	10	105	12	5.03	8	18	4.7	25	0.63	13	11948
05690	921011	020224	020558	2646	C8.3	S12W60	9	74	32	2.08	10	13	7.5	40	0.56	20	16373
05920	921027	221655	222023	486	C5.4	N08W84	9	9.7	8	2.28	12	13	4.2	19	0.71	35	11948
06280	921105	202845	204059	1338	C8.2	S18W84	9	8.3	8	2.13	3	13	2.7	28	0.44	25	15488
06380	921122	230638	231222	243	M1.6	N11E76	12	83	15	3.79	0	19	4.7	18	0.79	14	9293
06590	921204	113700	114210	–	M1.4	N19W71	11	36	17	3.14	14	17	3.2	25	2.00	29	14160
07160	930216	142612	143130	1124	M2.1	S06W76	9	224	40	3.03	0	13	2.7	20	0.55	6	18806

In the table, T is the electron temperature, VEM is the volume emission measure.

Table 3.2: Table 3.1 (Continue)

event	Date	General Infomation Start	End	Lifetime	GOES	Location	Parameters of Flare Region T	VEM	Area	Density	Velocity	Parameters of H-T Region T	VEM	Area	Density	Velocity	Height
								$\times 10^{48}$	$\times 10^{8}$	$\times 10^{10}$							
no.	YYMMDD	HHMMSS		[s]			[MK]	[cm^{-3}]	[km^2]	[cm^{-3}]	[km s^{-1}]	[MK]	[cm^{-3}]	[km^2]	[cm^{-3}]	[km s^{-1}]	[km]
07190	930217	103336	105436	1279	M5.8	S07W87	10	294	26	4.75	7	22	0.9	11	0.52	8	15488
07220	930221	003049	004945	1219	M1.4	N13E75	10	43	20	3.98	3	21	1.3	8	0.82	23	8850
07590	930315	203147	211353	3891	M2.5	S02W84	9	383	123	1.68	0	15	4.3	85	0.24	5	53100
08160	930611	101406	102040	1339	C5.7	S13W80	10	29	50	0.90	1	19	1.3	16	0.48	2	26550
08210	930624	074331	080537	1219	M9.7	S11E64	9	462	48	3.78	5	17	13	36	0.78	11	42038
08230	930624	172731	173913	1402	M4.2	S12E90	10	144	73	1.67	0	15	117	75	1.36	2	39825
08240	930625	031133	033441	1158	M5.1	S10E84	11	433	46	3.72	7	22	29	45	0.97	10	41064
08480	930926	182843	183013	1184	C2.6	N12E84	9	5.9	20	1.47	4	14	1.4	28	0.37	2	35400
08520	930927	104805	105549	792	C5.7	N11E80	11	208	27	1.22	5	21	1.4	10	0.66	6	16815
08530	930927	120709	121805	549	M1.8	N08E84	9	100	17	3.96	15	15	2.7	18	0.63	26	12390
08570	930928	025821	030917	732	C6.7	N12E73	10	14	15	1.57	19	14	4.5	22	0.66	33	11505
08730	931009	080801	081539	670	M1.1	N11W78	9	34	8	4.27	–	16	3.5	28	0.49	–	84078
08980	931130	060321	060915	–	C9.2	S20E84	10	18	21	1.42	0	14	9.1	50	0.52	5	22125
09390	940116	230821	232311	1034	M6.1	N08E74	18	260	35	3.62	12	36	0.8	5	0.97	10	11063
09610	940128	164852	170832	5175	M1.8	N08W85	10	318	90	1.94	2	14	12	73	0.44	4	63720
09630	940128	184646	185228	4012	M1.1	N08W84	9	83	36	1.97	6	12	3.0	19	0.60	12	27140
09660	940129	112002	113446	791	M2.4	N08W84	12	199	72	1.90	0	18	5.9	20	0.84	22	7080
09700	940227	090319	092521	2497	M2.8	N08W84	9	297	53	2.77	8	17	2.4	20	0.54	10	28615
10680	970917	174814	180406	542	M1.0	N20W84	8	60	18	2.93	3	14	0.4	7	0.50	14	16815
10980	971106	115112	121300	368	X9.4	S16W62	20	931	12	17.1	10	33	155	32	2.93	22	14603
11030	971115	223734	224510	1147	M1.0	N20E64	10	119	59	1.64	6	14	30	80	0.66	10	37613
11120	971126	041536	041822	2469	C3.6	N20E84	9	4.7	4	1.00	0	18	2.8	18	0.61	23	15045
11510	980323	024343	032105	2468	M2.3	S20W84	10	135	41	2.27	3	18	5.3	22	0.75	9	39825
11650	980423	052918	071205	1928	X1.2	S20E84	22	214	42	2.80	4	42	7.0	19	0.92	23	14160
11660	980424	084520	085746	889	C8.9	S20E84	9	180	90	1.46	7	15	4.5	29	0.55	13	16815
11830	980506	075728	090818	849	X2.7	S14W66	13	160	34	8.99	12	36	3.3	12	0.95	18	12390
11900	980508	015505	030319	1180	M3.1	S16W84	11	145	35	2.71	6	18	19	31	1.00	18	13275
11950	980509	031733	045755	1861	M7.7	S16W84	15	45	16	2.78	0	30	0.3	3	0.41	14	17700
12380	980809	084127	085251	–	M1.0	N14E60	10	54	16	2.90	13	16	7.8	31	0.67	13	14160
12460	980818	081713	083853	745	X2.8	N34E84	20	524	25	6.47	6	45	6.6	7	2.12	16	11063
12470	980818	221301	235037	532	X4.9	N30E84	16	194	34	9.89	7	33	19	23	1.36	32	16815
12500	980819	142345	143925	1780	M3.0	N35E80	12	248	42	3.07	3	24	1.2	10	0.68	7	22125

In the table, T is the electron temperature, VEM is the volume emission measure.

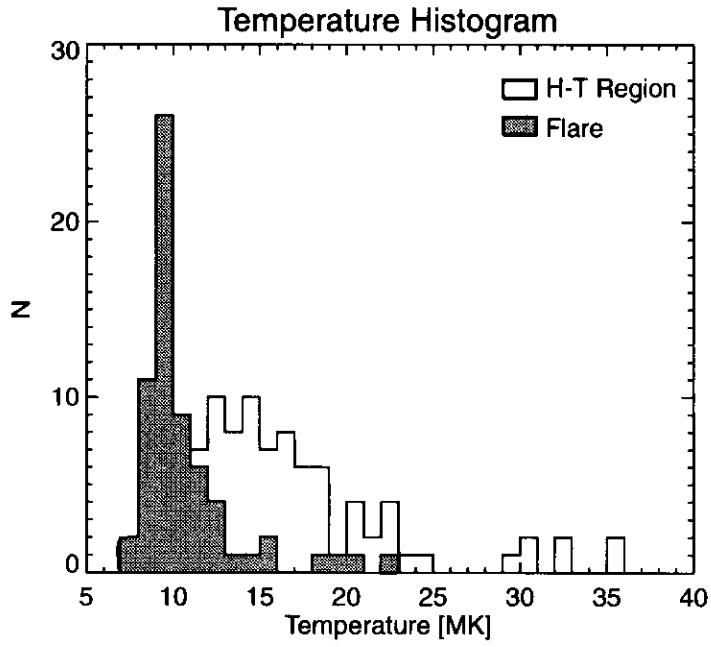

Figure 3.3: Temperatures of the flare loops and the high-temperature regions: The average temperature of the flares and the high-temperature regions are 11 MK and 19 MK, respectively.

3.3 Results

The list of flares with high-temperature regions is shown in table 3.1. The average temperature, the average EM, the average density, the area of the flare and the high-temperature regions were obtained at the nearest time when hard X-ray intensity observed in HXT M1-band was at the peak. Moreover we measured the height of the high-temperature regions at the peak time of HXT M1-band intensity. As for the apparent rising velocity, we recorded the rise velocity of the center-of-gravity of the structure. We defined the flare life time as the time interval, in which soft X-ray intensity is above the half of the maximum intensity.

3.3.1 Physical Parameters

The histogram of temperature and the high-temperature region of the listed flares is shown in Fig. 3.3. The average quantities of the flare loops and the high-temperature regions are 11 MK and 19 MK, respectively. Fig. 3.4 shows the ratio of temperatures between the flare loops and the high-temperature regions. We see from this figure that there is a correlation in the high-temperature regions and the flare loops.

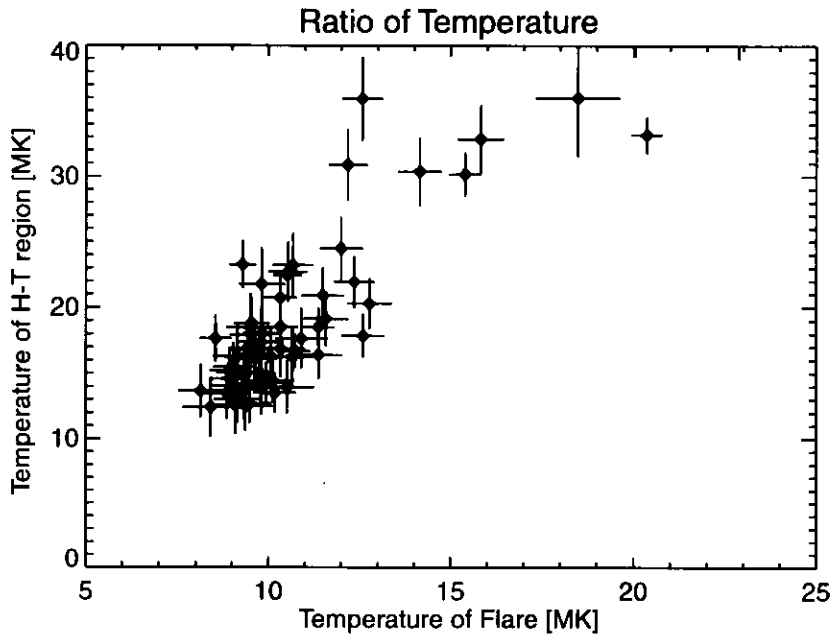

Figure 3.4: The relationship between the temperature of the high-temperature regions and the flare loops.

Fig.3.5 shows the histogram of volume emission measures (VEMs) of the flares and the high-temperature regions. The average VEMs of the flare loops and the high-temperature regions are $10^{49.9}$ cm^{-3} and $10^{48.6}$ cm^{-3}, respectively. The VEM of the flare loop is about one order larger than that of the high-temperature region. Fig.3.6 shows the ratio of VEMs between the flare loops and the high-temperature regions.

The area of the flare loops or the high-temperature regions is defined as the number of pixels in each area. The result is shown in Fig. 3.7. Since one pixel of full resolution image correspond to 1700 km on the solar surface, the average area of the flare loops and the high-temperature regions are 2.0 $\times$ 10^8 km^2 (70.5 pixels) and 1.5 $\times$ 10^8 km^2 (52.9 pixels), respectively. Fig. 3.8 shows the ratio of area between the flare loops and the high-temperature regions. We see from this figure that there is a correlation between the high-temperature regions and the flare loops.

The average quantity of each physical parameter is summarized in Table 3.2.

3.3.2 Relationship between Flare Loops and High-Temperature Regions

In the previous section, we measured the physical parameters of both the flare loops and the high-temperature regions. We investigate in this section the relationship between the

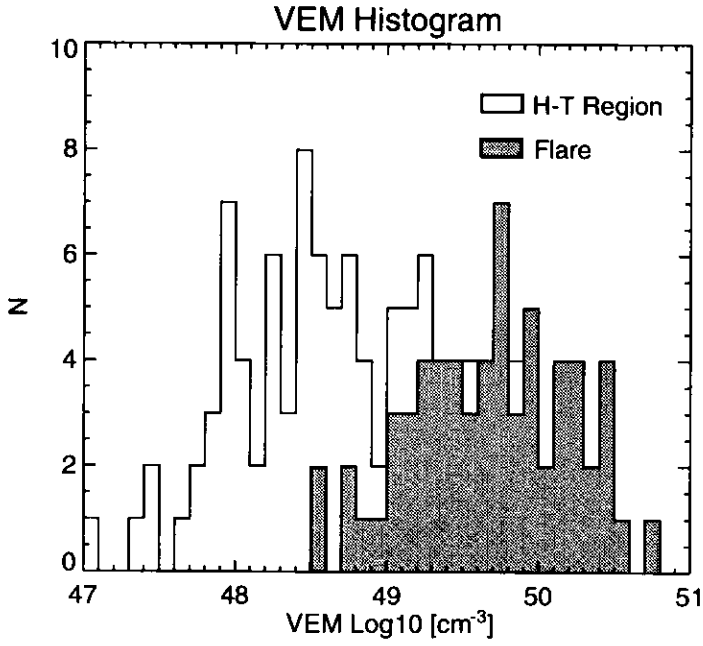

Figure 3.5: Histogram of the volume emission measures (VEMs). The average VEMs of the flare loops and the high-temperatures region are $10^{49.9}$ cm^{-3} and $10^{48.6}$ cm^{-3}, respectively.

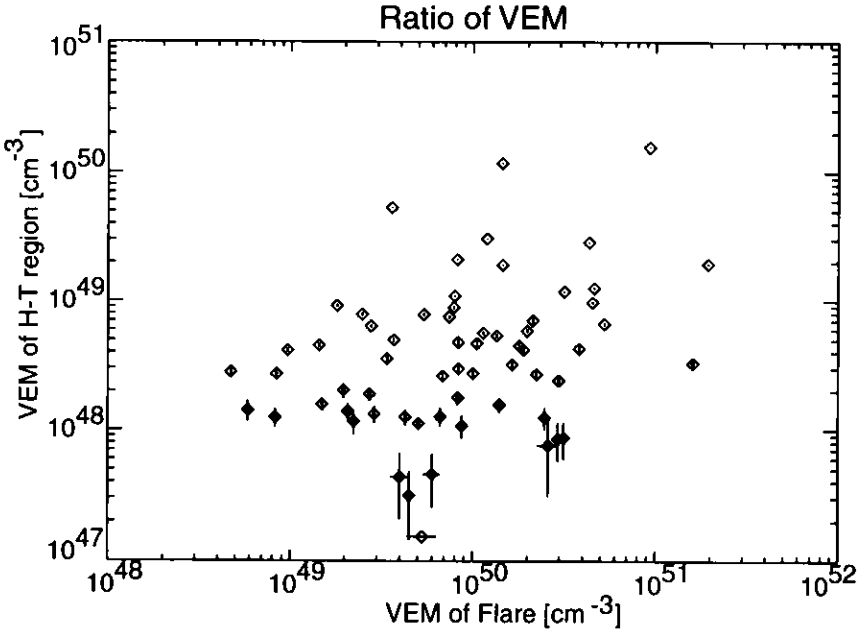

Figure 3.6: The relationship between the volume emission measures of the high-temperature regions and the flare.

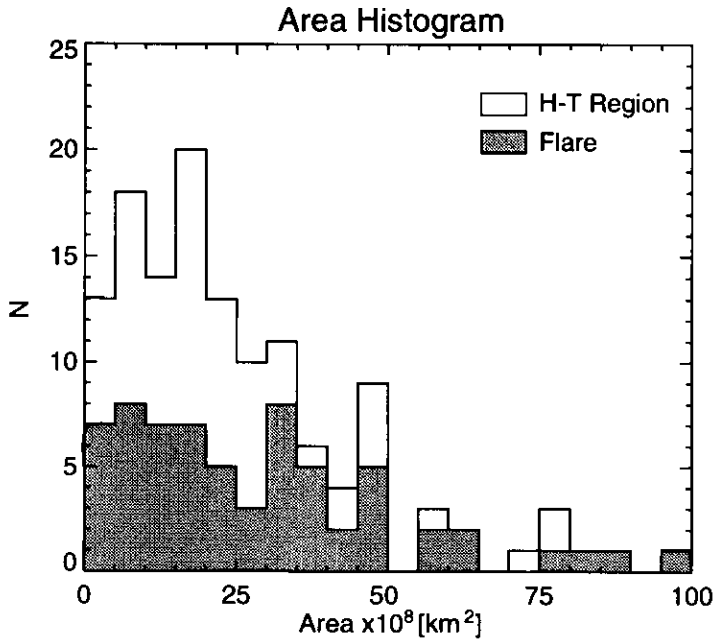

Figure 3.7: Histogram of the areas. The average area of the flare loops and the high-temperature regions are 2.0 $\times$ 10^8 km^2 (70.5 pixels) and 1.5 $\times$ 10^8 km^2 (52.9 pixels), respectively.

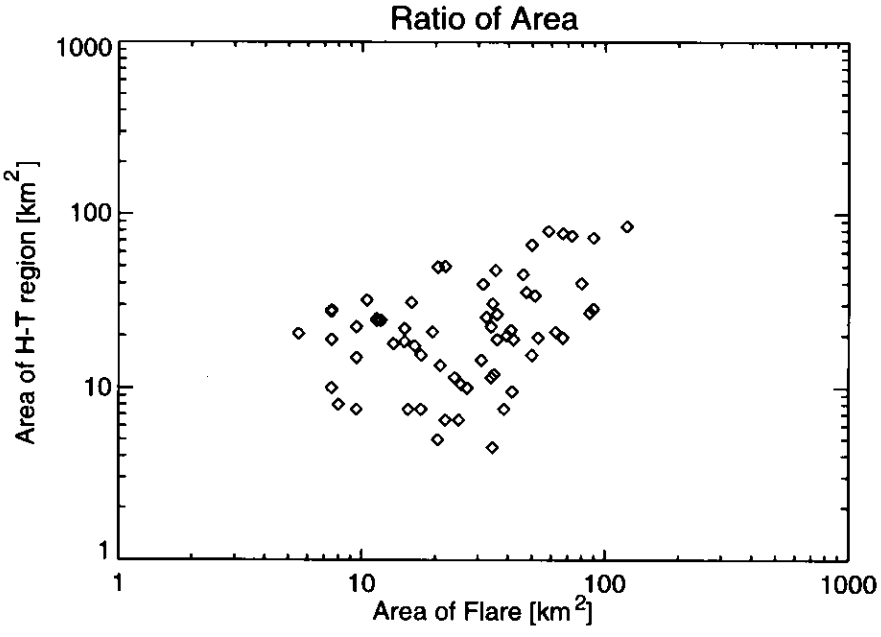

Figure 3.8: The relationship between the area of the high-temperature regions and the flare loops.

Table 3.2: Average Physical Parameters

	Temperature [MK]	VEM [cm^{-3}]	Area [km^2]	Density [cm^3]
Flare	11	$10^{49.9}$	2.0×10^8	3.1×10^{10}
High-temperature region	19	$10^{48.6}$	1.5×10^8	7.3×10^9

flare and the high-temperature region, paying attention to the X-ray fluxes and lifetimes of the flares. The left and right panels of Fig. 3.9 show the relation of the X-ray flux obtained from the GOES satellite and the lifetimes of the flares, respectively. The temperatures of the high-temperature regions are plotted in the first row. In the right panel of the first row, we clearly see that the temperatures of the high-temperature regions are proportional to the X-ray flux of the flares. The second-row panels show them with the VEMs of the high-temperature regions in the abscissa, and the third row panels are the same figures with the areas of high-temperature regions in the abscissa. We can not clearly see a correlation of these parameters for the high-temperature region except in the left panel in the first row.

3.3.3 Time profiles of High-Temperature Regions

Fig. 3.10, Fig. 3.11, and Fig. 3.12 show examples of the temporal and structural variations of the high-temperature regions and the flare loops. The upper figures ((A) $\sim$ (C)) are maps of the flare loop and the high-temperature region at three epochs during the flares. In these figures, intensity images, EM maps, and temperature maps are shown from left to right. Observing times are shown in the intensity images. The high-temperature region and the flare loop region are indicated by white and black lines, respectively. In the lower figures, the upper left panel shows time variation of the X-ray flare intensity obtained from Be 119 filter images of SXT (dot-dashed line) and HXT M1-band (solid line). The other three panels show time variation of the high-temperature region (asterisks) and the flare loop (dashed line) in temperature, emission measure, and area, respectively.

The following common features can be seen in Fig. 3.10, Fig. 3.11, and Fig. 3.12: (1) Both the flare loops and the high-temperature regions rise with time. Especially as Tsuneta et al. (1997) point out, the high-temperature region separates into two high-temperature ridge structures during the peak and decay phases (see Fig. 3.10). The total of 19 out of 64 high-temperature regions show the similar characteristic that the high-temperature region separates into a few patches. (2) The temperatures of the high-

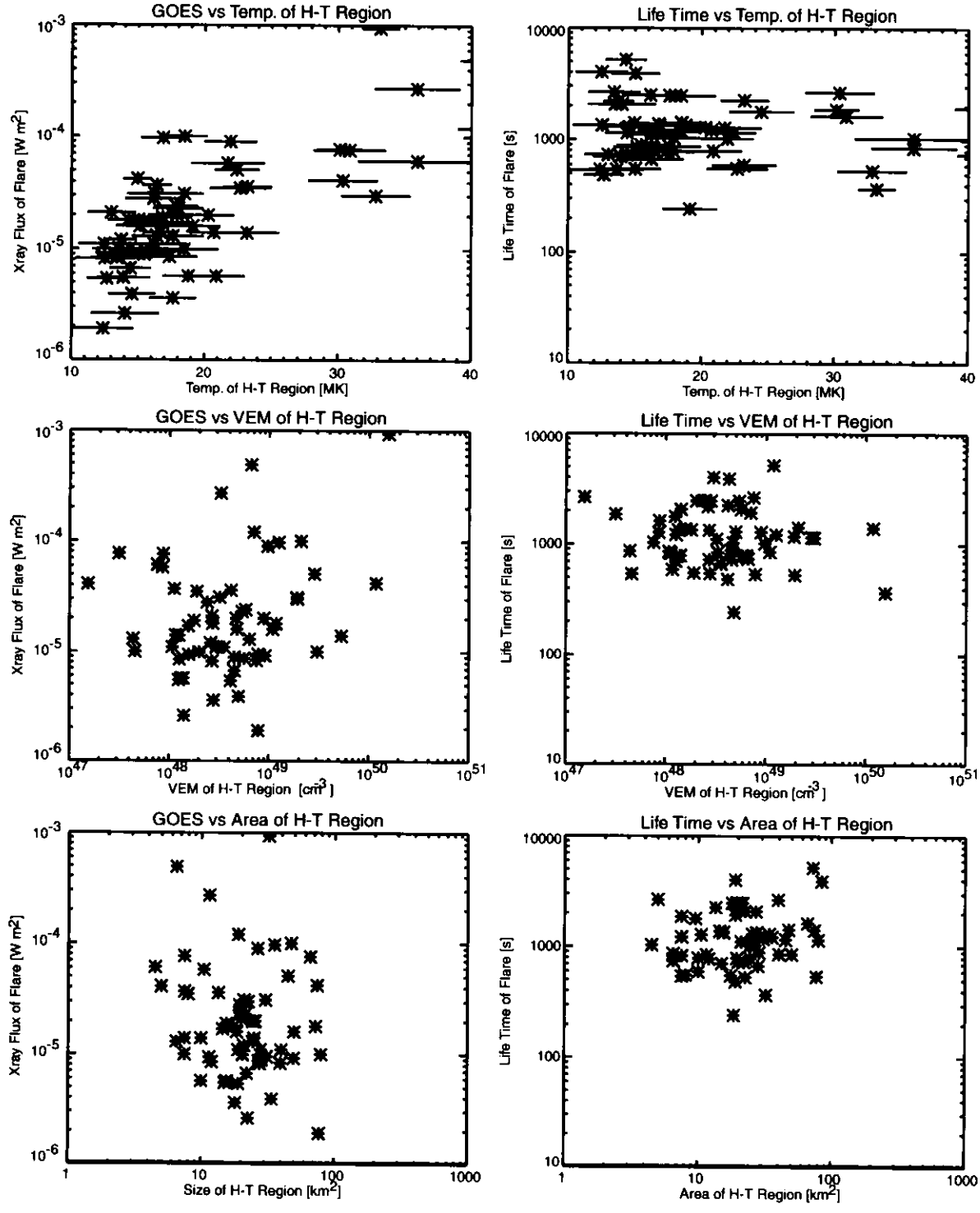

Figure 3.9: Left side panels) X-ray fluxes obtained from the GOES satellite are plotted against temperature, VEMs, and area of high-temperature regions, respectively. Right side) the same figure for flare lifetime vs. temperature, VEMs, and area of high-temperature regions.

temperature regions rapidly increase during the hard X-ray impulsive phase. This can be clearly seen in Fig.3.11, in which we have good coverage of observation preceding to the flare: In the figure (A) taken during the precursor phase, the regions different from the main flare loop is selected as a high-temperature region. In the figure (B), the high-temperature region appears in the north in the temperature map, before the emission measure of the flare loop increase. The time of the figure (B) coincides with the hard X-ray impulsive phase. (3) Temperature of the high-temperature region reaches the maximum between the peaks of hard and soft X-rays. The temperature of the high-temperature region in Fig. 3.12, however, again increases during the decay phase. Similar time profiles are observed for 14 out of 64 high-temperature regions.

3.3.4 Motions of High-Temperature Regions

The flare loops and the high-temperature regions rise at the same time. Fig. 3.13 shows the temporal developments of soft X-ray intensity and temperature map along the solid line in the top right panel for one event. The white line in the top left panel shows the locus of the center-of-gravity of intensity along the solid line. The rise velocity of the flare loop is about 2 km s^{-1}. On the other hand, we can see more rapid motions of the high-temperature regions in the lower figures obtained from the temperature maps. The rise velocity of the high-temperature region is about 10 km s^{-1}. Such a feature is seen in most of the events: The rising velocity of the high-temperature region is higher than that of the flare loop. Fig. 3.14 shows the histogram of the rising velocity of the flare loop and the high-temperature region. The average velocities of the flare loops and the high-temperature regions are 5.7 km s^{-1} and 15.6 km s^{-1}, respectively.

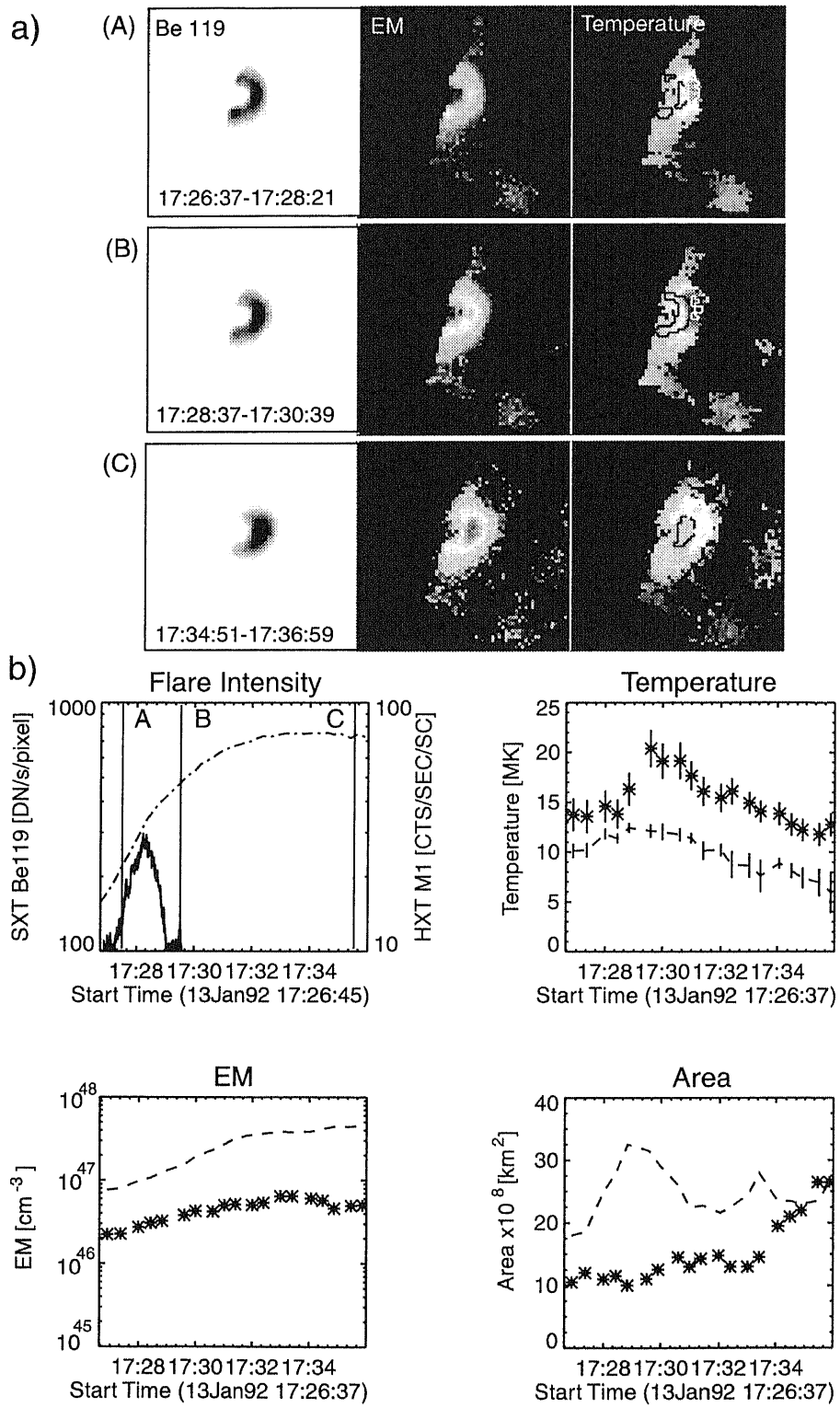

Figure 3.10: Temporal variations of the flare loop and the high-temperature region of the 13 January 1992 flare. Figure (a) shows the intensity, the emission measure, and the temperature maps at the three epochs indicated (A), (B), and (C). In the intensity maps figure (b) shows four time profiles of soft and hard X-ray intensities, temperature, emission measure, and area, respectively.

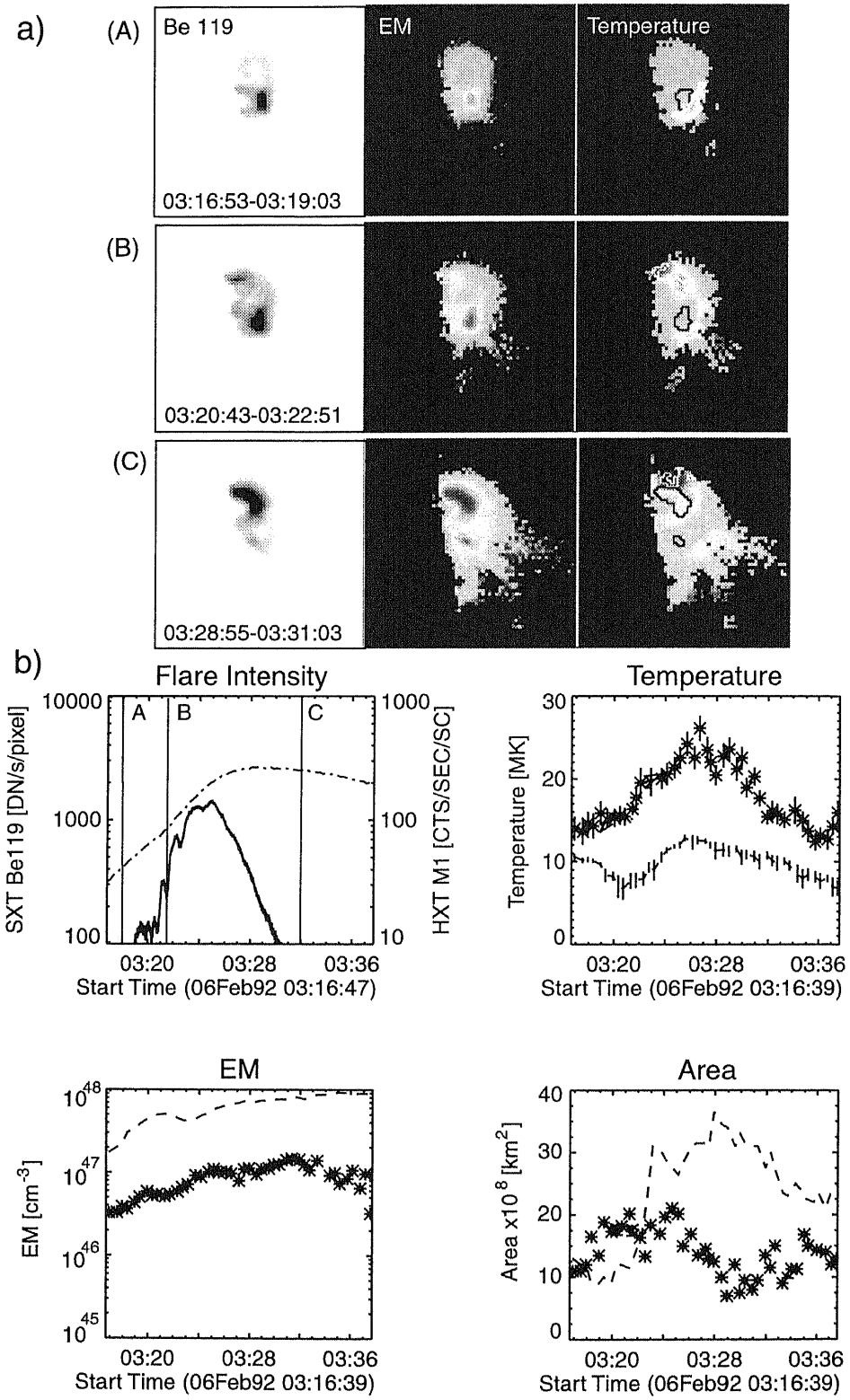

Figure 3.11: The same figure for the 6 February 1992 flare.

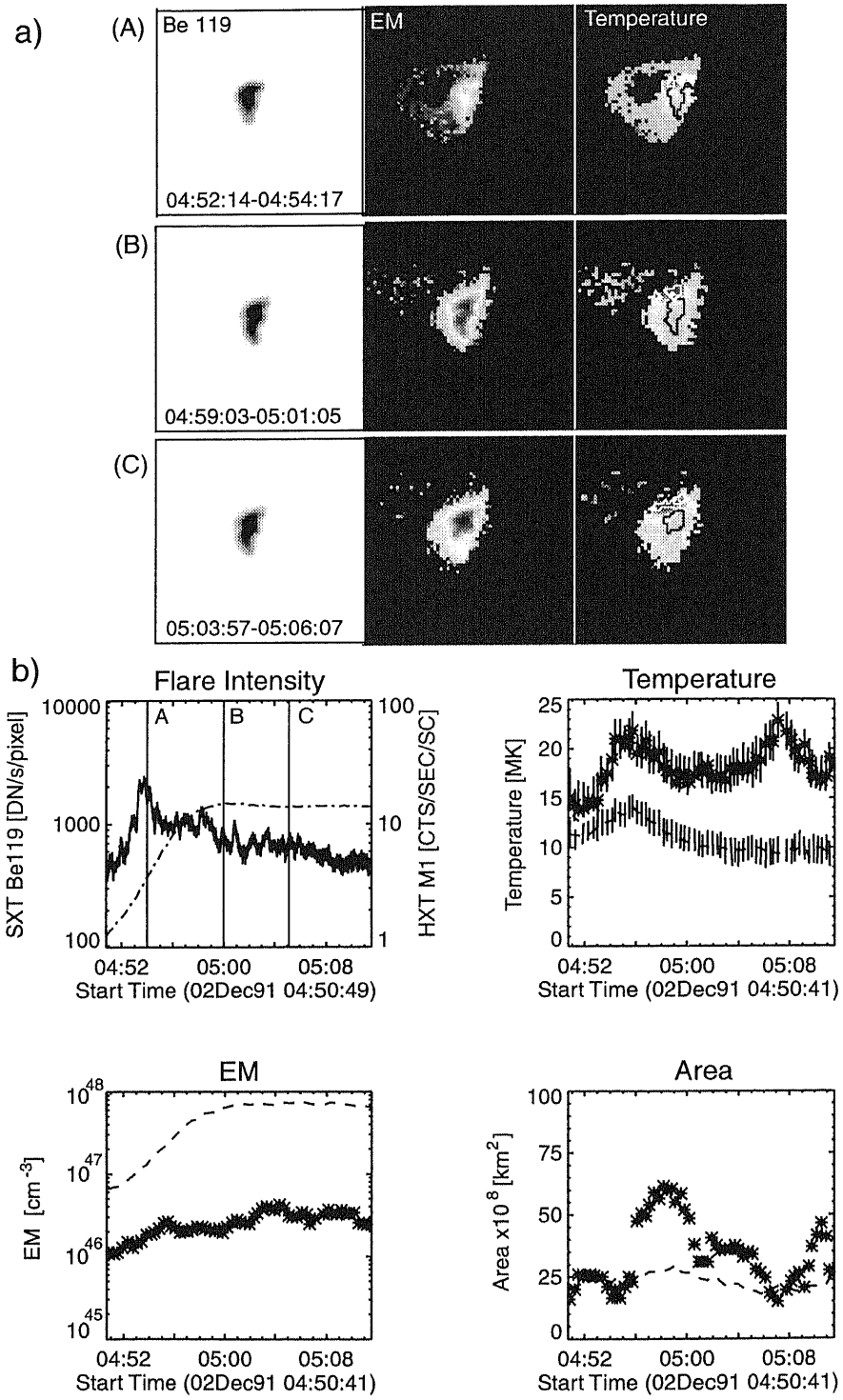

Figure 3.12: The same figure for the 2 December 1991 flare.

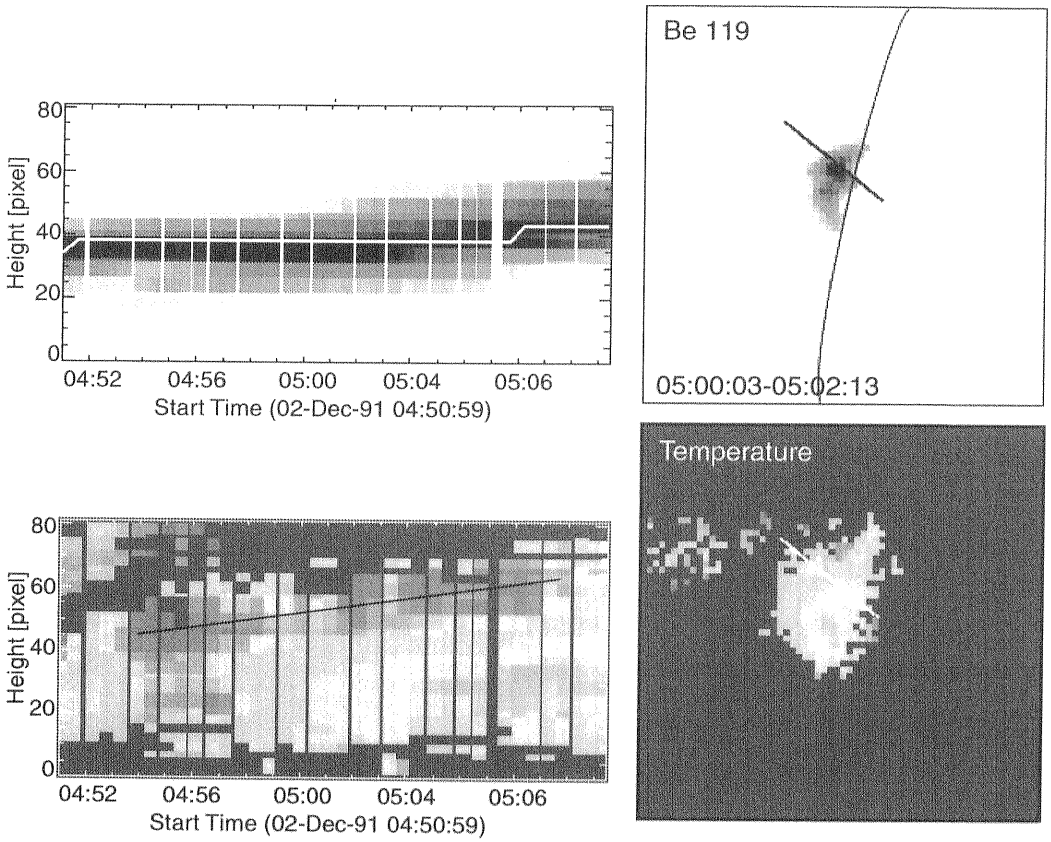

Figure 3.13: Rising motions of the 2 December 1991 flare. The left panels shows time slices of the soft X-ray intensity and temperature along the solid lines in the right panels.

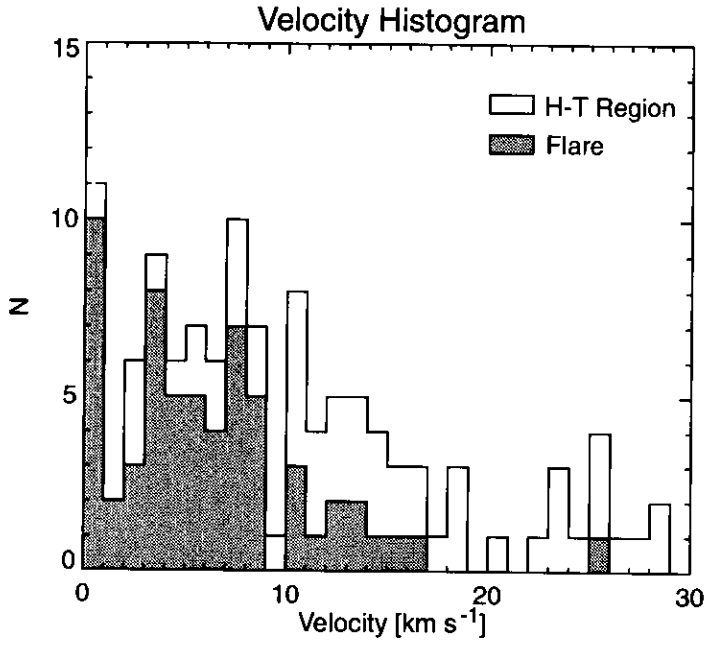

Figure 3.14: Histogram of the rise velocity. The average rise velocity of flare loops and high-temperatures regions are 5.6 km^{-1} and 15.4 km^{-1}, respectively.

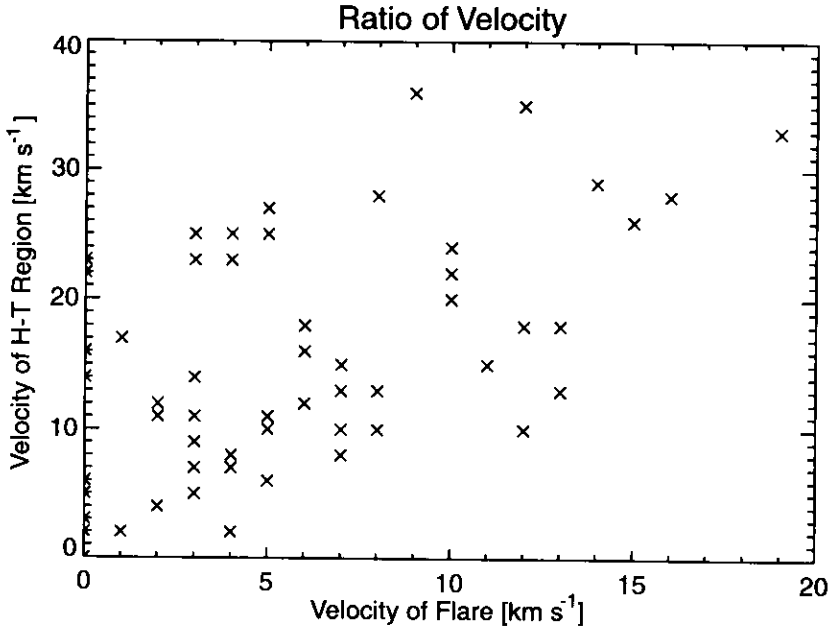

Figure 3.15: Relationship between the rise velocity of high-temperature regions and flare loops.

3.4 Discussion

3.4.1 Heating Mechanism of High-Temperature Regions

We see from Fig. 3.10, Fig. 3.11, and Fig. 3.12 that the high-temperature regions begin to appear during the hard X-ray impulsive phases and reach maximum temperature before the soft X-ray peak times. The temperatures of the high-temperature regions are higher (by definition) and their EMs and densities are much less than those of the flare loops. Since the emission measures of the flare loops result from new coronal material, chromospheric evaporation contributes to the brightening of the thermal flare loops. As the emission measures and densities of the high temperature regions are smaller and they appear earlier during the impulsive phase than the thermal plasmas in the flare loops, it could be guessed that the heating mechanism of the high-temperature region may differ from that of the flare loops, which depend on enthalpy flux brought into the corona by chromospheric evaporation. Many *Yohkoh* observations have led to the scenario that the magnetic reconnection contributes to energy release of flares. Consequently, one possibility is that the heating mechanism of the high-temperature region could be closely related to the magnetic reconnection process. Assuming that the reconnection region is located above the flare loop, we conclude that the high temperature region could be formed by coronal plasma directly heated by the process of magnetic reconnection, prior to evaporation.

Tsuneta et al. (1997) proposed that the heating mechanism of high-temperature region could be the slow shock associated with the reconnection outflow. This suggestion was based on the observation of two high-temperature ridge structures above the flare loop in the 13 January 1992 flare. As there are only a few events that show such clear segments of the high temperature regions in our flare list, we can not strictly confirm his conclusion in our analysis.

3.4.2 Flares without High-Temperature Regions

In our list of flares, no high-temperature regions were observed in about one-half of the case. We discuss in this section the characteristics which discriminate against the appearance of high-temperature regions. In the preceding sections, we found that the temperature of the high-temperature region is correlated to soft X-ray intensity and temperature of the flare loops. As for the geometrical area, the area of the high-temperature region is also correlated to that of the flare loops (Fig. 3.8).

Fig. 3.16 shows the relationships of the X-ray flux and the life time of flares to

each physical parameter of the flare loops; namely, temperature, VEM, and area. The arrangement of the figures is similar to Fig. 3.9. Asterisks (∗) and diamonds (◇) stand for flares associated with the high-temperature regions and flares without them, respectively. First, a glance of a left-side panels of Fig. 3.16 reveals the following. (1) Flares associated with the high-temperature regions have comparatively strong X-ray fluxes. (2) Though the correlation of temperature of the flare loop vs the flare X-ray flux exists in the top figure, this correlation is weaker than that in temperature of the high-temperature regions and the flare X-ray flux shown in Fig. 3.9. (3) There is obviously a correlation in VEM and the flare X-ray flux. Second, by examining the right-side panels in Fig. 3.16, the following can be noted. (4) Flares associated with the high-temperature regions have longer lifetimes. (5) VEMs of the flares associated with the high-temperature regions are comparatively larger than those of the other category. (6) Areas of the flares associated with the high-temperature regions are again comparatively bigger than those of the flares without.

Fig. 3.17 shows the histograms of the flares associated with the high-temperature regions and those of the flares without the high-temperature region vs. GOES X-ray flux, life time, and area of flares. The gray areas are for the flares without the high-temperature regions. It is noted from Fig. 3.17 that flares associated with the high-temperature regions have relatively strong X-ray fluxes, large loop structures in area, and live relatively long. It follows from these that as for flares associated with weaker, smaller, or shorter lifetime, high-temperature regions is not easy to observe due to observational performance. Therefore it is not evident whether flares associated with no high-temperature regions actually have no high-temperature regions. Sakao (1998) reported that two kinds of magnetic field configurations were responsible for the solar flare energy release (see Fig.1.7). With regard to "emerging-flux-type" flares, flare loops is usually compact. The future direction of this topic will be compare "loop-with-a-cusp" type flares and "emerging-flux-type" flares.

3.4.3 Rising Motion of High-Temperature Region

We see from Fig. 3.14 and Fig. 3.15 that rise velocity of many high-temperature regions are higher than those of flare loops. Implications of the difference in speed between the flare loops and and the high temperature region are discussed in this section. According to the CSHKP-type flare model, the rising motion of flare loops is not an actual motion of plasma, but an apparent motion of successive brightenings of reconnected magnetic loops: When reconnected loops, which continuously shrink down to the lower corona, are filled with dense plasma due to chromospheric evaporation, we have the appearance of bright

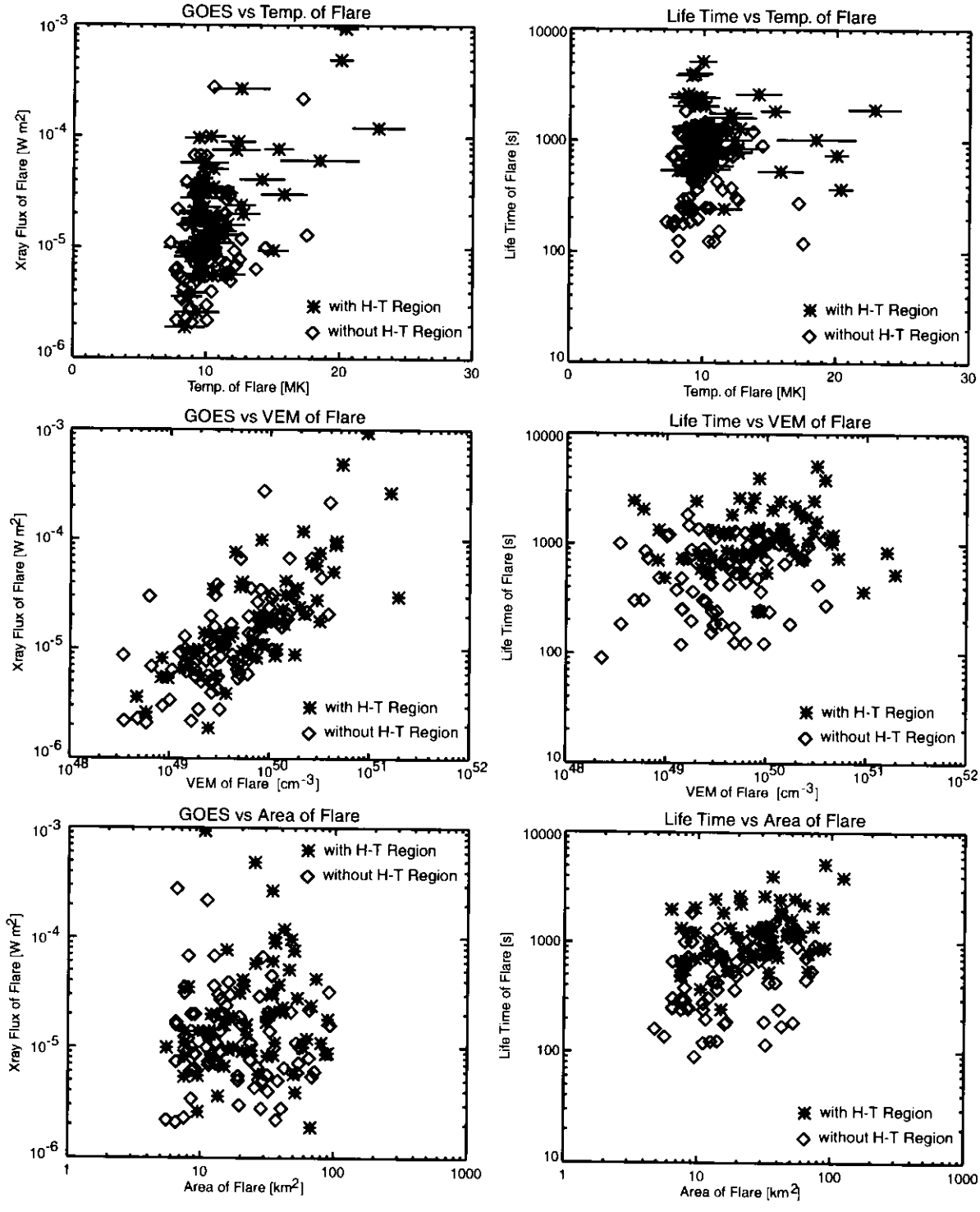

Figure 3.16: Left side) GOES X-ray fluxes are plotted against temperature, VEM, and area of flare loops, respectively from top to bottom. Right side) Same for flare lifetime plotted vs. temperature, VEM, and area of flare loops.

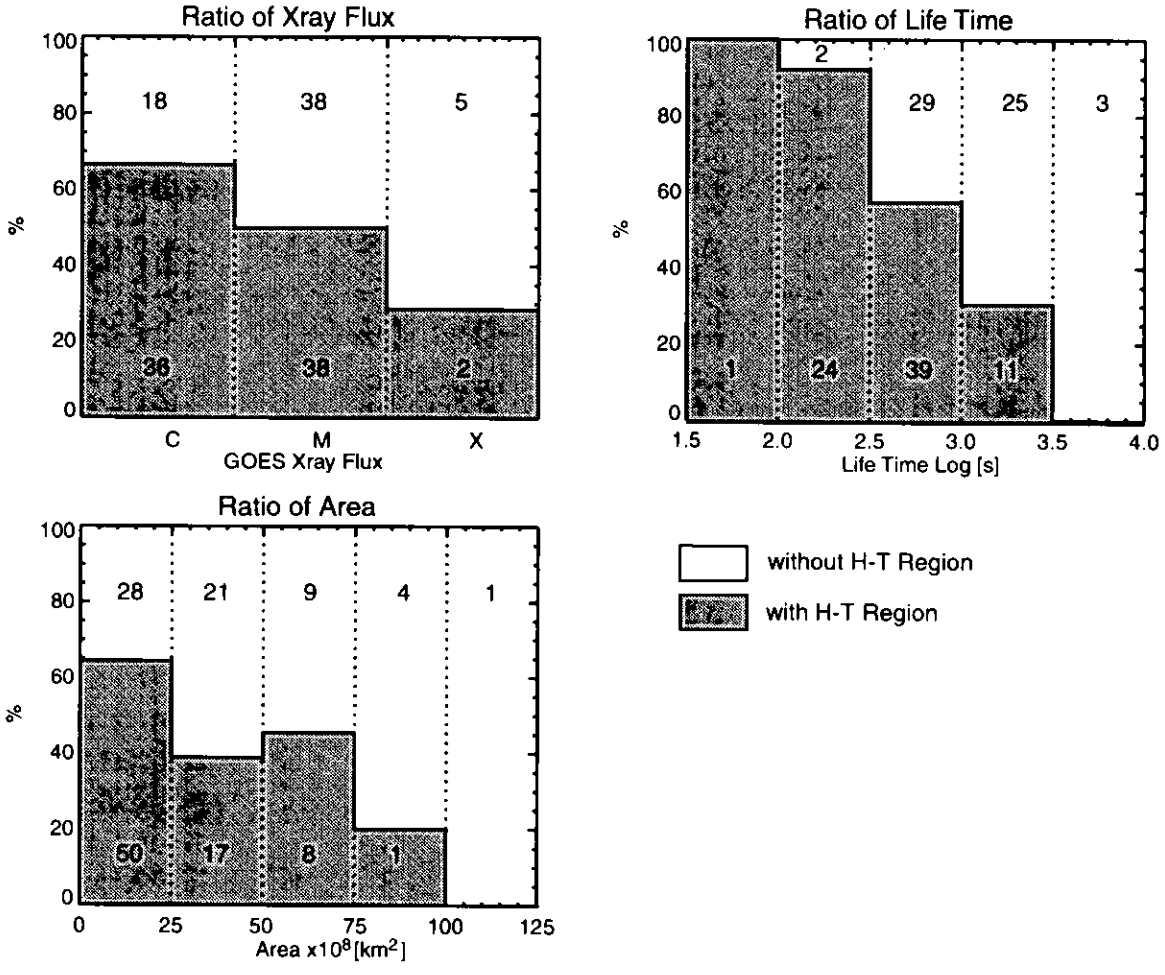

Figure 3.17: Histograms of flares associated with high-temperature regions and without, categorized by GOES X-ray flux, flare lifetime, and area. Flares with high-temperatures regions occupy the white area.

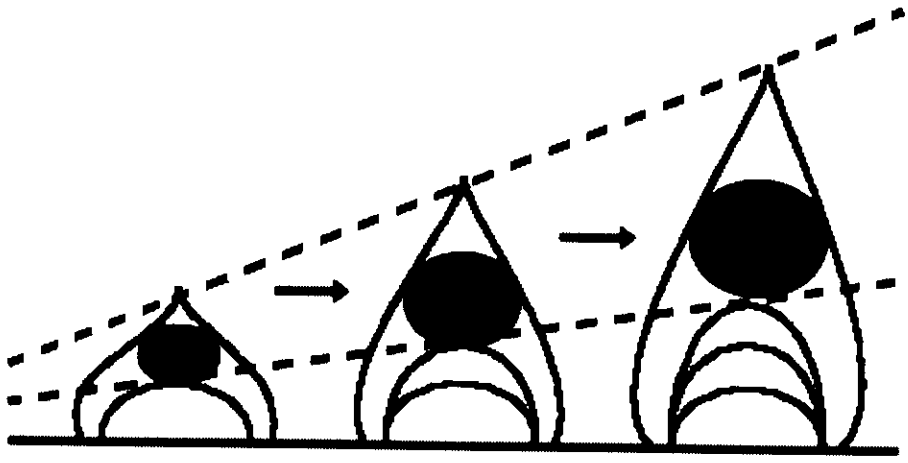

Figure 3.18: Schematic flare loop and cusp structures configuration; assuming that flare loop and cusp structure of flare expand in self-similarity, the rising velocity of the high-temperature regions seem to be faster than that of flare loops.

loops moving upwards in the corona. Since the reconnected loops are piling up one after another in progress of magnetic reconnection. The speed of rising motion of the flare loops is, therefore, related to the reconnection rate. On the other hands, since we think that high-temperature region relate to energy release area, we suppose that high-temperature regions locate between reconnection point and flare loops. Now assuming that flare loop and cusp structure of flare expand in self-similarity, we suppose that the rising motion of high-temperature region relate to a motion of X-point (see Fig. 3.18). Though X-point of reconnection is generally consider as to rise, we did not directly observed the rising motion of X-point. Therefor it is very important to compare the observational rising velocity to the theoretical one.

3.4.4 Scaling Law

Yokoyama & Shibata (1998) and Shibata & Yokoyama (1999) suggested a scaling law for the maximum temperature of reconnection-heated plasma T_{max} and magnetic field strength B,

$$\begin{aligned} T_{max} &\simeq \left(\frac{B^2 v_A L}{\kappa_0 2\pi}\right)^{2/7} \simeq 5.3\times 10^4 B^{6/7} {n_0}^{-1/7} L^{2/7} \\ &\simeq 3\times 10^7 \left(\frac{B}{50G}\right)^{6/7} \left(\frac{n_0}{10^9 cm^{-3}}\right)^{-1/7} \left(\frac{L}{10^9 cm}\right)^{2/7} \end{aligned} \tag{3.1}$$

where $v_A = B/4\pi\rho^{1/2}$ is the Alfven speed, $\rho(= m n_0)$ is the mass density, m is the

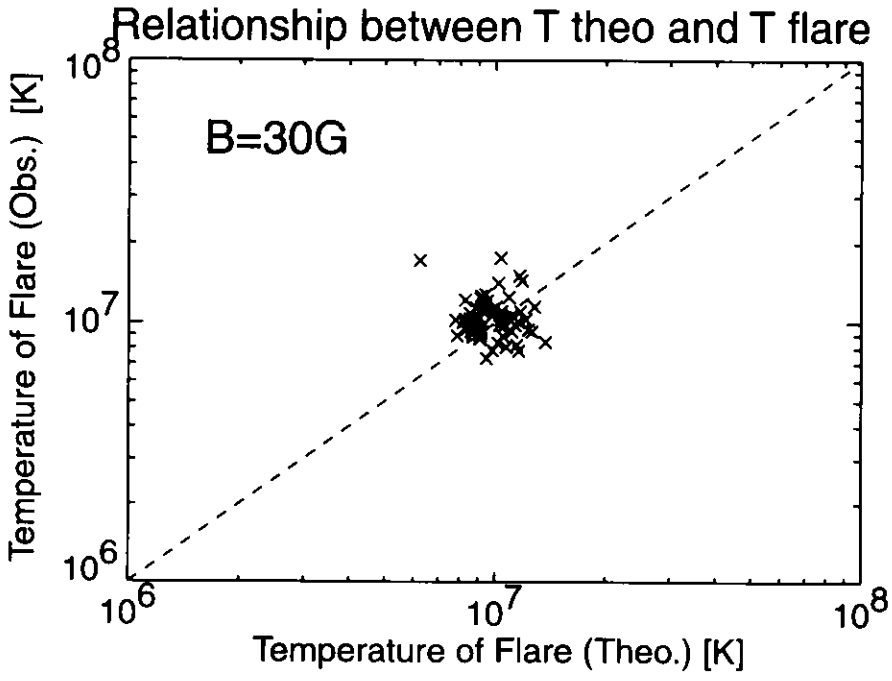

Figure 3.19: Relationship of temperature between quantities obtained from Eq. 3.1 and observation. Dashed line (B = 30 G) shows the best correlation.

proton mass, n_0 is the preflare proton number density (= electron density), and L is the characteristic length of the (reconnected) magnetic loop. This law was red using by the theory which is based on a magnetic reconnection model with heat conduction and chromospheric evaporation, assuming that the gas pressure of a flare loop is comparable to magnetic pressure. According to this scaling law, the maximum temperature of flare loop is proportional to the characteristic length of the loop, if both the magnetic field strength and the electron density are independent from the loop length.

Fig. 3.19 shows the relationship of observed temperatures and theoretical temperatures estimated with *Yokoyama-Shibata* scaling law, assuming $B = 30$ G. We see from this figure that when the coronal magnetic field is about 30 G, the theory is consistent to the observation, though the dispersion of the correlation is large, implying the importance of precise coronal magnetic field measurement.

Fig. 3.20, quoted from Shibata & Yokoyama (1999), is the relationship between temperature and emission measure of solar and stellar flares. This figure indicates that for a fixed magnetic field strength, the flare temperature increases as the flare loop length increases. Similarly the relationship between temperatures and emission measures from our observation are plotted in Fig. 3.21. In the top panel of Fig.3.21, squares (□),

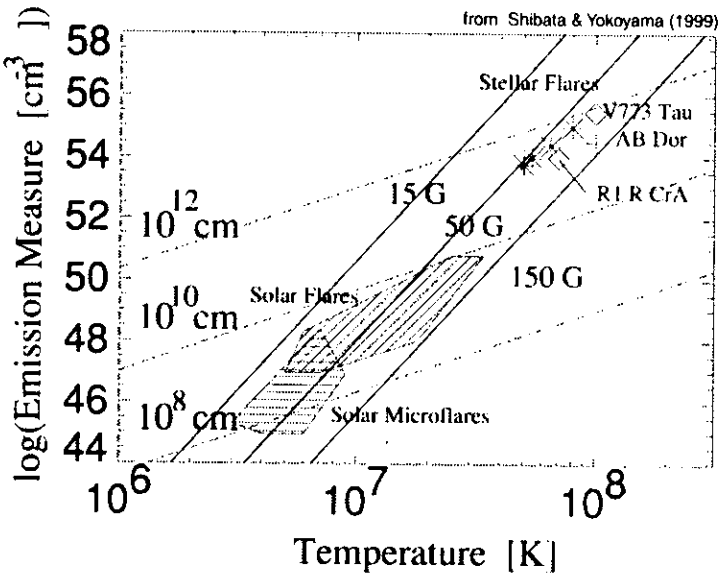

Figure 3.20: Relationship between temperature and emission measure of solar flares and stellar flares (from Shibata & Yokoyama 1999).

diamonds ($\diamond$), and crosses ($\times$) stand for the loop length of 2×10^9 cm, 10^9 cm, and 10^8 cm, respectively. Though longer loops seem to correspond to bigger VEMs, this relation is not clear. We plot the quantities of the flare and the high-temperature region in the lower graph. Asterisks ($*$) and diamonds ($\diamond$) represent the high-temperature regions and the flare loops, respectively. This figure shows that the points of the high-temperature regions extend to the lower right, not consistent with the theory.

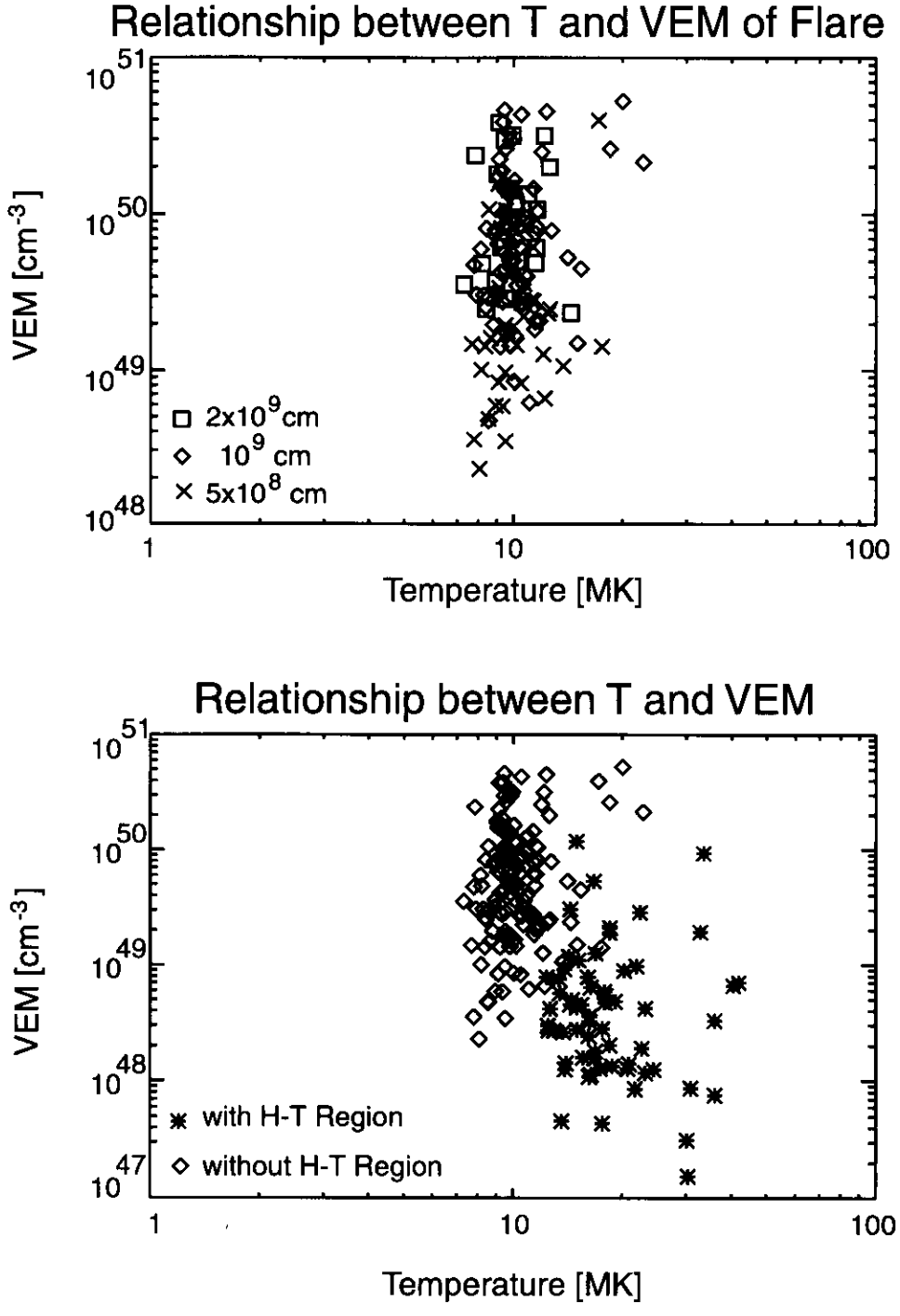

Figure 3.21: (Upper) Relationship between temperatures and emission measures of flare loops: Squares (□), diamonds (◇), and crosses (×) are the loop length of 2×10^9 cm, 10^9 cm, and 10^8 cm, respectively. (Lower) Relationship between temperature and emission measure of flare loops and high-temperature regions. Asterisks (*) and diamonds (◇) stand for high-temperature regions and flare loops, respectively.

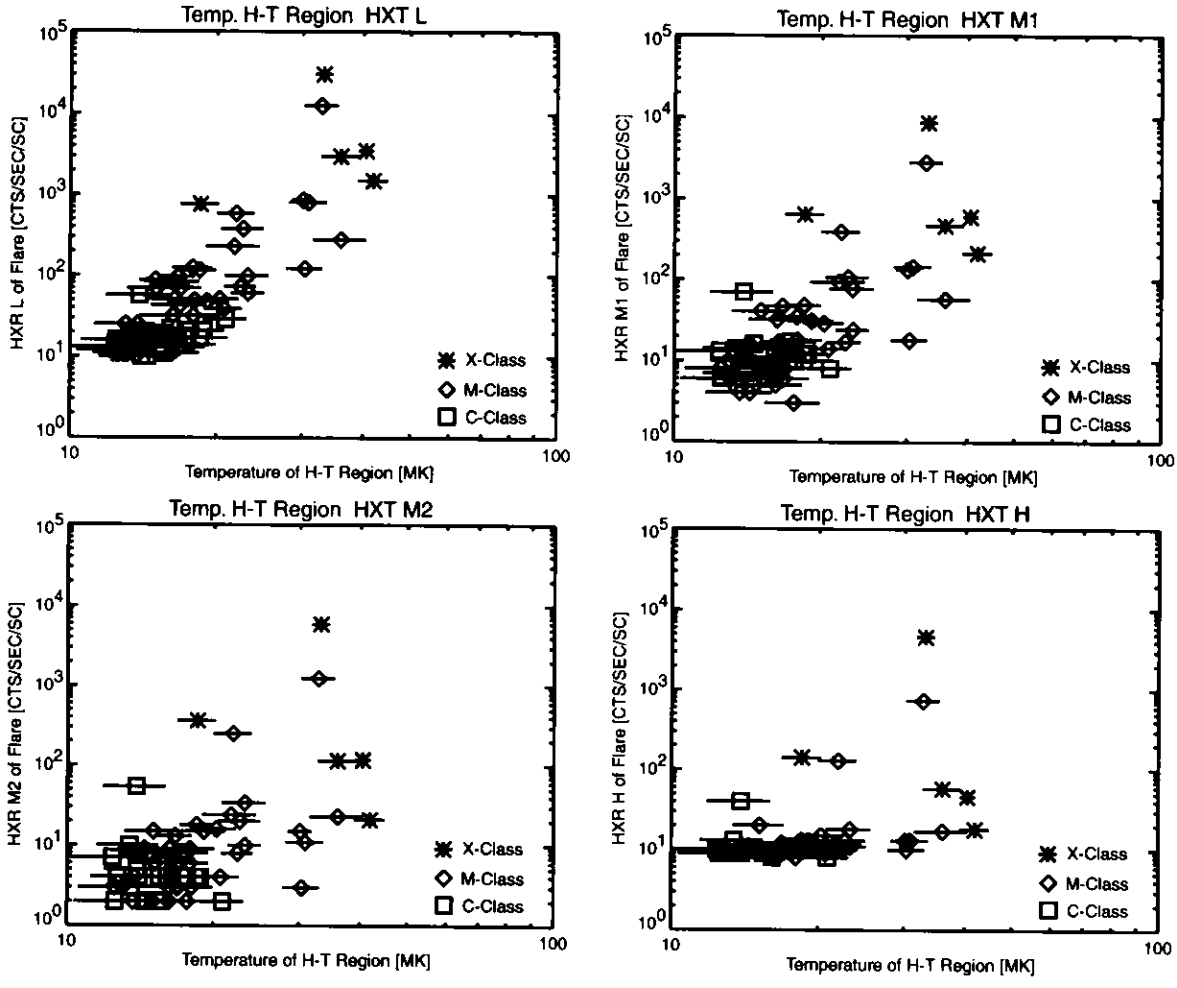

Figure 3.22: Relation between temperatures and hard X-ray peak counts observed in HXT L-, M1-, M2-, H-bands. Squares (□), diamonds (◇), and pluses (+) stand for C-class, M-class, and X-class flares, respectively.

3.4.5 Electrons of High-Temperature Regions

Fig. 3.22 shows the relationship between temperature of the high-temperature region and hard X-ray peak intensity observed in the HXT L-, M1-, M2, H-bands. The flare X-ray fluxes obtained from GOES satellite distinguish symbols; squares (□), diamonds (◇), and plus (+) stand for C-class, M-class, and X-class flares, respectively. We see in Fig. 3.22 that stronger flares have stronger intensities for both hard and soft X-rays. Important to note is that the temperatures of the high-temperature region shows a clear correlation with the low-energy hard X-rays, suggesting that both thermal and non-thermal sources contribute to the HXT L-band, adding credence to the high-temperature estimates.

3.5 Summary

This investigation reveals the following conclusions:

1. We have found 64 flares associated with high-temperature regions out of 141 flares.
2. The average temperature, volume emission measure, and area of the high-temperature regions are 19 MK, $10^{48.6}$ cm^{-3}, and 1.5×10^9 km^2, respectively. Similarly, the same quantities of the flare loops are 11 MK, $10^{49.9}$ cm^{-3}, and 2.0×10^9 km^2, respectively.
3. The temperature of the high-temperature region is proportional to that of the flare loop.
4. The area of the high-temperature region is proportional to that of the flare loop.
5. High-temperature regions begin to appear during the hard X-ray impulsive phases and reach maximum temperature before the peak of the soft X-ray intensity. They continue to be observed for about 10 minutes during soft X-ray decay phases.
6. The rise velocity of the high-temperature region is $2 \sim 3$ times as fast as that of flare loop.
7. Flares associated with high-temperature regions have stronger X-ray flux, longer lifetimes, and bigger area than those without high-temperature regions.

References

Carmichael, H. 1964, in AAS-NASA Symposium on Solar Flares, ed. W. N. Hess (NASA SP-50), 451

Culhane, J. L., Hiei, E., Doschek, G. A., Cruise, A. M., Ogawara, Y., Uchida, Y., Bently, R., Brown, C. M., Lang, J., Watanabe, T., et al. 1991, Sol. Phys., 136, 89

Doschek, G. A. 1999, ApJ, 527, 426

Hirayama, T. 1974, Sol. Phys., 34, 323

Kopp, R. A., & Pneuman, G. W. 1976, Sol. Phys., 50, 85

Kosugi, T., Makishima, K., Murakami, T., Sakao, T., Dotani, T., Inda, M., Kai, K., Masuda, S., Nakajima, H., Ogawara, Y., Sawa, M. & Shibasaki, K. 1991, Sol. Phys., 136 17

Masuda, S., Kosugi, T., Hara, H., Tsuneta, S., & Ogawara, Y. 1994, Nature, 371, 495

Ogawara, Y., Takano, T., Kosugi, T., Tsuneta, S., Watanabe, T., Kondo, I. & Uchida, Y. 1991, Sol. Phys., 136, 1.

Petschek, H. E. 1964, in AAS-NASA Symposium on Solar Flares, ed. W. N. Hess (NASA SP-50), 425

Priest, E. R. 1981, in *Solar Flare Magnetohydrodynamics*, ed. E. R. Priest (New York: Gordon & Breach), 1

Sakao, T., Kosugi, T., & Masuda, S. 1998, in *Observational Plasma Astrophysics: Five Years of Yohkoh and Beyond*, eds. T. Watanabe, T. Kosugi, & A. C. Sterling, p 273

Sato, J., Sawa, M., Masuda, S., Sakao, T., Kosugi, T., & Sekiguchi, H. 1998, THE YOHKOH HXT IMAGE CATALOGUE

Shibata, K., & Yokoyama, T., 1999, ApJ, 526, L49

Sturrock, P. A. 1966, Nature, 211, 695

Tsuneta, S., Acton, L., Bruner, M., Lemen, J., Brown, W., Caravalho, R., Catura, R., Freeland, S., Jurcevich, B., Morrison, M., Ogawara, Y., Hirayama, T., & Owens, J., 1991, Sol. Phys., 136, 37.

Tsuneta, S., Masuda. S., Kosug, T., & Sato. J. 1997, ApJ, 478, 787

Yokoyama, T., & Shibata, K., 1998, ApJ, 494, L113

Warren, H. P., Bookbinder, J. A., Forbes, T. G., Golub, L., Hudson, H. S., Reeves, K., & Warshall, A. 1999, ApJ, 527, L121

Chapter 4

Relation between High-Temperature Regions and Other Phenomena

Abstract

From the list of flares in "THE YOHKOH HXT IMAGE CATALOGUE" by Sato et al (1998), we have selected events, which have hard X-ray double footpoint sources in one of the images of HXT L-, M1-, M2-, and H-bands, and investigated the relationship between the location of the high-temperature region above the loop top and the intensities of hard X-ray footpoint source. We find that the high-temperature region is located closer to the brighter hard X-ray footpoint source. Using the list of high-temperature regions by Akiyama (2001), we have selected the events which are associated with soft X-ray plasma ejecta, and compared the location of the high-temperature region and the trajectory of ejecta. We found no clear geometrical relationship between them.

4.1 Introduction

The soft X-ray telescope (SXT) (Tsuneta et al., 1991) and the hard X-ray telescope (HXT) (Kosugi et al., 1991) aboard *Yohkoh* (Ogawara et al., 1991) have better temporal coverages and resolutions than those of previous solar X-ray telescopes, and have revealed many previously unknown coronal structures. Among these newly discovered phenomena, the hard X-ray source above the flare loop top is one of the most interesting findings (Masuda et al., 1994). The discovery of this hard X-ray source in impulsive flares has contributed to the idea that solar flares release energy by magnetic reconnection at a site above the soft X-ray loop tops, and that the flare model for traditional two-ribbon type (or LDE) flares may be also applicable to impulsive flares. According to Masuda et al. (1994), the loop-top hard X-ray source has an effective temperature of 100–150 MK and a total

emission measure (EM) of 10^{44} cm^{-3}, if the hard X-ray source is thermal origin (superhot source). Moreover, the area above the flare loop shows higher temperatures than those of other regions in soft X-ray as well as hard X-ray images. According to the statistical study of 64 flares having the high-temperature regions obtained from soft X-ray images by Akiyama (2001), in Chapter 3 of this thesis, these high-temperature regions were observed about half of the flares and had the following observed characteristics: (1) The average temperature is 19 MK, and is about 1.5 times as high as that of the flare loops. (2) The average of volume emission measures (VEMs) is $10^{48.6}$ cm^{-3}, and is one order larger than that of flare loops. (3) The average size is 1.5×10^8 km^2. (4) In temperature and in size, the high-temperature regions have obvious correlations with the flare loops. (4) The temperatures of the high-temperature regions have clear correlation with soft X-ray flare fluxes. (5) Flares with the high-temperature regions are generally long duration events and have large structures. (6) The high-temperature regions appear during the hard X-ray impulsive phase and reach the maximum temperature before the peak of soft X-ray intensity. (7) The rising speed of the high-temperature regions is, as an average, about twice as fast as that of the flare loops.

Besides these characteristics of the high temperature region, we examine the positions of these regions in connection to the flare loops, and hard X-ray loop-top and double foot point sources. Shibata et al. (1995) and Ohyama & Shibata (1998) pointed out that some X-ray ejecta observed in impulsive flares suggested energy release mechanism by magnetic reconnection. Therefore Shibata et al. (1995) proposed that magnetic reconnection took place in all flare-like phenomena, and the differences between impulsive and LDE flares were only in size and life time, which modified the apparent characteristics of the flares. According to his unified model, plasma ejection in flares is a key process to trigger fast magnetic reconnection by this rising motion of plasmas. Since the hard X-ray loop top source is regarded as an interaction region of reconnection outflows and thermal flare loops, the reconnection point is considered to be located between the hard X-ray loop top source and the plasma ejecta.

If the magnetic reconnection is taken as an energy source for solar flares, understanding the global coronal magnetic structures is essential for flare physics. Therefore, the purpose of this chapter is to investigate the morphological characteristics of the high-temperature region, and especially, to compare the position of the high-temperature region in connection to X-ray plasma ejecta, which provides some hint about the magnetic structure above the flare loops.

4.2 Relation to Hard X-ray Foot-Points Sources

4.2.1 Data & Data Selections

The temperature maps obtained from soft X-ray images used for identifying the position of high-temperature region were derived from the soft X-ray telescope (SXT) (Tsuneta et al., 1991) aboard *Yohkoh* (Ogawara et al., 1991). We use only partial-frame image (PFI) data taken in the flare mode, which has high temporal (about 2 s) and spatial (2.5 arcsec) resolutions. The way the temperature maps are made and the high-temperature regions are defined is as in Akiyama (2001).

The hard X-ray images were taken by the hard X-ray telescope (HXT) (Kosugi et al., 1991) aboard *Yohkoh*. It is a hard X-ray imager of Fourier-synthesis type, consisting of 64 modulation subcollimators. HXT is capable of taking simultaneous imaging in four energy bands, namely, the L-band (13.9 – 22.7 keV), M1-band (22.7 - 32.7 keV), M2-band (32 – 52.7 keV), and H-band (52.7 - 92.8 keV). Basic temporal and angular resolutions are 0.5 s and 5 arcsec, respectively.

Events which satisfy the following conditions are selected:

- Events are observed by both of the Al 11.6 and Be 119 filters; the combination of these two filters is most sensitive for temperature diagnostics of flaring plasma.
- The total number of images in each event is more than 30, consisting of full-resolution PFIs; this enables to examine the time profile of the high-temperature region.
- Events are listed in "THE YOHKOH HXT IMAGE CATALOGUE" edited by Sato et al (1998), and have peak count rates greater than 10 cts/s/subcollimator (SC) for the L-, M1-, and M2-bands, and 20 cts/s/SC in the H-band; the H-band has a larger background count rate than the other bands.
- Events have the high-temperature regions defined by the same Akiyama (2001) criteria.
- Events which have double footpoint hard X-ray sources observed in more than one of the HXT bands, namely in the L-, M1-, M2-, or H-band images in order to survey the relative location of the high-temperature region to the hard X-ray footpoint sources.
- Events which have both footpoints inside the solar limb.

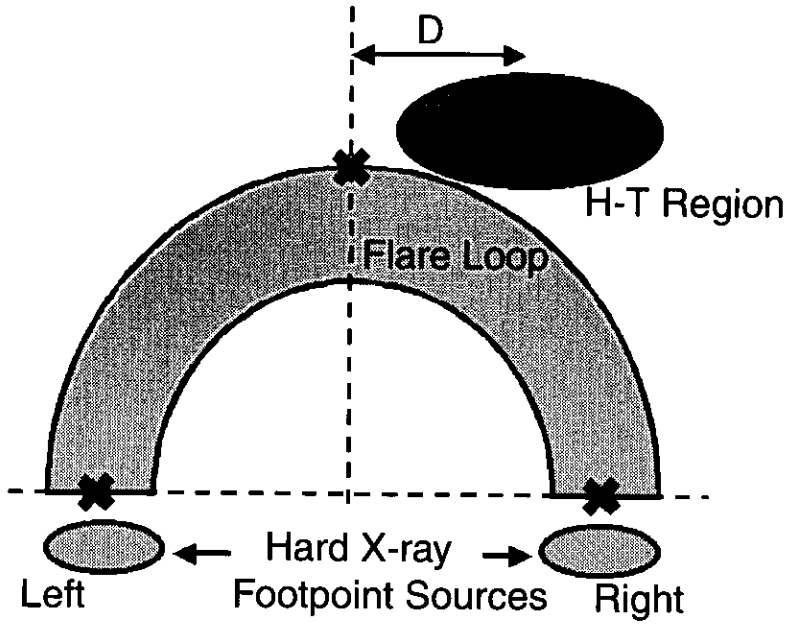

Figure 4.1: Schematic flare-loop configuration; double footpoint sources and high-temperature region. "D" is the distance of high-temperature region from the bisector, and is positive, when it is located on the "right"-side of the flare loop put concave down in the X-ray image.

We found 19 flares applying the above criteria for the events from 1 October 1991 to 31 August 1998. We select the flares which have hard X-ray double footpoint sources: Fig. 4.1 schematically shows how to measure "D," the distance to the center-of-gravity of the high-temperature region from the perpendicular bisector of the double footpoint sources. For convenience, we also define the "right" footpoint source in hard X-rays as one located on the right-side, when the soft X-ray flare loop is placed concave down (inverse U shape) in the SXT image. The distance D has a positive sign, when the high-temperature region is found on the "right"-side. The hard X-ray intensities of each footpoint source are listed in Table 4.1.

4.2.2 Results

Fig. 4.2 shows the location of high-temperature regions relative to hard X-ray double footpoint sources. The abscissa is the ratio of the hard X-ray intensity of the right footpoint to the left footpoint. The ordinate is the distance of the high-temperature region (D). We see from Fig. 4.2 that the majority of points scatter in the first and fourth quadrants, which means that the high-temperature region tends to be on the side of the stronger hard X-ray footpoint source.

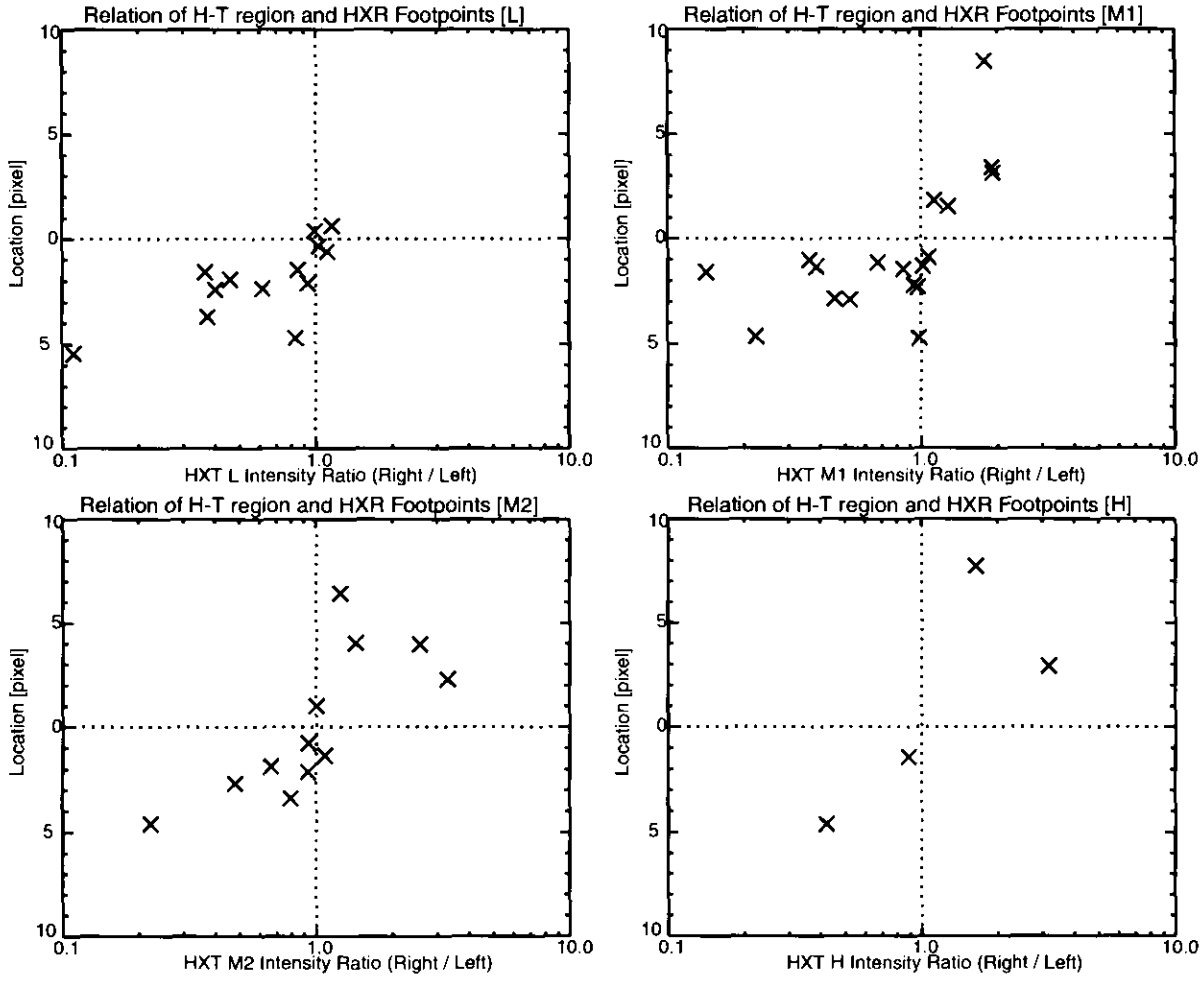

Figure 4.2: Relative location of the high-temperature region and hard X-ray double footpoint sources observed in HXT L-, M1-, M2-, and H-bands: Distance of high-temperature region from the footpoint bisector is plotted against the footpoint hard X-ray intensity ratio, right/left.

Table 4.1: List of Flares and Hard X-ray Footpoint Sources

	General Infomation			HXT Footpoint Source								Distance			
event[1]	DAY	Time	Location	Lo		M1		M2		H		L	M1	M2	H
no.	YYMMDD	HHMMSS		R	L	R	L	R	L	R	L				
00980	911119	0928	S14W66	3100	3707	2209	2249	–	–	–	–	-4.70	-4.70	–	–
01110	911204	1743	N18E58	3656	5924	2732	3220	2723	4099	2569	2886	-2.35	-1.43	-1.86	-1.41
01640	911215	1421	N06W41	3256	2803	2063	1614	2030	616	–	–	0.63	1.55	2.280	–
01690	911216	0359	S12E70	–	–	600	1551	–	–	–	–	-1.34	–	–	–
01860	911224	0406	S16E58	523	1429	117	824	–	–	–	–	-1.57	-1.58	–	–
02880	920207	1127	S18W52	–	–	2805	1481	2731	1068	2890	910	–	3.40	3.97	2.93
04590	920714	1744	S12W32	3628	3518	1880	2801	–	–	–	–	-0.35	-1.13	–	–
04810	920811	1329	S12W44	2995	3524	2521	2482	2329	2153	–	–	-1.47	-1.30	-1.34	–
05010	920822	0823	N16W62	2193	4773	1422	3921	–	–	–	–	-1.92	-1.02	–	–
05180	920906	0502	S08W38	–	–	3967	2076	3245	2271	–	–	–	3.14	4.03	–
05490	920912	1521	N18E20	1859	4952	1873	3574	–	–	–	–	-3.70	-2.88	–	–
05690	921011	0203	S12W60	2927	2635	1901	1782	2074	2226	–	–	-0.62	-0.89	-0.78	–
05820	921027	2217	S26W20	–	–	3564	3813	2145	2694	–	–	-2.18	-3.39	–	–
07210	930218	1013	S21E21	3747	4023	3354	3453	3103	3333	–	–	-2.10	-2.28	-2.12	–
07850	930422	1359	N12E04	2091	5198	1627	3555	1541	3209	1176	2791	-2.40	-2.85	-2.68	-4.62
08660	931003	0902	N08N02	7551	7591	6730	5962	7505	7449	–	–	0.38	1.83	1.01	–
09390	940116	2309	N08E74	–	–	3920	2208	4186	3354	3499	2141	8.49	6.43	7.75	–
09790	940630	2038	S12E30	840	7588	668	2992	57072571	–	–	-5.46	-4.64	-4.61	–	

Table 4.2: List of X-ray Ejecta and High-Temperature Region

	Flare			Ejecta		H-T Region
event[2] no.	DAY YYMMDD	Time HHMMSS	GOES	Shape	Motion	Position
01060	911202	044857	M3.6	Blob/Loop	top	right
02260	920113	172435	M2.0	Loop	top	top
02820	920206	031203	M7.6	Loop	right	left
07190	930217	103336	M5.8	Loop	top	top
07220	930221	003049	M1.4	Loop	top	top
08240	930625	031133	M5.1	Loop	right	top
08530	930927	120709	M1.8	Loop	left	top
09390	940116	230821	M6.1	Loop	right	right
10980	971106	115112	X9.4	Loop	right	top
11510	980323	024343	M2.3	Loop	top	top
11650	980423	052918	X1.2	Loop	top	top
11660	980424	084520	C8.9	Loop	top	left
11950	980509	031733	M7.7	Loop	right	right
12460	980818	081713	X2.8	Loop	right*	left
12470	980818	221301	X4.9	Loop	right*	left

*) Loop-like plasma ejecta sit on the left side of the flare loop, while the ejected loop was expelled from the right footpoint.

4.3 Relation with Soft X-ray Plasma Ejections

4.3.1 Data & Data Selections

The temperature maps of the high-temperature region were constructed from the images of the soft X-ray telescope (SXT) (Tsuneta et al., 1991) aboard *Yohkoh* (Ogawara et al., 1991). We use only partial-frame (PFI) images taken in the Flare mode, which has high temporal (about 2 s) and spatial (2.5 arcsec) resolutions. From the list of the high-temperature regions (Akiyama, 2001), 64 flares are selected from "THE YOHKOH HXT IMAGE CATALOGUE" edited by Sato et al (1998).

As for the soft X-ray plasma ejecta, we use only PFI data taken in the Quiet mode, which have three spatial resolutions: "full-resolution" of 2.5 arcsec/pixel, "half-resolution" with 5 arcsec pixel-size, and "quarter-resolution" with 10 arcsec summation. The time resolution of the Quiet mode ranges from several sec to a few minutes. The images that we use to investigate the X-ray plasma ejecta in this paper were obtained with either the Al.1 filter or the Al/Mn/Mg filter. Both filters are sensitive to soft X-rays between 3 and 40 Å and enable observations of plasma with temperatures from 1.5×10^6 K to a few $\times$ 10^7 K (Tsuneta et al., 1991).

Sixteen events associated with soft X-ray plasma ejecta are found in the list of flares the high-temperature regions, Table 4.2, by visual inspection of the data.

Table 4.3: Relationship between the Ejecta and the High-Temperature Region

	Number	%	% of "Top" Type of Ejecta
Same Direction	7	44 %	31 %
Differet Direction	9	56 %	13 %

4.3.2 Results

Comparing the moving direction of ejecta and the location of the high-temperature region around the flare loop, we choose first the events with the X-ray plasma ejecta in the list of flares having the high-temperature regions. Fig. 4.3 shows the example of the images of 2 December 1991 flare. The first and third row panels show the temperature maps and the soft X-ray images obtained from the Al12 filter, respectively. Times of observations are also shown. The second row is the difference image, the image obtained during the top time span subtracted by the image during the bottom time span. The loop-like plasma ejection is indicated by arrows in the third row panels. As for the X-ray ejecta observed in either half or quarter-resolution images, we superpose the temperature maps of reduced resolution to match the resolution of those images. Second, we classify the moving direction of ejecta into three patterns ("right side", "top", "left side") in connection to the flare loop. The same definition of the direction used for the high-temperature region is applied to the ejection direction. For the Fig. 4.3 event, the X-ray ejecta moved upward from (to the "top" of) the flare loop and the high-temperature region was located on the right side of the flare loop. The results are summarized in Table 4.2. The table contains the shape of ejected plasma, the moving direction of ejected plasma, and the location of the high-temperature regions.

The statistics are shown in Table 4.3. Since it is difficult to determine the plasma ejection direction precisely, the direction need only to be close to vertical to (to the "top" of) the flare loop to be so classified. The percentage of this "top" direction of ejected plasma is shown in Table 4.3. No definite correlation was found in Table 4.3 for the moving direction of the ejected plasma and the location of the high-temperature region

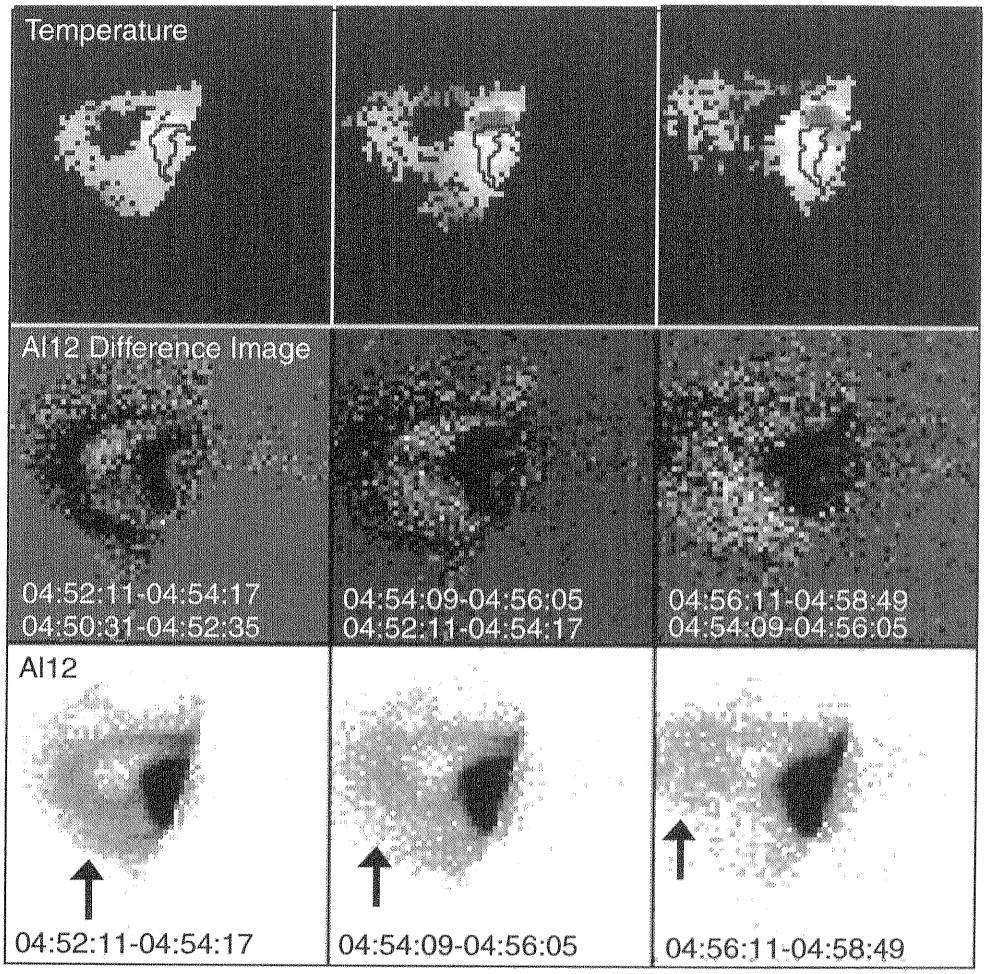

Figure 4.3: High-temperature region and X-ray plasma ejecta of the 2-Dec-1991 flare. The first and the third row panels are temperature maps and soft X-ray intensity images, respectively. The second row panels show the difference images of soft X-ray intensity (image during the top time span subtracted by image during bottom time span). Ejected plasmas are indicated by arrows.

4.4 Summary and Discussion

4.4.1 Location of High-Temperature Regions

In Fig. 4.2 high-temperature regions are found to be preferentially situated toward the stronger sides of the double footpoint sources seen in hard X-rays. Sakao et al (1992) and Canfield et al. (1992) reported the asymmetry of hard X-ray brightness of the double footpoint sources in the impulsive phase: The footpoint with the stronger magnetic field has the stronger magnetic field convergence, and hence, has less electron precipitation than the footpoint with the weaker field due to magnetic-mirror effect. Interactions with particles penetrating to the footpoints of coronal magnetic fields tend to be enhanced in the footpoint of the weaker magnetic field, if particles are equally accelerated and penetrating to the both footpoints. This situation explains the fact that almost all of the high-temperature regions are located in the brighter side of the hard X-ray footpoints. Based on these results, we can conclude that the high-temperature region tends to be located on the weaker side of the coronal magnetic fields.

It is noted that these observations and interpretations are based on the two-dimensional data of SXT, and therefore, might include some ambiguity in deriving the location of high-temperature regions. More concrete information about the 3-D structures of flaring regions are required in future researches. With such information, a more definite relationship might be revealed between the intensity of hard X-ray sources and the location of the high-temperature region above the loop top.

4.4.2 Global Magnetic field

We see from table 4.3 that there is no clear relationship between the moving direction of ejected plasma and the location of high-temperature regions. This might partly come from technical difficulty in determining the 3-D trajectory of plasma ejecta in the 2-D SXT images; no definite reference point for the ejecta can be determined, since the shapes are mostly loop-like. However, it should be also considered that the moving direction of X-ray ejects is influenced by the structure of magnetic field above the flare loop. It has been suggested for a long time that some instability of large-scale magnetic fields may trigger these plasma ejections and associating flare activity of the entire regions. Despite these ambiguities, there are two definite events on 18 August 1998, in which the plasma ejections started at the opposite footpoints from the respective high-temperature regions.

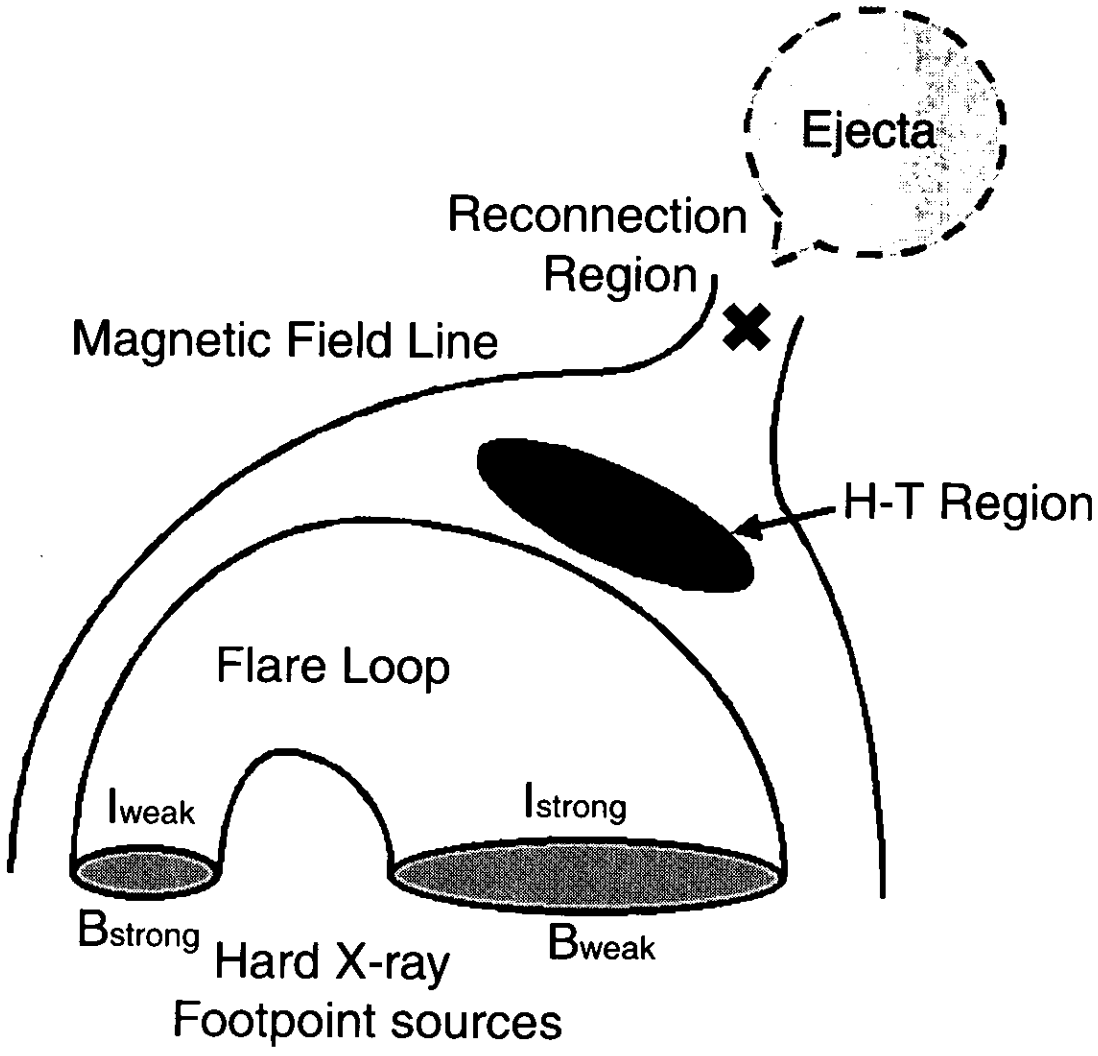

Figure 4.4: A schematic presentation of flare, which has asymmetry of magnetic fields.

4.4.3 Flare Model

A schematic picture of flare is shown, which explicitly shows an asymmetry of the magnetic fields in the photosphere (Fig. 4.4). This picture is similar to the stardard model of two-ribbon flares and the anti-cornucopia model for impulsive flares (Sakao, 1998). Therefore, this picture fits the concept of the unified flare model (Shibata et al., 1995) and the location of the high-temperature region is consistent with this model. However, a more quantitative comparison of observations and simulations is definitely required to prove Tsuneta et al. (1997)'s scenario that the high-temperature region is heated by slow shocks originating from the reconnection outflow.

References

Akiyama, S. 2001, PhD Thesis., The Graduate University for Advanced Studies

Canfield, R. C., Hudson, H. S., Leak, K. D., Mickey, D. L., Metcalf, T. R., Wuelser, J.-P., Acton, L. W., Strong, K. T., Kosugi, T., Sakao, T., Tsuneta, S., Culhane, J. L., Phillips, A., and Fludra, A. 1992, PASJ, 44, L111

Kosugi, T., Makishima, K., Murakami, T., Sakao, T., Dotani, T., Inda, M., Kai, K., Masuda, S., Nakajima, H., Ogawara, Y., Sawa, M. & Shibasaki, K. 1991, Sol. Phys., 136 17

Masuda, S., Kosugi, T., Hara, H., Tsuneta, S., & Ogawara, Y. 1994, Nature, 371, 495

Ohyama, M., & Shibata, K. 1998 ApJ, 499, 934

Ogawara, Y., Takano, T., Kosugi, T., Tsuneta, S., Watanabe, T., Kondo, I. & Uchida, Y. 1991, Sol. Phys., 136, 1.

Sakao, T., Kosugi, T., Masuda, S., Inda, M., Makishima, K., Canfield, R. C., Hudson, H. S., Metcalf, T. R., Wuelser, J.-P., Acton, L. W.,and Ogawara, Y. 1992, PASJ, 44, L83

Sakao, T., Kosugi, T., & Masuda, S. 1998, in *Observational Plasma Astrophysics: Five Years of Yohkoh and Beyond*, eds. T. Watanabe, T. Kosugi, & A. C. Sterling, p273

Sato, J., Sawa, M., Masuda, S., Sakao, T., Kosugi, T., & Sekiguchi, H. 1998, THE YOHKOH HXT IMAGE CATALOGUE

Shibata, K., Masuda, S., Shimojo, M., Hara, H., Yokoyama, T., Tsuneta, S., Kosugi, T., & Ogawara, Y. 1995, ApJ, 451, L83

Tsuneta, S., Acton, L., Bruner, M., Lemen, J., Brown, W., Caravalho, R., Catura, R., Freeland, S., Jurcevich, B., Morrison, M., Ogawara, Y., Hirayama, T., & Owens, J., 1991, Sol. Phys., 136, 37.

Tsuneta, S., Masuda. S., Kosug, T., & Sato. J. 1997, ApJ, 478, 787

Chapter 5

Summary and discussion

So far we have discussed the properties of the high-temperature regions and their relationships to other phenomena based on our reliable temperature maps obtained from SXT images. In this section, we summarize the results of our studies and comment on the future directions of the research.

5.1 Summary

The hard X-ray loop top sources were discovered by the hard X-ray telescope (HXT) aboard *Yohkoh* (Masuda et al., 1994). At the same time the high-temperature regions were observed with the soft X-ray telescope (SXT) aboard *Yohkoh* (Masuda et al., 1994; Nitta & Yaji, 1997; Tsuneta et al., 1997; Doschek, 1999). We have investigated these phenomena observed with SXT using the data obtained from both SXT and HXT. We summarize our studies here, following the conclusions in each chapter of the thesis:

5.1.1 Chapter2 : Evaluation of Temperature Map Observed with the YOHKOH SXT

We have assessed the errors in temperature map obtained from SXT to increase the reliability of temperatures in the high-temperature regions. We estimated the PSF of the Be119 and the Al12 filters using the SXT_PSF procedure and evaluated the temperature map derived from the deconvolved images. Errors considered were

- Error of jittering motions of the spacecraft during the observation was about 0.1 pixel. The Maximum of the error corresponded to about 4 MK.
- Error of integrated moving phenomena taken about 2 minutes apart was about 1 pixel. Therefore, errors introduced by intrinsic plasma motions are negligible.

- Effects of scattered lights to the high-temperature regions came from the brightest flare core regions. We made temperature map using the core part of PSF obtained from the SXT_PSF procedure and evaluated temperature maps in the corrected images. Consequently, more accurate temperatures were successfully derived from the deconvolved data, while shape of faint structures could also be extracted from the original data.

5.1.2 Chapter3 : Characteristics of High-Temperature Region above the Loop Top

We detected 64 high-temperature regions above flare loops during October 1991 and August 1998 using the Partial frame images of SXT/*Yohkoh* and found the following properties.

- We have found 64 flares associated with high-temperature regions out of 141 flares.
- The average temperature, volume emission measure, and size of the high-temperature regions are 19 MK, $10^{48.6}$ cm^{-3}, and 1.5×10^9 km^2, respectively. Similarly, the same quantities of the flare loops are 11 MK, $10^{49.9}$ cm^{-3}, and 2.0×10^9 km^2, respectively.
- Temperature of the high-temperature region is proportional to that of the flare loop.
- Size of the high-temperature region is proportional to that of the flare loop.
- High-temperature regions begin to appear during hard X-ray impulsive phases and reach the maximum temperature before the peak of soft X-ray intensity. They continue to be observed for about 10 minutes during soft X-ray decay phases.
- The rising speed of the high-temperature region is $2 \sim 3$ times as fast as that of flare loop.
- Flares associated with high-temperature regions have stronger X-ray flux, longer life time, and bigger size than those without high-temperature regions.

5.1.3 Chapter4 : Relation between High-Temperature Regions and Other Phenomena

From the list of flares in "THE YOHKOH HXT IMAGE CATALOGUE" by Sato et al (1998), we have selected events, which have hard X-ray double footpoint sources in one of the images of HXT L-, M1-, M2-, and H-bands, and investigated the relationship between

the location of the high-temperature region above the loop top and the intensities of hard X-ray footpoint source. We found that the high-temperature region is located closer to the brighter hard X-ray footpoint source. Using the list of high-temperature regions by Akiyama (2001) in chap. 3, we have selected the events which are associated with soft X-ray plasma ejecta, and compared the location of the high-temperature region and the trajectory of ejecta. We found no clear geometrical relationship between them.

5.2 Future Direction

In order to understand the formation mechanisms of the high-temperature regions above flare loops, we studied the high-temperature regions observed in SXT. Though we found that the high-temperature region could be directly related to magnetic reconnection, we could not close in upon its detailed mechanism. Tsuneta et al. (1997) proposed that the high-temperature regions observed with SXT were heated by slow shock produced by magnetic reconnection. To confirms whether this story is correct. we think it necessary and indispensable to observe slow shock as directly as to see density and velocity jumps at the shock fronts. We expect to do this by *Solar-B* satellite.

Moreover, since we have not paid attention to the following interesting topics, we will take in the future direction of this study the following approaches.

Comparison between Hard X-Ray Loop Sources and High-Temperature Regions

In this thesis we did not investigated comparison the high-temperature region obtained from SXT with hard X-ray loop sources, because there were a few flares associated with hard X-ray sources. Tsuneta et al. (1997) and Nitta & Yaji (1997) compared relative locations of the two phenomena. The former authors proposed that the high-temperature regions represent the super-hot ($\geq$ 30 MK) plasma, while, the latter authors denied. We seem to agree Our study in this thesis might agree to the conclusions of the former authors, as the temperature of the high-temperature regions obviously were higher than that of the flare loop in our definition.

Comparison between CSHKP Flare Model and Emerging Flux Model

Since the origin of Hard X-ray loop top sources could be suggested from the CSHKP flare model, the formation of the high-temperature region could also be implemented in the the current scheme of the CSHKP model. On the other hand, the other type of flare

model was proposed, in which magnetic reconnection takes place by emerging flux from the photosphere (Heyvaerts, 1977; Nishio et al., 1997). We would like to pay attention to the latter type of flares, and to investigate whether the high-temperature regions with the same characteristics might also prevail in these events.

References

Akiyama, S. 2000, PhD Thesis., The Graduate University for Advanced Studies

Doschek, G. A. 1999, ApJ, 527, 426

Heyvaerts, J., Priest, E. R., & Rust, D. M. 1997, ApJ, 216, 123

Masuda, S., Kosugi, T., Hara, H., Tsuneta, S., & Ogawara, Y. 1994, Nature, 371, 495

Nishio, M., Yaji, K., Kosugi, T., Nakajima, H., & Sakurai, T. 1997 ApJ, 489, 976

Nitta, N., & Yaji, K. 1997, ApJ, 484, 927

Nitta, N., Sato, J., & Hudson, H. 2001, ApJ, in press

Tsuneta, S., Masuda, S., Kosugi, T., & Sato, J. 1997, ApJ, 478, 787

model was proposed, in which magnetic reconnection takes place by emerging flux from the photosphere (Heyvaerts, 1977; Nishio et al., 1997). We would like to pay attention to the latter type of flares, and to investigate whether the high-temperature regions with the same characteristics might also prevail in these events.

References

Akiyama, S. 2000, PhD Thesis., The Graduate University for Advanced Studies

Doschek, G. A. 1999, ApJ, 527, 426

Heyvaerts, J., Priest, E. R., & Rust, D. M. 1997, ApJ, 216, 123

Masuda, S., Kosugi, T., Hara, H., Tsuneta, S., & Ogawara, Y. 1994, Nature, 371, 495

Nishio, M., Yaji, K., Kosugi, T., Nakajima, H., & Sakurai, T. 1997 ApJ, 489, 976

Nitta, N., & Yaji, K. 1997, ApJ, 484, 927

Nitta, N., Sato, J., & Hudson, H. 2001, ApJ, in press

Tsuneta, S., Masuda, S., Kosugi, T., & Sato, J. 1997, ApJ, 478, 787